AIR-SIDE CONDENSATE MANAGEMENT: DRAINAGE CHANNELS IN HEAT EXCHANGERS

BY

DEEP GUPTA

THESIS

Submitted in partial fulfillment of the requirements
for the degree of Master of Science in Mechanical Engineering
in the Graduate College of the
University of Illinois at Urbana-Champaign, 2010

Urbana, Illinois

Adviser:

Professor Anthony M. Jacobi

Abstract

Condensate on the air-side surface of flat-tube air-cooling heat exchangers can result in several adverse effects on the overall thermal-hydraulic performance. In order to improve the performance of compact heat exchangers under wet-surface conditions, promoting the drainage of condensed water is critical. Drainage channels on tube walls might provide a robust solution to promote condensate drainage from compact heat exchangers. A quantitative and qualitative evaluation of the effectiveness of drainage channels on the condensate retention characteristics of compact flat-tube louver-fin heat exchangers is presented. Various geometries of drainage channels are engraved on surrogate tubes in contact with fin stock. Two fin designs are tested using a dynamic dip testing method, and four designs are tested in a small wind tunnel apparatus. Data from the quantitative results and the visualization tests show that the drainage channels reduce the condensate retention for all the fin designs tested, except one. Fin structure plays an important role in determining the condensate retention behavior and hence the effect of drainage channels. Other important parameters, such as fin gap and louver gap, which have an effect on the condensate retention behavior are identified. The results include a comparison of drainage channel geometry and dimensions, over a range of incoming air velocity and relative humidity, and at different sample inclinations. The maximum effect obtained is a 27% reduction in steady-state retention. A method to implement drainage channels in full-size heat exchangers is suggested and an analysis suggests heat transfer can be improved by 12% while pressure drop is reduced by 9%.

Acknowledgements

In a cooperative endeavor, there are some personalities who deserve special acknowledgement due to their very special contribution and enlightened suggestions during the course of this project. Without their cooperation and encouragement this project would not have been possible.

I would first like to thank my advisor Professor Anthony M. Jacobi for his support and guidance throughout this project. His willingness to help and hardworking nature will always be an inspiration in my life. I would also like to thank Dr. Young-Gil Park, who proposed the idea for this project. His help and valuable advice, especially in the design of experimental apparatus is deeply appreciated. I would extend my thanks to all the members of the research group for providing me a conducive research environment, and motivating me at many times.

Also, I would especially thank Keith Parrish, Machine shop coordinator at the Mechanical Science and Engineering Department, and also other staff of the shop, for providing support in building the experimental apparatus for this project. Their suggestions in designing and manufacturing are really valuable to this project. I am further thankful to the Air Conditioning and Refrigeration Center (ACRC) for sponsoring this project.

Finally, I would like to thank my parents Gyan Prakash Gupta and Mradula Gupta, and my sister, Shikha Gupta for always being a tremendous source of love and support.

Table of Contents

List of Figures vii
List of Tables x
Nomenclature xi

Chapter 1 - INTRODUCTION 1
1.1 Introduction 1
1.2 Literature Review 2
1.2.1 Condensate Retention Characteristics and Related Effects: Earlier Studies 2
1.2.2 Studies Related to Automotive Louver-fin Heat Exchangers 5
1.2.3 Improving the Thermal-Hydraulic Performance 13
1.3 Project Objectives 17

Chapter 2 - EXPERIMENTAL METHODS 20
2.1 Dynamic Drainage Tests 20
2.1.1 Heat Exchanger Sample 20
2.1.2 Drainage Channel Designs 21
2.1.3 Dynamic Dip Testing Apparatus 21
2.1.4 Conditions and Procedure 22
2.2 Contact Angle Measurements 23
2.3 Real Time Condensate Retention and Visualization Tests 24
2.3.1 Heat Exchanger Assembly 24
2.3.2 Drainage Channel Designs 24
2.3.3 Closed Peltier Chamber 25
2.3.4 Table-Top Wind Tunnel Apparatus 25
2.3.5 Operating Conditions and Procedure 27
2.4 Fin Stock Designs 28

Chapter 3 – EXPERIMENTAL RESULTS AND DISCUSSION 40
3.1 Dynamic Dip Testing Results 40
3.1.1 Fin Design Comparison 40
3.1.2 Effect of Drainage Channels 42
3.1.3 Reliability of Dynamic Dip Tests: Contact Angle Variation 45

3.2 Closed Visualization Chamber 46
3.3 Table-Top Wind Tunnel Results 47
3.3.1 Fin Design Comparison 48
3.3.2 Effect of Drainage Channels 51
3.3.3 Effect of Sample Inclination 57
3.3.4 Effect of Inlet Relative Humidity 58
3.3.5 Effect of Air Velocity 60
3.3.6 Effect of Fin Base Temperature 61
3.4 Visualization Results 62

Chapter 4- IMPLEMENTATION OF DRAINAGE CHANNELS IN FULL-SIZE HEAT EXCHANGERS 99
4.1 Implementing Drainage Channels: Sample Design 99
4.2 Heat Transfer and Pressure Drop Estimation 100
4.2.1 Calculation Methodology 101
4.2.2 Effect of Drainage Channels on Heat Transfer Performance 103
4.2.3 Effect of Drainage Channels on Pressure Drop 106

Chapter 5– CONCLUSIONS AND RECOMMENDATIONS 114
5.1 Dynamic Dip Testing 114
5.2 Real-Time Condensate Retention and Visualization Experiments 115
5.3 Heat Transfer and Pressure Drop Calculations 118
5.4 Recommendations for Future Studies 119

Bibliography 121

Appendix A- Calculation of Air Side Area 129

Appendix B – Uncertainty Analysis 132
B.1 Dynamic Dip Tests 132
B.2 Contact Angle Measurements 134
B.3 Small Wind Tunnel Tests 135

Appendix C- Heat Transfer Calculations and EES Code 145
C.1 Heat/Mass Transfer Analysis 145

C.1.1 Coolant Side Calculations 145
C.1.2 Conduction Resistance 146
C.1.3 Air Side Resistance 146
C.1.4. Overall Heat Transfer Coefficient 150
C.1.5 Heat/ Mass Transfer Equations 150
C.2 Pressure Drop Analysis 154
C.2.1 Estimation of f-factor 154
C.2.2 Pressure Drop from f-factor 155

List of Figures

Figure 1.1 Condensate accumulation in louver-fin heat exchangers [50] 19
Figure 1.2 Effect of surface coating on the exit of fin column [34] 19

Figure 2.1 Heat exchanger sample used in dip tests [34] 29
Figure 2.2 Clamp and screw assembly (used in dynamic dip tests) 29
Figure 2.3 Clamp and screw assembly (holes and countersinks) 29
Figure 2.4 Channel dimensions & geometry (for dip tests): (a) rectangular channel at the center with w×d as width and depth, (b) positioning of two channels, (c) triangular channel with included angle, (d) trapezoidal channel with the angle specified, and width at the top as 1 mm and depth d..... 30
Figure 2.5 Drainage channels on aluminum plate covering the entire height 30
Figure 2.6 Schematic of dynamic dip testing apparatus [51], [52]..... 31
Figure 2.7 Metal frame used in dynamic dip testing 31
Figure 2.8 Contact angle measurement apparatus [38]..... 32
Figure 2.9 Heat exchanger assembly (single fin column) used in visualization experiments 32
Figure 2.10 Heat exchanger sample a) visualization tests, b) quantitative measurements 33
Figure 2.11 Drainage channels covering the entire length of the sample 33
Figure 2.12 Some drainage channel designs used in condensation tests 34
Figure 2.13 Drainage channels (square cross section-1x1 mm) inclined at an angle of 45^0 34
Figure 2.14 Schematic of a closed chamber for visualization 35
Figure 2.15 Closed visualization chamber: complete apparatus..... 35
Figure 2.16 Schematic of the table top wind tunnel 36
Figure 2.17 Close fit between the tunnel and the sample and the weighing mechanism 36
Figure 2.18 Temperature measurement locations in the heat exchanger base plate (length of the plate extending beyond the cold plate not shown)..... 37
Figure 2.19 Table top wind tunnel: complete apparatus..... 37
Figure 2.20 Inclined sample arrangement..... 38

Figure 3.1 Effect of fin design on water retention characteristics (dynamic dip tests) 75
Figure 3.2 Cross section of a multi louvered fin showing the effective fin spacing..... 75
Figure 3.3 Effect of channel shapes on condensate retention for fin Design 1 76
Figure 3.4 Effect of channel shapes on condensate retention for fin Design 2 76
Figure 3.5 Effect of changing dimensions on water drainage for rectangular geometry fin Design 1 (dimensions specified as wxd)..... 77
Figure 3.6 Effect of changing dimensions on water drainage for triangular geometry fin Design 1 77
Figure 3.7 Effect of changing dimensions on water drainage for rectangular geometry fin Design 2 (dimensions specified as wxd)..... 78
Figure 3.8 Effect of Number of Channels on Retention for Fin Stock Design 1 for Triangular (45°) Channels 78
Figure 3.9 Effect of number of channels on retention for fin Design 1 for square (1×1 mm) channels..... 79

Figure 3.10 Contact angle on aluminum surface a) before acetone washing, b)after acetone treatment 79
Figure 3.11 Effect of changing surface wettability on retention characteristics for fin Design 1 80
Figure 3.12 Comparison of fin stock designs using the small wind tunnel tests 80
Figure 3.13 Effect of different channel geometries on condensate retention behavior of fin Design 1 (actual condensate retention tests) 81
Figure 3.14 Effect of changing dimensions and orientation of the rectangular shaped channels on condensate retention characteristics of fin Design 1 81
Figure 3.15 Spilling of the condensate onto the fin-channel intersection [36] 82
Figure 3.16 Effect of changing dimensions of the triangular shaped channels on condensate retention characteristics of fin Design 1 82
Figure 3.17 Effect of drainage channels on condensate retention of fin Design 2 83
Figure 3.18 Effect of drainage channels on retention characteristics of fin Design 3 83
Figure 3.19 Effect of drainage channels on retention characteristics of fin Design 4 84
Figure 3.20 Effect of inclining sample at 15^0 to the vertical on the condensate retention of Design 1 84
Figure 3.21 Typical humidity and air temperature measurement data 85
Figure 3.22 Effect of inlet relative humidity on the condensate retention of fin Design 1 86
Figure 3.23 Linear fit showing the effect of inlet relative humidity on steady state retention of fin Design 1 86
Figure 3.24 Effect of drainage channels at high humidity (95-96%) on fin Design 1 87
Figure 3.25 Effect of air velocity on the condensate retention characteristics 87
Figure 3.26 Linear fit showing the effect of air velocity on steady state retention of fin Design 1 88
Figure 3.27 Effect of air velocity on the drainage channel performance 88
Figure 3.28 Linear fit showing the dependence of final retention on fin base temperature 89
Figure 3.29 Formation and growth of inter-fin bridges at fin base 89
Figure 3.30 Air velocity profile at the exit of fin column for fin Design 1 90
Figure 3.31 a) Downstream and b)front view of fin design 1 at the initial stages of the experiment 90
Figure 3.32 Schematic diagram of draining pattern at fin outlet for fin design 1 at a) t=35-40 min, b) 55-60 min, c)t= 75-80 mins, after the start of the experiment 91
Figure 3.33 Schematic diagram of draining pattern at fin outlet for fin design 2 at a) t=35-40 min, b) 55-60 min, c) t= 75-80 mins, after the start of the experiment 92
Figure 3.34 Forces acting on a droplet near a drainage channel [36] 93
Figure 3.35 Draining occurring through drainage channels 93
Figure 3.37 Growth of fin bridge for the triangular fins tested by [36] 94
Figure 3.36 Effect of drainage channels: pulling and spilling 94
Figure 3.38 Drainage occuring due to shape of fins of Design2 95

Figure 4.1 Drainage channels incorporated in full size heat exchangers 108
Figure 4.2 Full size heat exchanger with drainage channels: a sample design 108
Figure 4.3 Percentage change in heat transfer rate caused by drainage channels with Reynolds number for fin Design 3 109
Figure 4.4 Percentage change in heat transfer rate caused by drainage channels with inlet

relative humidity for fin Design 3 109
Figure 4.5 Variation in latent and sensible heat transfer rates caused by drainage channels with varying inlet relative humidity for fin Design 3 110
Figure 4.6 Percentage change in heat transfer rate caused by drainage channels with varying mass flow rate of coolant for fin Design 3 110
Figure 4.7 Maximum percentage change obtained in the heat transfer rates by using drainage channels with different fin designs 111
Figure 4.8 Percentage change in pressure drop caused by drainage channels with Reynolds number for fin Design 3 111
Figure 4.9 Maximum percentage change obtained in the pressure drop by using drainage channels with different fin designs 112

List of Tables

Table 2.1 Channel geometries and dimensions used in the study 39
Table 2.2 Geometrical description of the fin stock designs 39

Table 3.1 Static retention data for design 1 samples (dynamic dip tests) 96
Table 3.2 Static retention data for design 3 and design 4 samples (table top wind tunnel tests) 96
Table 3.3 Static retention data for design 1 and design 2 samples (table top wind tunnel tests) 97
Table 3.4 Effect of sample inclination on the static retention of fin Design 1 97
Table 3.5 Effect of inlet relative humidity on the static retention of fin Design 1 97
Table 3.6 Fin gap and louver gap for all fin designs 98

Table 4.1 Sample inlet conditions and the calculated values showing the difference in heat transfer and pressure drop through the drainage channels for a full size heat exchanger 113

Table A.1 Total air side area calculations for all fin designs 131

Table B.1 Uncertainty in Design 1 samples (dynamic dip tests) 142
Table B.2 Uncertainty in some of the Design 2 samples (dynamic dip tests) 142
Table B.3 Uncertainties in contact angle measurements 143
Table B.4 Systematic errors and sensitivities of the measurements 143
Table B.5 Uncertainties and their effect for a sample case (fin Design 1 baseline) 143
Table B.6 Absolute and relative uncertainties associated with Design 1 and Design 2 samples 144
Table B.7 Absolute and relative uncertainties associated with Design 3 and Design 4 samples 144

Table C.1 Regression constants for the j-correlation [31] 156
Table C.2 Regression constants for f- factor correlation [31] 156
Table C.3 Regression constants for the wet multiplier for j-factor [41] 156
Table C.4 Regression constants for the wet multiplier for f-factor [41] 157
Table C.5 EES Code listing for calculating the heat transfer and pressure drop 158

Nomenclature

Roman Symbols:

A_{fin}	air side fin heat transfer area (mm^2)
A_{tube}	air side tube heat transfer area (mm^2)
A_{total}	air side total heat transfer area (mm^2)
b_f	slope of enthalpy curve (kJ/kg-K)
B_R	absolute systematic standard uncertainty of a result
C	heat capacity (kW/K)
C_p	specific heat capacity (kJ/kg-K)
d	depth of the drainage channel (mm)
$D_{H2O,air}$	binary mass diffusivity of water in air (m^2/s)
d_t	tube minor diameter (mm)
D	fin depth (mm)
D_H	hydraulic diameter (mm)
f	fanning friction factor
F_d	air-side flow depth, or fin depth (mm)
F_p	fin spacing (mm)
$F_{p,eff}$	fin gap (mm)
F_w	fin width (mm)
g_m	mass transfer coefficient (kg/m^2-s)
G_c	air mass flux at minimum cross-sectional area (kg/m^2-s)
h	heat transfer coefficient (W/m^2-K)

H	vertical length of heat exchanger (mm)
i	enthalpy of air (kJ/kg)
j	Colburn *j*- factor
K_c	entrance pressure loss coefficient
K_e	exit pressure loss coefficient
L_p	louver spacing (mm)
L_g	louver gap (mm)
L_{NL}	non-louvered length (mm)
L_w	louver width (mm)
$\dot{m}_a$	air mass flow rate (kg/s)
$\dot{m}_c$	mass deposition rate of condensate (kg/s)
$\dot{m}_{cool}$	coolant mass flow rate (kg/s)
$\dot{m}_d$	drainage rate (kg/s)
$\dot{m}_{da}$	dry air mass flow rate (kg/s)
mf	mass fraction
M_A	mass per unit area (g/m^2)
NTU	number of transfer units
N_f	total number of fins across the height of heat exchanger
N_{LB}	number of louver banks
ΔP	air side pressure drop across heat exchanger (Pa)
Pr	Prandtl number
$\dot{Q}$	heat transfer rate (kW)

R	thermal resistance (K/W)
Re_{L_p}	Reynolds number based on louver spacing
Sc	Schmidt number
Sh	Sherwood number
S_R	absolute random standard uncertainty of a result
t_{95}	coefficient for student's t-distribution
t_p	tube spacing (mm)
T	Temperature (K)
U_{95}	overall uncertainty for 95% bounds
U_R	combined standard uncertainty of a result
v_{air}	air velocity (m/s)
w	width of the drainage channel (mm)
W	width of heat exchanger (mm)
$\bar{X}$	calculated sample mean

Greek Symbols:

α	louver angle (°)
β	mass transfer driving force
δ	fin thickness/thickness (mm)
ε	effectiveness
η	fin efficiency
θ	included angle (°) for a triangular drainage channel
θ_F	evaporator inclination (°)

θ_i	absolute sensitivity coefficient of a parameter
θ_R	receding contact angle
μ	estimated population mean
σ	area contraction ratio (A_{min}/A_{fr})
Φ	relative humidity (%)
φ_j, φ_f	wet-surface multipliers for Colburn *j*- and *f*- factors
ω	humidity ratio (kg/kg)

Subscripts:

air	air-side
b	fin base
c	cross sectional
ch	channeled
cool	coolant
f	fin
fb	front and back
fg	latent (used with enthalpy)
in, i	inlet conditions
lat	latent
lm	log mean
out, o	outlet conditions
s	surface
sens	sensible

v	velocity
w	water vapor

Chapter 1 - INTRODUCTION

1.1 Introduction

Contemporary automotive manufacturers are making a strong effort to reduce the space occupied by various components of the automobile and provide maximum cabin space. As a part of this larger effort, the size of automotive evaporators is being reduced, resulting in increasingly complex geometries on the air side of these heat exchangers. Typically, highly compact louver-fin heat exchangers are used in the automotive systems, as they occupy small volume and have the ability to provide high amounts of heat transfer. These compact heat exchangers are also commonly used in such air-conditioning and heat pumping applications that undergo dehumidification and defrosting processes. Under wet or frosted conditions the heat-transfer performance can drop. In these exchangers, the air side thermal resistance accounts for approximately 80% of the total resistance. [1] Consequently, large surface areas per unit volume and heat transfer enhancement techniques are important. Improving the efficiency of these complex heat exchanger systems is an important issue and has attracted significant research attention.

When the air-cooling heat transfer surfaces of a heat exchanger operate below the dew point of the air flow, condensate forms on these surfaces. The condensate remains there until removed by the forces of surface tension, shear, or gravity, or until it evaporates in the off cycle. The retained condensate can have a severe impact on the overall performance of the heat exchangers. It can cause reduced heat transfer, increased pressure drop, water carry-over, and unhealthy microbial activity. The detrimental effects of condensate retention are especially important for compact louver-fin automotive evaporators, as they have very high surface-area-to-volume ratio and

highly interrupted and complex fin structure. Condensate bridges readily form in the small louver and fin gaps, and cause related changes in heat transfer and friction performance. Figure 1.1 shows the images of accumulated condensate in automotive evaporators. So an effective method of condensate removal is highly desirable.

Currently, surface wettability modification by a chemical coating or some other means, is widely used to promote drainage. The operating environment of the automotive heat exchangers typically causes progressive surface fouling, including the effect of corrosion and particle accumulation. Simmons *et al.* [2] showed that the conditions surrounding the automotive heat exchangers can promote persistent fungal colonization, and hence affect the long term performance of the surface treatments. Drainage channels in the form of integrated long grooves on the tube surfaces might provide an excellent long-term solution for condensate management in compact heat exchangers. The goal of this research is to explore the capabilities of drainage channels in reducing the condensate accumulation and improving the overall performance of compact louver-fin heat exchangers. The work will be used as a guideline in selecting a promising possible channel geometry for obtaining a reduction in condensate retention, and hence improved performance for a given fin design specification.

1.2 Literature Review

1.2.1 Condensate Retention Characteristics and Related Effects: Earlier Studies

Bryan [3] was among the first to study heat transfer performance under wet conditions. For a bare tube surface coil under dehumidifying conditions, he reported that heat transfer coefficient and the friction factor under wet conditions were higher than those under dry conditions. However, later, Bryan [4] concluded that the heat transfer coefficient was greater in dry conditions, when he presented experimental data for heat and mass transfer on dehumidifying

extended surface coils. The difference was due to the condensation on fin surfaces in the latter case, which caused a decrease in fin-coil surface effectiveness.

Bettanini [5] conducted numerous experiments on simultaneous heat and mass transfer to a vertical surface. An enhancement in the sensible heat transfer coefficient under wet conditions was reported. He hypothesized that the increase in sensible performance was due to surface roughness caused by the condensation. He reported that the mass transfer affected the heat transfer and relative coefficients. Two types of experiments were conducted, one with the soap and water solution sprayed on the surface to temporarily cause filmwise condensation, which later changed to the dropwise mode, and the other with gypsum chips to simulate water droplets on the surface. It was also observed that heat transfer coefficient is higher for dropwise condensation mode, because of effect of surface roughness. The experimental procedure and apparatus used in these experiments, however was simple. Thus, the experimental results which show that the thermal performance increases due to condensation cannot be directly applied to more complicated heat exchangers.

Yoshii *et al.* [6] studied the effects of dropwise condensation on the pressure drop and heat transfer performance of wavy-fin heat exchangers. Owing to condensation, the pressure drop was found to increase by 50-100% over the dry-surface conditions. From the experiments performed on the scale-up models of heat exchangers and dye-in-water flow visualization, Yoshii and coworkers concluded that the location and shape of the droplets play important roles in determining the overall impact of condensate on the performance. Guillory and McQuiston [7], and later McQuiston [8] reported an enhancement of 30% in heat transfer coefficient for developing flow between horizontal flat plates under wet surface conditions. Tree and Helmer [9] found that heat transfer and pressure drop were unaffected in the laminar regime but an effect

was observed in the turbulent regime, for experiments performed on the parallel plate heat exchangers under wet conditions.

Jacobi and Goldschmidt [10] found a decrease in the heat transfer coefficient at low Reynolds number, but an increase at high Reynolds number, under wet conditions for circular-finned tubes. They suggested that their results were due to condensate retention. At low Reynolds numbers, water was retained causing degradation in the performance, while at high Reynolds numbers, vapor shear removed the condensate and the heat transfer increased due to the surface roughness.

Korte and Jacobi [11] studied the condensate retention characteristics and effects on air-side performance of plain-fin-and-tube heat exchangers. They conducted experiments under both dry and wet conditions. It was found that the steady-state condensate retention per unit heat transfer area, the heat transfer performance and the friction factor under wet conditions were all dependent on fin spacing. The quantity of retained condensate per unit area decreased with decreasing fin spacing from 6.35 mm to 2.12 mm. The effect of air flow on the condensate retention was more or less inconclusive, as increasing the air flow rate increased the retention for some exchangers, while decreased for others. For heat exchanger with fin spacing 6.35 mm, an enhanced sensible heat transfer performance was observed. With the fin spacing as 3.18 mm, the heat transfer coefficient was found to be sometimes lower and sometimes higher than the dry conditions.

Yin and Jacobi [12] studied the condensate retention characteristics and its effect on the thermal hydraulic performance of plain-fin and wavy-louvered fin heat exchangers. The heat exchangers, exposed to an air velocity range of 0.8 to 2.0 m/s, exhibited retention characteristics independent of the flow velocity, but dependent on the fin geometry and contact angles. For both type of

exchangers, the condensate mass retained per unit heat transfer area increased with decreasing fin spacing. At the same fin spacing, the quantity of condensate retained for the plain-fin heat exchanger was 10-20% less than for the wavy-louvered heat exchanger. For wet surface conditions, the wet Colburn *-j* factor decreased, and the decrease was greater at smaller fin spacing, as greater amount of water was retained with lower fin spacing.

Kim and Jacobi [13] also found a decrease in the heat transfer performance of both plain and slit-fin, round tube evaporators, when comparing wet conditions to dry conditions. The increased pressure drop and the decreased heat transfer were concluded to be caused by the blockage effect of the condensate retained on the fins. Under wet conditions, the sensible j factor was also found to be dependent on the number of tube rows for plain–fin-and-tube exchangers and the fin spacing for slit-fin-and-tube heat exchangers. *j* factors increased as the fin spacing was increased. The effect of fin spacing on the real time retention was also found to be significant for plain-fin-and-tube heat exchangers. For smaller fin spacing, an overshoot was observed before reaching the steady-state mass of retained condensate. The time required to reach the steady-state was longer and the steady-state value of retained condensate was higher at lower velocities. For slit-fin-and-tube heat exchangers, an oscillation in the condensation rate was seen at higher velocities, due to the shedding effect. Plain-fin-and-tube exchangers retained less condensate than the slit-sin-and-tube exchangers with same fin spacing and number of tube rows. A larger fin spacing for the slit-fin-and-tube exchanger resulted in higher mass of retained condensate.

1.2.2 Studies Related to Automotive Louver-fin Heat Exchangers

Most of the studies related to louvered fin heat exchangers have been reported in terms of overall heat exchanger performance. There have been fewer studies focused on the detailed flow field and heat transfer measurements within the heat exchangers. Kays and London [14] were among

the first to publish the data on louver fin surfaces, but the geometries of the surfaces they studied were a lot different from those currently used. Later, Kays and London [15] published a compilation of heat transfer and pressure drop measurements for a large number of heat exchanger designs. Beauvais [16] was one of the first to conduct flow visualization experiments on the louvered fin array. He found that louvers tried to realign the airflow parallel to them rather than acting as surface roughness that enhanced the heat transfer performance.

Davenport [17], [18] performed experiments similar to those of Beauvais and revealed that the flow pattern could be characterized in terms of duct-directed or louver-directed flows, depending on the Reynolds number. He found that at low Reynolds number there was a flattening of the *j*-factor curve, caused by the transition from louver-directed to duct directed flow. He also reported a comprehensive study of non-standard variants of the flat-tube and louvered-fin heat exchangers and developed correlations for them. The fin spacing and the hydraulic diameter do not contribute to the correlations. He found louver spacing to be more relevant than hydraulic diameter and fin spacing for the basis of the Reynolds number. His experiments and correlations showed that the Colburn j and Fanning friction factors tend to decrease with smaller louver angle, and the j-factor increases with a larger louver length.

Kajino and Hiramatsu [19] performed detailed flow visualization experiments on louver-fin arrays using dye injection and hydrogen bubble techniques. They found the dominance of fin directed flow for larger fin spacing and louver-directed flow for small fin spacing. Achaichia and Cowell [20] tested 15 samples of louvered plate-fin heat exchangers with one or two tube rows. These samples showed higher Colburn j-factors than the conventional serpentine louver fin heat exchangers. At low Reynolds number, the Stanton number approached the solution for laminar flow in a duct. Flow in this range is dominated by the fin directed flow. At high Reynolds

numbers, a plot between Stanton number and the Reynolds number becomes parallel to the solution for laminar flow over a flat plate. The flow in this region is dominated by louver-directed flow. In the middle range of Reynolds number, because of the transition from the fin directed to the louver directed flow, flattening of the St curve was observed. Achaichia and Cowell [21] also performed numerical studies on an infinite array of zero thickness louvers and obtained and expression for flow angle. Webb and Trauger [22] performed flow visualization studies that showed the relationship of flow alignment with louvers for different louver angles, louver spacinges and fin spacinges. They developed a correlation for flow efficiency, defined as the ratio of transverse flow path length to ideal transverse flow path length. Their description of the flow supports that of Davenport [17].

Webb and Jung [23] compared the performance of louver-finned, flat-tube heat exchangers with that of plain-fin-round-tube heat exchanger. They described the advantages of the flat-tube design, identifying the flat-tube heat exchangers have airflow normal to all louvers, no existence of tube-wake region which decreases heat transfer downstream of round tubes, a lower profile drag and a higher fin efficiency. Suga and Aoki [24] conducted a 2-D numerical analysis of louver fin geometries and obtained the optimum louver angle, keeping the ratio of fin spacing and louver spacing constant. Cui and Tafti [25] performed numerical studies on a 3-D fin geometry and found an increase in the heat transfer for smaller unlouvered length. However, they also concluded that complete elimination on un-louvered fin length can decrease the heat transfer. In a study similar to that by Suga and Aoki [24], Kim *et al.* [26] performed experiments on 12 louvered-fin heat exchangers and reported an optimal range of louver angle for maximum performance.

There have been numerous experimental studies of the louvered fin geometry which have reported correlations relating the heat transfer characteristics to the fin parameters. Some of the commonly used correlations include those by Chang and Wang [27] and Chang *et al.* [28], who developed generalized correlations for the j and f factors. Their correlation was based on the experimental data from 91 multi-louvered fin heat exchangers, including the results from previous studies of the past 20 years. The correlations developed by Kim and Bullard [29] correlations for the j and f factors were based on experiments performed on 45 louver-fin exchangers and 225 data sets. Dang *et al.* [30] provided the heat transfer and pressure drop correlations based on 20 different multi-louvered fin and flat tube heat exchangers. The correlations show a significant effect of fin length and fin spacing on the heat transfer coefficient and the pressure drop as a function of frontal air velocity. Recently, Park and Jacobi [31] developed correlations for the j and f factors based on experiments performed on 126 different louver-fin heat exchangers at 9 laboratories. This comprehensible database consisted of 1030 heat-transfer and 1270 pressure-drop measurements.

Much of the research related to automotive louver-fin heat exchangers has been directed at dry performance and fewer studies have been conducted for wet exchanger performance. Wang *et al.* [32] tested two different louver-fin, serpentine type evaporators under dry and wet conditions. They found that both the heat transfer coefficient and the pressure drop under the wet conditions were higher than those under the dry conditions. They concluded that the fin surface roughness was increased due to the water droplets, which increased the pressure drop. The heat transfer coefficient increased because the additional surface roughness enhanced turbulent mixing. However, they calculated the wet fin efficiency based on McQuistion's method [33], which is

overly simplistic. Thus the reported fin efficiency and the heat transfer coefficient depended significantly on relative humidity.

The work on the wet air-side performance of automotive evaporators has mostly been reported in terms of overall heat exchanger performance. Very few studies are found in the open literature that focus on the condensate retention, management, and drainage characteristics of automotive compact heat exchangers. Osada *et al.* [34] provided early quantitative measurements and visual observations for the wet air-side performance of automotive evaporators. They performed heat transfer and visualization experiments on single fin columns of multi-louvered flat tube evaporators. They assessed the effects of louver geometry, inclination angle and the surface wettability on the condensate drainage. They concluded that due to condensate louver bridging, the heat transfer coefficient and pressure drop decreased under wet conditions for samples with a narrow louver opening. They reported that the fin surface characteristics near the air-flow-exit face of the heat exchanger significantly affected the condensate drainage behavior. From condensate visualization experiments, they found that a significant amount of water accumulates and drains on the downstream side of the heat exchanger, and hence they suggested that it is critical to increase the wettability of the tube surface near the outlet of the evaporator (Figure 1.2). The louver-cut length also affected the condensate drainage. Increasing the louver-cut length decreased the amount of louver blockage. They found an improved performance by an inclination of the core to the upstream direction. They argued that an improved drainage was achieved because; the gravitational force and the air flow friction opposed each other and formed a balanced distribution of condensate retention. However, this finding contradicts a report by Kim *et al.* [35], who obtained favorable results by a core inclination towards the downstream direction.

In a study similar to that by Osada *et al*. [34], McLaughlin and Webb [36] used a table-top apparatus to conduct experiments on single column of louvered fins which was brazed to a refrigerant tube. Their setup allowed the visual observation of the formation and the subsequent drainage of the condensate. They studied the impact of fin geometry on drainage characteristics and retention. They conducted single-fin tests with an air flow of 2.5 m/s and inlet relative humidity greater than 95%. They provided the tube-side cooling by cold water which was circulated through a tube brazed to one side of the fin. This allowed optical access through glass on the other side of the fin. Initial drop-wise condensation changed to film-wise condensation, as the drops quickly grew and coalesced to form a film. They found that condensate layer is thin near the leading edge and it thickens along the air-flow direction. More condensate bridges occurred near the bottom of the specimen. They provided conjecture on condensate drainage paths based upon the pattern of retained condensate. They also performed dip tests on the sample for the quantitative measurement of the retained condensate. They reported that retention increased with decreasing the louver spacing. There was a reduction of 26% in the condensate retention when the louver spacing was changed from 1.1 mm to 1.3 mm. However, the effect of fin spacing on retention was inconclusive--condensate mass per area was largest for F_p=2.4 mm, 1.6 mm, and then 2.0 mm. In a similar study [37], they found that heat transfer coefficient decreased under wet conditions compared to dry conditions, but the effect was negligible for the larger louver spacing (1.3 mm). Air-side pressure drop decreased under wet conditions for the smaller louver spacing. Also, under wet conditions, they found a 30-40% increase in heat transfer coefficient and 10-15% higher pressure drop for a louver spacing of 1.3 mm in comparison to 1.1 mm. They justified the effect of louver spacing in terms of condensate blockages between the louvers, which can more easily form for lower louver spacing, and the

blockage can change the flow from louver-directed to duct-directed, hence reducing the heat transfer. The authors reported that the sensible heat transfer and the pressure drop was similar under dry and wet conditions for fin spacing=2.4 mm, but the heat transfer decreased and the pressure drop increased for fin spacing=1.6 mm. They explained this observation on the basis of condensate forming inter-fin bridging when the fin spacing is smaller.

Kaiser and Jacobi [38] studied the thermal-hydraulic performance and the retention characteristics of automotive evaporators. They found that the sensible heat transfer coefficient decreased and the air-side pressure drop increased under wet conditions. This effect was larger for smaller louver spacing. They also found that the difference between the wet and dry performance decreased with an increase in the air-side Reynolds number. Their data also show that a small louver spacing and a large louver angle increased the heat transfer and pressure drop. Steady-state retention results obtained by Kaiser and Jacobi showed a large influence of frontal velocity on the quantity of retained condensate for all tested heat exchangers. They observed two distinct drainage patterns in the dynamic drainage tests: fast drainage heat exchangers which reached the steady state within 120 seconds, and the sustained-drainage heat exchangers, which took almost 4 hrs to reach steady state. The sustained-drainage pattern was attributed to louver bridging, and these bridges are difficult to be removed by gravitational forces.

Tang and Jacobi [39] also found that the heat transfer decreased and the air-side pressure drop increased under wet conditions. They reported that the fin spacing and the louver length are the critical dimensions in determining the condensate retention. The difference in the wet and the dry performance varied from 10-100% and the clogging of the louvers under wet condition was claimed to be the major reason. The friction factor increased from 10 to 70% over the dry conditions, depending upon the fin geometry. The heat exchangers with smaller fin and louver

spacing had more pressure drop. The retained condensate decreased the effective minimum flow area, causing an increase in the pressure drop. Kim and Bullard [40] performed experiments under wet conditions on flat-tube louver-fin heat exchangers, and measured the heat transfer and pressure drop. They tested 30 samples and assessed the effects of Reynolds number, louver angle, fin depth, and fin spacing on the wet exchanger performance. They found that with increasing louver angle, both the sensible heat transfer and the pressure drop increased. The pressure drop was larger under wet conditions as compared to the dry case. The pressure increase ratio was more than 1 for most of the cases and even greater than 2 for some cases. The heat transfer coefficient for the wet conditions varied from 0.7 to 1.6 times that of dry conditions. They did not consider the effects of surface wettability in their correlations for the *j*- and the *f*- factors for wet conditions.

Recently Park and Jacobi [41] explored the effects of fin geometry and operating conditions on the air-side thermal-hydraulic performance of flat-tube heat exchangers. They conducted experiments on exchangers with louvered, wavy, and plain fins under dry and wet conditions in a closed-loop calorimetric wind tunnel. The heat transfer and friction performance were measured at face velocities ranging from 0.5 m/s to 2.8 m/s for dry- and wet- surface conditions. They found that the fin spacing has the most significant impact on the *f*- and *j*- factors, especially at high Reynolds number. Louver spacing was found to have more impact on the performance under the wet conditions than under the dry conditions. Both *f*- and *j*- factors decreased with smaller louver spacing under wet conditions. They found that core inclination improved the condensate drainage and hence the thermal-hydraulic performance under the wet conditions. The authors also developed new empirical correlations for the *j*- and the *f*- factors for flat-tube,

louver-fin heat exchangers. They provided correlations for wet conditions using the wet-surface multipliers for both *f*- and the *j*- factors.

Thus, with some exceptions, most of the literature available points out the fact that condensate retention causes degradation in the thermal-hydraulic performance under the wet conditions. The geometrical parameters affect the condensate drainage characteristics, and hence have an effect on the overall performance.

1.2.3 Improving the Thermal-Hydraulic Performance

There have been numerous attempts to improve the thermal-hydraulic performance of louver-fin heat exchangers. The literature is replete with research which has been conducted to provide improvements in the performance. The literature review in this section primarily focuses on the research directed at improving the air-side thermal performance, leading to improvements in the overall performance of the heat exchanger.

The most commonly used method to reduce the impact of condensate on the heat transfer performance of heat exchangers has been to modify the surface wettability through surface treatments. Mostly these treatments are hydrophilic, which reduce the surface tension of water on the aluminum surface. However, recently, there have been findings [42], [43] which show that increasing the static contact angle also improves the performance in some cases. There are different methods which have been used to manipulate the surface wettability of aluminum, they may be categorized as: a) non-reacting material coating on the aluminum surface, b) chemical conversion treatments, in which a material deposited on the surface reacts with aluminum to form a layer of new compound, and c) Using micro-scale topographical manipulations, which modify the contact angle.

Goodremote and Hartfield [44] were among the first to study the effect of a hydrophilic coating on the performance of a serpentine-tube louver-fin automotive evaporator. They found that a hydrophilic coating reduced the pressure drop but did not change the heat transfer. However, they did not report the fin geometry in their work. Fu *et al.* [45] investigated the effects of an anti-corrosion coating on the thermal-hydraulic performance of a louvered-fin-and-tube heat exchanger under wet conditions. They conducted experiments on three anti-corrosion coated exchangers with different fin spacing, and one non-coated exchanger. They found negligible effect of the surface treatment on the performance of all types of exchangers tested.

Hong and Webb [46] examined the effects of hydrophilic coatings to improve wettability and thus decreasing the pressure drop under the wet conditions. The experiments were performed on coated and non-coated wavy, lanced and louver-fin heat exchangers, at a fixed face velocity of 2.5 m/s and the ratio of wet to dry pressure drop maintained at 1.2 for the non-coated exchangers. They found that the hydrophilic coatings have no effect on the heat transfer performance. However the coatings decreased the wet-to-dry pressure drop ratio by 45% for louver-fin heat exchangers and 15% for the wavy-fin heat exchangers at velocity of 2.5 m/s. Hong [47] also developed a model to predict the carry-over velocity and compared it to the experimental data. However, he obtained the contact angle data from static-drop goniometer test and did not consider the effect of contact angle hysteresis. An important finding made by Hong was related to the durability of the coating; after around 1000 wetting cycles, the initial contact angle of the coated surface, which was measured to be less than 10^0, increased to the constant value of about 60^0, which was also the value for the non-coated surfaces.

Korte and Jacobi [11] studied the effects of hydrophilic as well as hydrophobic coatings on the condensate retention characteristics and the wet performance of plain-fin-tube heat exchangers.

Interestingly, they found that the surface wettability of an uncoated exchanger increased significantly during the first 100 hours of wet-dry cycling. This increase in the wettability resulted in increase in steady state retention for the heat exchanger with 3.18 mm fin spacing, while caused a decreased retention for exchanger with fin spacing as 6.35 mm. The steady state retention for the hydrophilic coated exchangers was found to be independent of the air face velocity over the range of their study (1.5 m/s to 8 m/s). The hydrophobic coating led to a significant increase in the friction factor under wet conditions. Ha *et al.* [48] studied the thermal-hydraulic performance of wet fin-and-tube heat exchangers and reported that increasing the wettability of the exchangers reduced the time required to reach the steady-state condensate retention. Wang and Chang [49] also investigated the effects of hydrophilic coatings on the heat transfer and friction characteristics of plain-fin-round-tube exchangers. They found that the heat transfer was unaffected by the coatings, while the pressure drop was lowered by 15-40%. Kim and Jacobi [13] found a decrease of around 50% in the steady state condensate retention with the use of hydrophilic coating. They also reported that the sensible j- factor was unaffected by the coating, but the f- factor decreased.

Osada *et al.* [34], while performing experiments on single row of multi-louvered fins, found that a hydrophilic coating at the fin outlet caused a decrease in the pressure drop and increase in the heat transfer coefficient, compared to the non-coated sample. They found the change in the drainage path with the hydrophilic coating as the major reason for reduced condensate retention and improved performance. McLaughlin and Webb [36] found that using the hydrophilic coating though improved the surface wettability, but it reduced the condensate retention only by 12%. However, due to reduction in the fin and louver bridging with the use of hydrophilic coatings, the

heat transfer coefficient was found to increase. Surprisingly, they reported that the hydrophilic coating did not affect the air-side pressure drop.

Though surface wettability modifications using a chemical or a non-reacting coating have been applied the most to reduce the air-side resistance and improve performance, there have been recurrent questions regarding its durability [11], [46], [47]. Evaporators undergo many wet/dry cycles in most operating environments. The coating treatment usually has the tendency to be partially washed away by condensate during repeated wet/dry cycling. Thus more permanent methods of reducing the air-side thermal resistance through the modification of surface wettability have been recently explored. Sommers and Jacobi [42] showed the effectiveness of micro grooves on aluminum surface in increasing the water drainage. They prescribed a method to fabricate controlled micro-scale, topographical features on an aluminum surface to modify its wettability. They found a reduction of 50% in the volume of the water droplet for incipient sliding on the micro-grooved surfaces, which increased the apparent contact angle. In a similar study, Liu *et al.* [43] described a surface-embossing technique to impart micro-scale surface features on the heat exchanger construction material. They found a consistent reduction in the critical sliding angle on surfaces after embossing. They suggested smaller spacing between the parallel micro-grooves (<100 μm), larger depth and steeper side walls for drainage enhancement.

The only study available in the literature on the performance evaluation of drainage channels on the tube walls of louver-fin heat exchangers is from Mclaughlin and Webb [36]. They visualized the drainage characteristics on a single row fin, and measured the condensate retention using dip tests. They tested the drainage channels, which were the refrigerant channels on the formed plate evaporator. In the visualization tests, they noticed that shallow channels (1 mm depth) did not drain any water, while some drainage was observed through 2 mm deep channels. However, in

the condensate retention tests, they found that drainage channels increased the condensate retention. They found increased fin bridging caused by the spilling of the condensate from the shallow drainage channels responsible for this increase. Thus, they concluded that the vertical channels on the air-side tube surface produced little or no enhancement. However, they did not explore different geometries and designs of drainage channels and also their affect on different fin designs. A drainage channel which is ineffective for 1 fin design might be effective for the other. Also, the method to measure the condensate retention used by Mclaughlin and Webb puts question on the reliability of the data.

1.3 Project Objectives

The project is directed at improving the thermal-hydraulic performance of automotive louver-fin flat-tube heat exchangers, by reducing the air-side thermal resistance and pressure drop. Heat exchangers operating under the dehumidifying conditions face the problem of condensate retention leading to decreased thermal performance and other degrading biological effects. Drainage channels in the form of grooves on the tube surface will be explored as the means for improving the condensate drainage behavior of compact heat exchangers. The project objectives include evaluation of various drainage channel geometries and identification of the physical mechanisms for effective drainage by measuring and visualizing water retention and drainage behavior. Dynamic dip tests were performed with different drainage channel designs on different fin designs for quantitative measurements. A visualization test apparatus was designed, which allowed qualitative as well as quantitative measurements. The results from the dynamic dip tests and the condensation apparatus were then used to select the channel-fin design combination to be used in full size heat exchangers. A comparison of fin stock geometric and scale effects on retention and drainage behavior was also made. Full size heat exchangers were designed with

drainage channels incorporated in them. Thermal and pressure drop analysis was then performed based on the correlations available in the literature to assess the effect of drainage channels on the thermal-hydraulic performance. A computer simulation was developed to calculate the change in the heat transfer performance and the pressure drop caused by the drainage channels on the heat exchangers constituting the fin designs tested in the experiments.

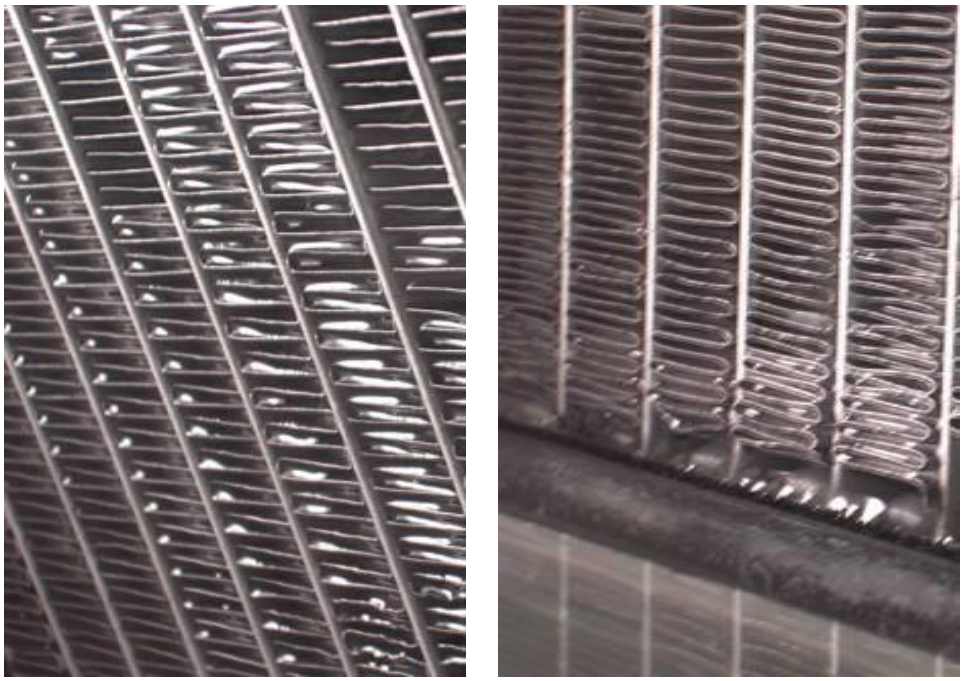


Figure 1.1 Condensate accumulation in louver-fin heat exchangers [50]

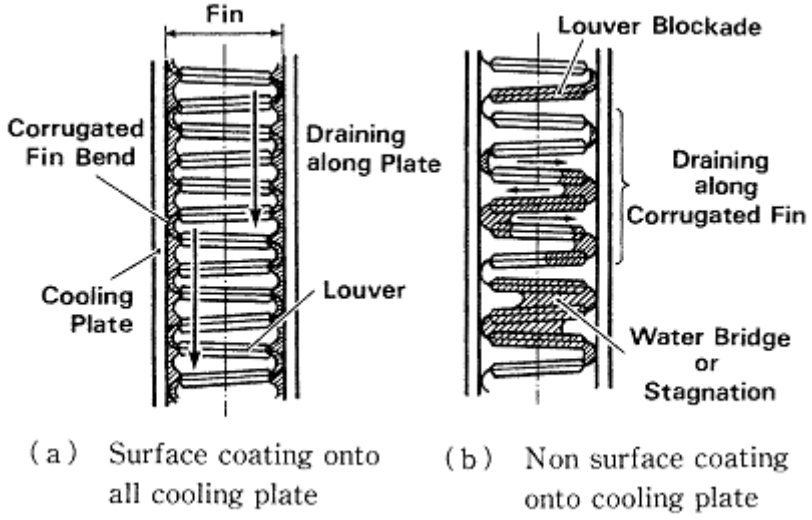


Figure 1.2 Effect of surface coating on the exit of fin column [34]

Chapter 2 - EXPERIMENTAL METHODS

Dynamic dip testing was first used to qualitatively assess the effect of drainage channels on the condensate retention of single row louver fin heat exchanger. The qualitative results obtained from the dip tests were further confirmed from the real time condensation experiments performed in a small wind tunnel. An open loop table top wind tunnel was designed and constructed for the quantitative measurement as well as for visualization of the condensate drainage behavior on the single row louver fin heat exchanger sample. This chapter describes the heat exchanger samples used, different fin designs, drainage channels designs selected, the experimental apparatus and procedure.

2.1 Dynamic Drainage Tests

2.1.1 Heat Exchanger Sample

The dynamic drainage experiments were conducted on a simplified compact heat exchanger made by placing multi-louvered fin stock between two aluminum plates as shown in Figure 2.1. The side aluminum plates acted as the surrogate flat tubes. A similar arrangement was used by Osada *et al.* [34] in their experiments. The plates and the fin stock were held together using an aluminum clamp and screw assembly (Figure 2.2), ensuring the vertical orientation of the exchanger for experiments. A spirit level was used to ensure that the fin stock had the same orientation as the side aluminum walls, every time the sample was reassembled. The clamp and the screw assembly had countersinks and holes (Figure 2.3), which enabled it to be attached to a stable metal frame, again to ensure same vertical orientation every time the experiment was performed. Two different designs of louver-fins were used in these experiments (Explained later in section 2.4). Same sample of fin stock was used for a given fin stock design for multiple experiments.

2.1.2 Drainage Channel Designs

Various drainage channels were fabricated in the form of long vertical grooves on the sides of the aluminum walls in contact with the fin stock. The channels were thus in contact with the fin stock on both sides. The fabricated designs had variations in geometry, dimensions, and positioning across the plates—the actual values were based on manufacturability and guided by earlier work. Cross sections of some of the channel designs are shown in Figure 2.4. Geometries selected for the dynamic dip testing were rectangular, triangular, and trapezoidal. The width and the depth were varied for the rectangular channels, i.e., the aspect ratio, and the width and the included angle were varied for the triangular ones. The length of the channels was made equal to the fin stock length, i.e., they covered the entire vertical height of the sample (Figure 2.5). For the dynamic dip tests, the number of channels across the entire fin depth varied from one to two. The single channel was placed at the center, while the two channels were placed equally distributed across the depth.

2.1.3 Dynamic Dip Testing Apparatus

The fabricated samples were tested using a dynamic dip testing apparatus, developed by Zhong *et al.* [51], and later explored and tested in detail by Liu *et al.* [52]. The apparatus is shown in Figure 2.5. It consists of a large water tank, with a smaller submerged air tank to control water level by displacement of water using compressed air, and a structure to suspend and weigh the sample. Air was supplied to the displacement tank by a pressurized air line. The air vent allowed the air to quickly leave the displacement tank when the vent valve was opened. The water used was normal tap water with impurities removed. Since the sample size was much smaller than those typically tested in this apparatus, more accuracy was required. In order to achieve the accurate and stable vertical alignment of the sample, a metal frame was used to suspend the

samples from the balance. The frame is shown in Figure 2.7. The frame consisted of a plexiglass plate, which was directly kept on the scale. The plexiglass plate had two threaded stainless steel rods attached to it, which were attached to the aluminum block. Threaded rods were used so as to adjust the orientation and level of the bottom aluminum block. The bottom aluminum block had a vertical slot which enabled the attaching of the heat exchanger, assembled though the clamp and the screw assembly, in a proper vertical orientation. The frame was kept over an electronic balance (Sartorius GP-8201), having an accuracy and readability of 0.1 g. The data were transferred to the computer through an RS-232 interface at the balance. The recording interval of the acquisition system used was 0.18 sec. The data were processed using the software WINWEDGE.

2.1.4 Conditions and Procedure

The heat exchanger was first assembled with the clamp and screw assembly, after washing the fin stock and the aluminum plates with acetone solution and drying them completely using compressed air. The clamped sample was then attached to the frame, kept over the electronic balance. Once the sample was suspended on the electronic scale over the reservoir, the experiment was initiated by setting the balance to zero. The water level in the tank rose as the compressed air supply was opened, and the sample was submerged. Before opening the air supply, a final alignment check, using a spirit-level was performed. Once the specimen was fully submerged, the air supply was closed. Since the heat exchanger sample has complex geometrical features, there may be air trapped in the fin stock. The water surrounding the sample was vigorously agitated. Bubbles formed on the sample surface, if any, were removed using a paint brush. The data acquisition system was started, and the air vent was suddenly opened completely to allow water lever to drop quickly.

As water drained from the specimen, the amount of water retained on the sample was recorded by the computer-based data acquisition system. Multiple runs were conducted on a given sample to assess the repeatability of the experiment. As discussed later, the uncertainty in the experiments was higher than the uncertainty of the balance, due to other factors and the relatively small size of the samples. In order to obtain statistics on the experiments, 20 identical tests were performed on a selected sample. The uncertainty in the measurements was estimated from instrument uncertainties (~0.1 g for the balance) and the statistical data (see Appendix-B). For the remaining samples, 5-6 readings were recorded and then the average results were reported.

2.2 Contact Angle Measurements

Sessile-drop contact angle measurements on the aluminum surface were performed using digital photography and image analysis technique. The test set-up used is similar to those used in prior work [38], [52], and was used here to measure the static contact angle of water on aluminum surfaces. The experimental set-up is shown in Figure 2.8. A droplet of distilled water was placed on the test surface in the horizontal position using a micro-syringe. The surfaces used were aluminum side plates, which acted as the tubes. The profile images of the droplets were recorded using a KAP-PA DX 10-1394a high-resolution CCD camera (magnification up to 25 x) from a location in plane with the base. Image analysis software (Kappa ImageBase- provided with the camera) was used to process the images and determine the contact angles. Droplets in the range from 5 µL to 25 µL were injected onto the test surface and two independent measurements were recorded for each droplet volume. For each droplet, two angles (on either end of the droplet) were measured and the average value was taken to be the static contact angle, and 20 different measurements were obtained for a given surface. These data provide some general measure of surface wettability, but advancing and receding contact angles were not measured.

2.3 Real Time Condensate Retention and Visualization Tests

After the dynamic dip testing of the heat exchanger samples, actual condensate experiments were performed. The heat exchanger sample was redesigned. Some new channel designs were also explored. The real-time tests included quantitative measurements as well as qualitative observations.

2.3.1 Heat Exchanger Assembly

In the actual condensation experiments, the heat exchanger sample was again taken to be a single row of fin stock. For the visualization experiments using the wind tunnel apparatus, a glass plate was used on one side, and an extended aluminum plate was used on the other side; the whole assembly was clamped and attached to the thermoelectric device (Figure 2.9). The attachment of the sample to the thermoelectric device was done through the means of screws and countersinks on the thermoelectric device. For the quantitative measurements (i.e., the mass the real-time mass measurements), the glass plate on one side was replaced by an aluminum plate (Figure 2.10), so as to have metal plates on both sides on the fin stock, in order to more realistically mimic the heat exchanger.

2.3.2 Drainage Channel Designs

As in the dynamic drainage experiments, the drainage channels were engraved as vertical grooves on the aluminum plates surrounding the fin stock. For visualization tests, the channels were made only on one side, which was attached to the thermoelectric device. The channels extended along the whole length of the plates. Shown in Figure 2.11 is the positioning of the channels on the aluminum base plate. For all experiments, three equi-spaced channels along the entire depth of the fin stock were used. The geometries tested included rectangular, triangular and trapezoidal. Some of the drainage channels are shown in Figure 2.12. The geometries and

dimensions were based on the results from the dynamic drainage testing. The channels selected were some of the best performers in the dynamic drainage tests. In addition to the vertical ones, channels inclined to the vertical were also tested. Figure 2.13 shows one such channel design, in which the channels were inclined at 45^0 to the vertical. The inclined channels were square in geometry, and drained the condensate into a vertical main channel, through which the final drainage occurred. Finally, the various channel geometries and dimensions tested with the dynamic drainage and the condensation experiments are summarized in Table 2.1.

2.3.3 Closed Peltier Chamber

A closed chamber was first designed for the visualization tests. The chamber design was adopted from previous research [42], with slight modifications. The basic design of the closed chamber is shown in Figure 2.14. However, this approach was abandoned, for the reasons discussed later, and was not used to conduct experiments. Instead, a table-top wind tunnel apparatus was designed and was used in experimentation.

2.3.4 Table-Top Wind Tunnel Apparatus

The apparatus was a table-top wind tunnel, providing air at desired humidity and temperature to the heat exchanger sample. A schematic of the apparatus is shown in Figure 2.16. The apparatus consisted of a DC fan (Dayton 2RTJ6 Square Axial Fan, 170 cfm, 14.4W) with variable speed using a DC power supply. The fan was mounted on a frame, which was open to the ambient air, and also to the humidifier discharge. The two humidifiers (Honeywell HWM Warm Mist Humidifiers) had adjustable valves for maintaining a desired humidity level. The fan supplied the moist air to a large mixing chamber. The mixing chamber and the tunnel assembly were made of plexiglass.

The moist air then passed through a honeycomb straightener into the tunnel. The exit of the tunnel fit closely to the sample, without touching it, minimizing air leakage and allowing for the weight measurement (Figure 2.17). The humidity and the dry bulb temperature of the entering air in the tunnel were recorded by a data logger (Omega OM-62) having an uncertainty of ±2% RH and ±0.5°C. The data provided by the data logger were logged on to a computer through a USB connection and were processed by standard software provided with the data logger. The sample was mounted on a thermoelectric device (CP-031 Thermoelectric Cold Plate-TE Technology, Inc.), to keep its temperature below the dew point of the entering moist air. The temperature of the fin stock sample was measured at three points at the aluminum base plate, and the temperature of the entering moist air was recorded through thermologgers (Omega HH506RA), having an uncertainty of 0.05% of the reading +0.7 ^{0}C (where T is in ^{0}C). Type-J thermocouple wires were used to connect the sample to the thermologgers. The temperatures were measured at three different locations in the aluminum plate thermoelectric device junction, and then the value was taken to be the average temperature at that time instant. The locations of temperature measurement are shown in Figure 2.18. The Peltier fin stock assembly mounted on a frame was weighed using an electronic balance (Sartorius GP 8201, Accuracy: ± 0.1g), which logs the data onto the computer. The recording interval of the acquisition system was 0.18 sec. The air velocity was measured downstream of the sample, using thermal anemometer (Veloci-Calc 8355), providing accurate measurements up to 2.5% of the reading. The velocity was measured at seven different locations equally spaced from the top to the bottom of the heat exchanger assembly. The complete experimental apparatus for the table top wind tunnel is shown in Figure 2.19.

2.3.5 Operating Conditions and Procedure

The heat exchanger sample was first washed and completely dried before starting the experiment. The sample was then clamped on to the thermoelectric cooler. The close fit between the tunnel and the sample was checked to ensure that the electronic balance was free of any disturbances. The vertical alignment of the sample was checked using a spirit-level. To start the experiment, first the fan was switched on, and the DC voltage was adjusted until the desired air velocity at the exit of the fin column was attained. The humidifiers were then turned on, and the logging of the operating conditions (temperature and relative humidity) was started. When the desired humidity was obtained inside the tunnel, the thermo-electric cooling was switched on. At this point, the balance was zeroed, and the logging of the mass measurements was initiated. The real-time retained condensate was recorded, and the temperature of the cold plate was maintained using a variable power supply. Typically, the average sample base temperature was maintained at 14.5-16.0°C at steady state. The temperature of the fin base was measured every 10 minutes after the start of the experiment. The incoming moist air temperature was 21.0-23.0°C. Some of the steady-state conditions were varied and the effects were also observed. The experiments were conducted for two air velocities, 2.5-2.6 m/s and 3.5-3.6 m/s, and at relative humidity levels of 85-87% and 94-96%. Steady-state conditions were usually attained in around 1-1.5 hours of operation. For the visualization experiments, ink markings were used to identify the drainage paths. Also RAIN-X® Anti-Fog treatment was used on the front glass for clear visualization. Further, most of the experiments conducted were for the vertical orientation of the heat exchanger assembly, which was ensured through the spirit level. A few experiments were performed in which the sample was kept inclined to the vertical. To ensure that the air flow remains parallel to the fins, the tunnel was tilted with the heat exchanger assembly. The tilted assembly is shown in Figure 2.20.

2.4 Fin Stock Designs

Four different louver-fin designs were used in this study. The dimensions and geometrical parameters are specified in Table 2.2. In dynamic dip tests, only Design 1 and Design 2 were used. For the condensate retention and visualization experiments, all the four designs were used. For a given fin design, the same fin stock was repeatedly used for different surrounding aluminum plates with various channel geometries, for consistency. The first two designs (i.e. Designs 1 and 2) not only differ in external dimensions, but have different fin and louver spacing. Design 1 has higher fin and louver spacing compared to those of Design 2, and Design 2 is overall more compact than Design 1. Design 3 and Design 4 have almost the same dimensions except the fin depth. The fin depth for Design 3 was the smallest among the all designs tested. In terms of compactness, Design 3 and Design 4 have geometrical characteristics in between of Designs 1 and 2.

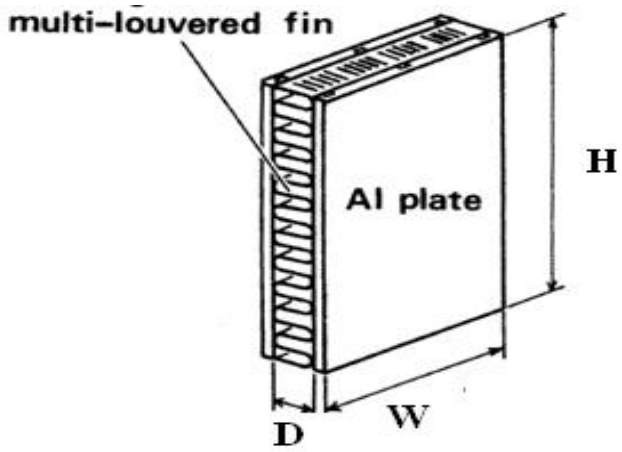


Figure 2.1 Heat exchanger sample used in dip tests [34]

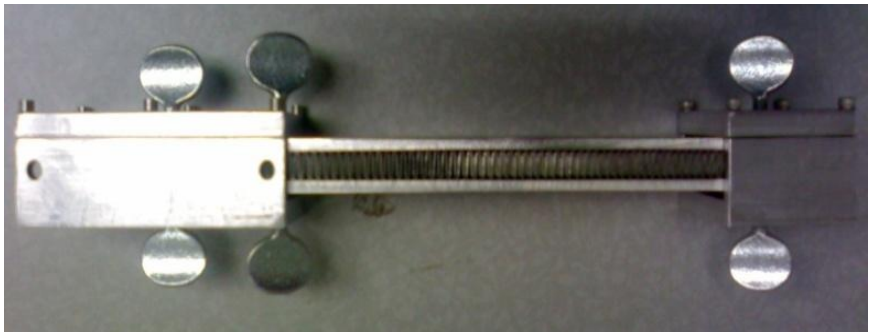


Figure 2.2 Clamp and screw assembly (used in dynamic dip tests)



Figure 2.3 Clamp and screw assembly (holes and countersinks)

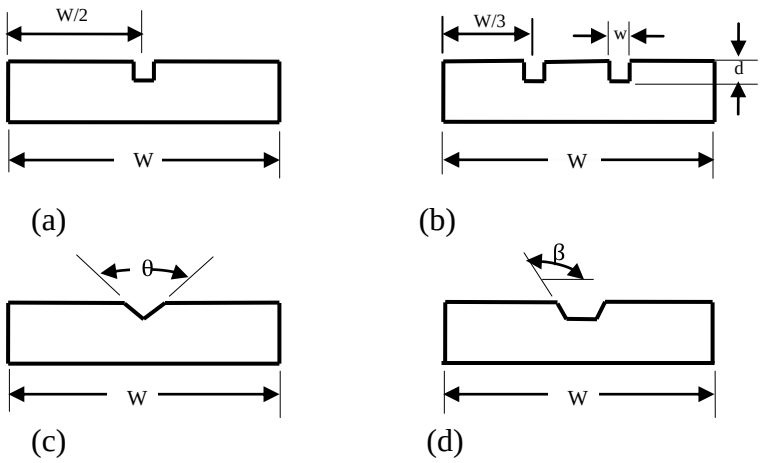


Figure 2.4 Channel dimensions & geometry (for dip tests): (a) rectangular channel at the center with w×d as width and depth, (b) positioning of two channels, (c) triangular channel with included angle, (d) trapezoidal channel with the angle specified, and width at the top as 1 mm and depth d

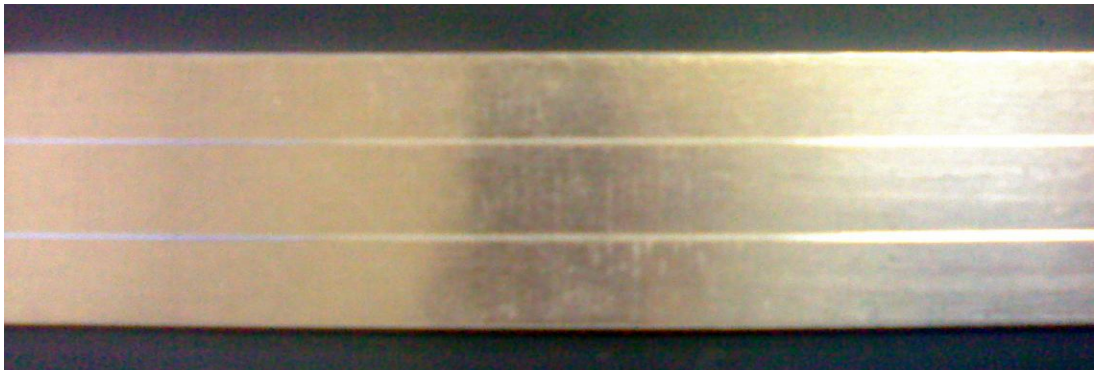


Figure 2.5 Drainage channels on aluminum plate covering the entire height

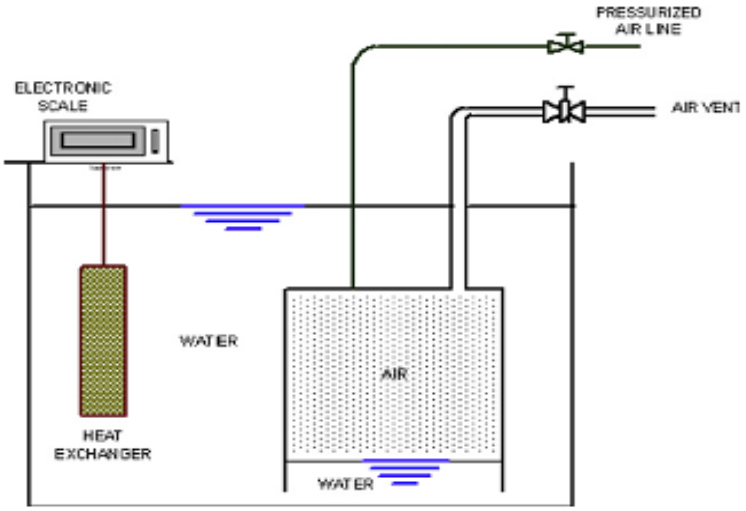


Figure 2.6 Schematic of dynamic dip testing apparatus [51], [52]

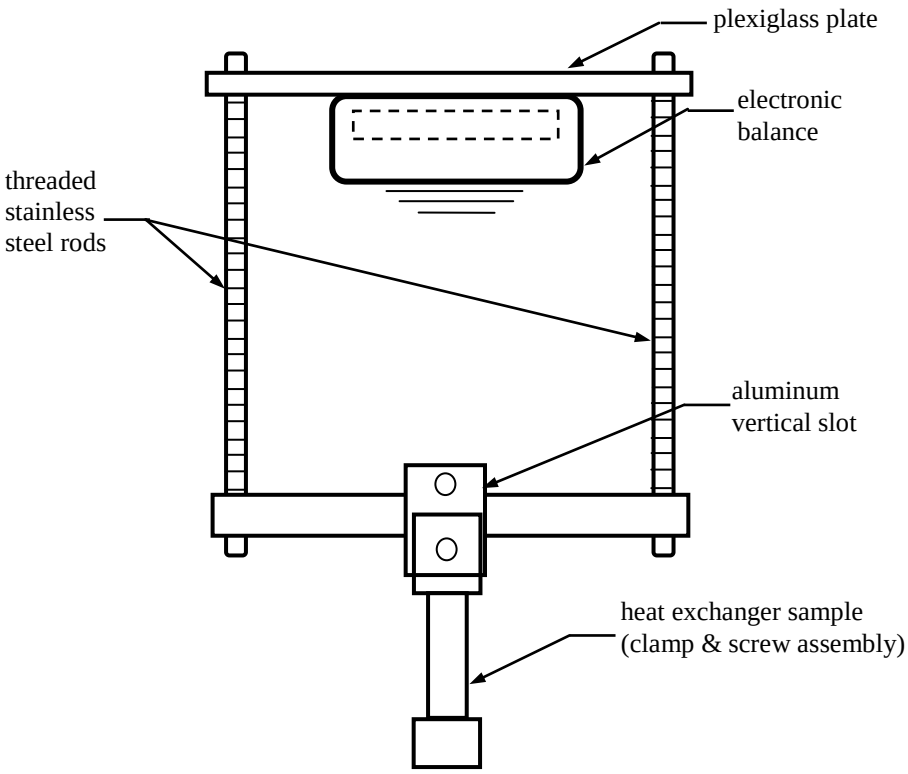


Figure 2.7 Metal frame used in dynamic dip testing

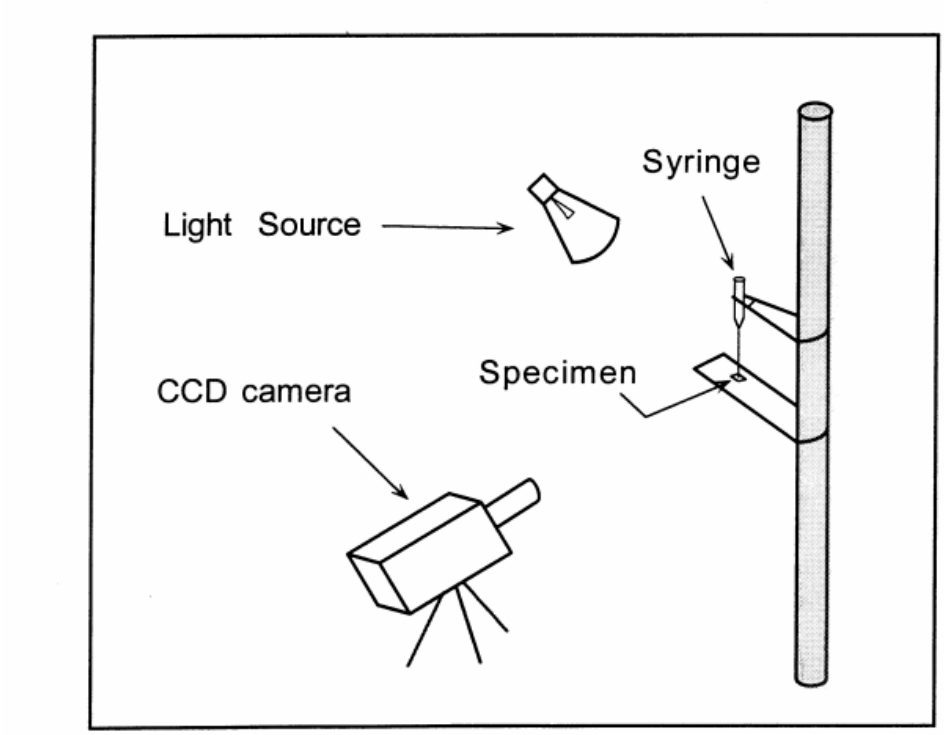


Figure 2.8 Contact angle measurement apparatus [38]

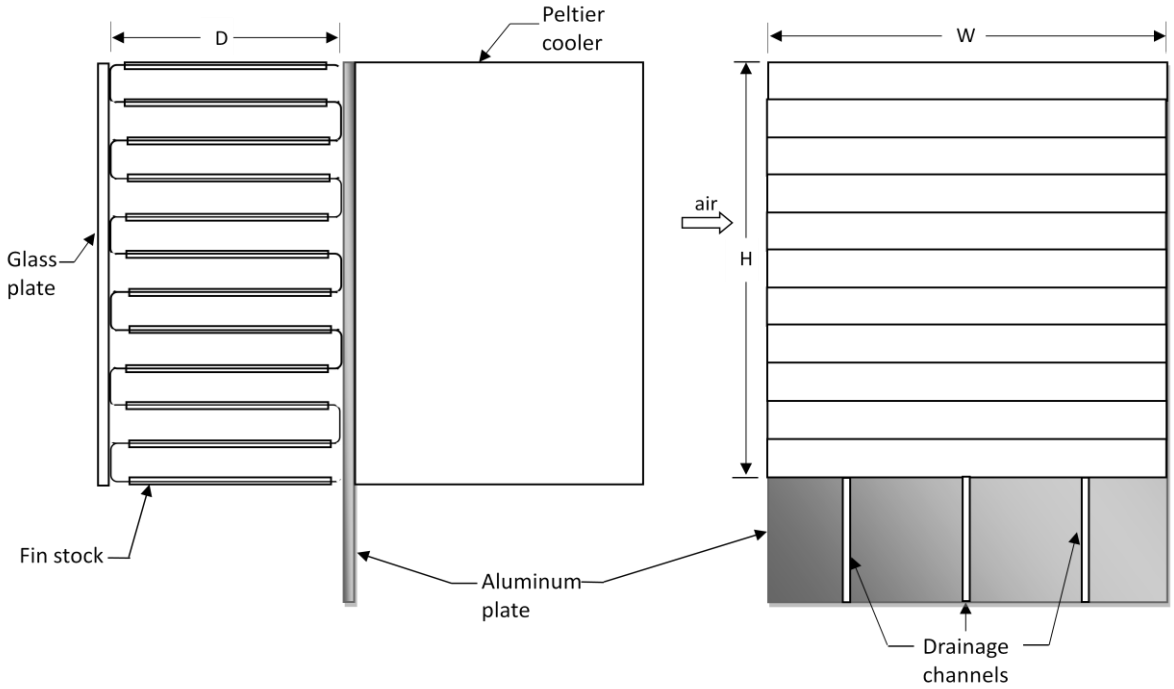
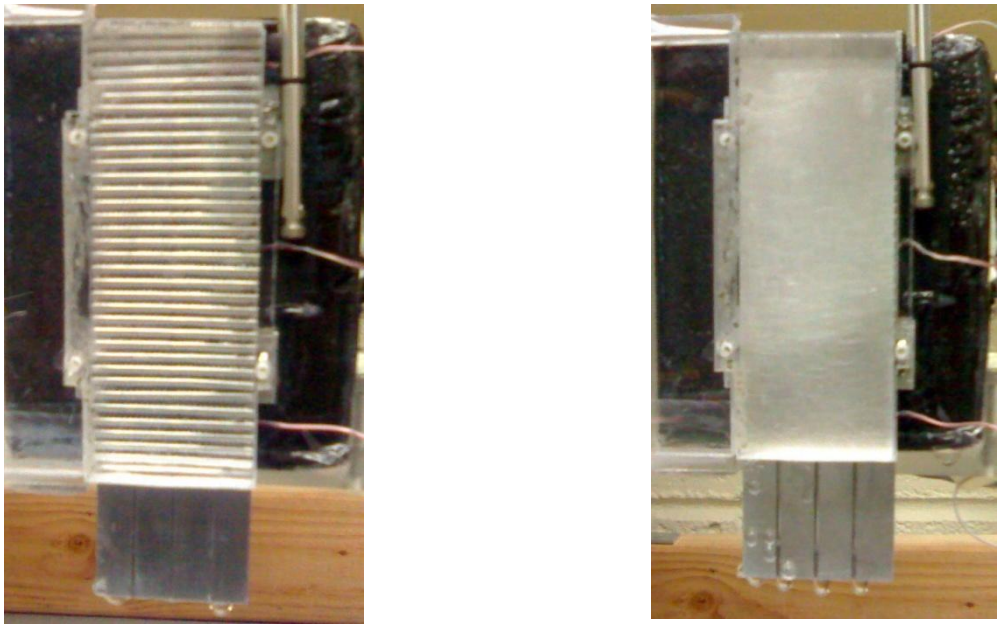


Figure 2.9 Heat exchanger assembly (single fin column) used in visualization experiments



a) b)

Figure 2.10 Heat exchanger sample a) visualization tests, b) quantitative measurements

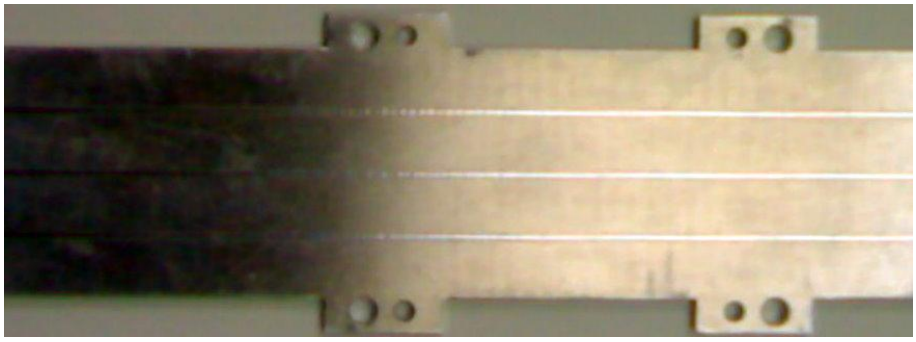


Figure 2.11 Drainage channels covering the entire length of the sample

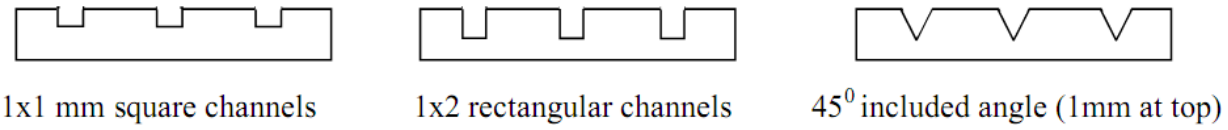


Figure 2.12 Some drainage channel designs used in condensation tests

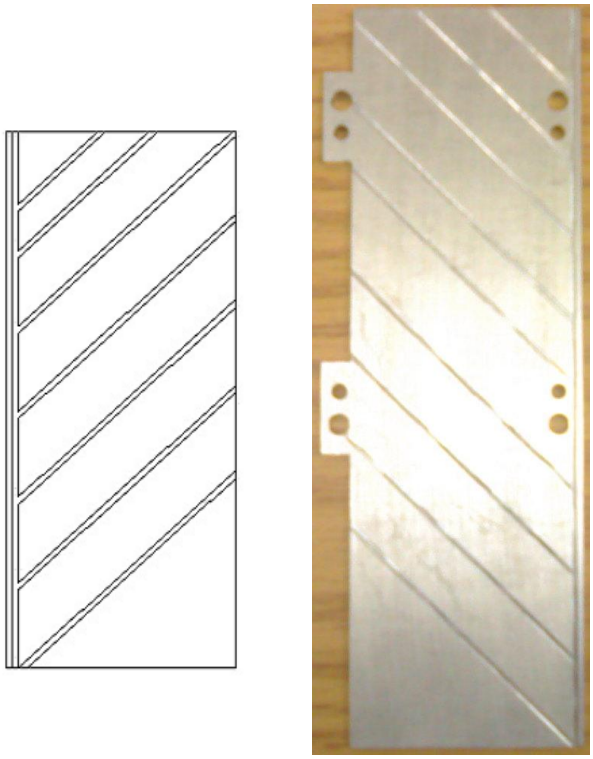


Figure 2.13 Drainage channels (square cross section-1x1 mm) inclined at an angle of 45^0

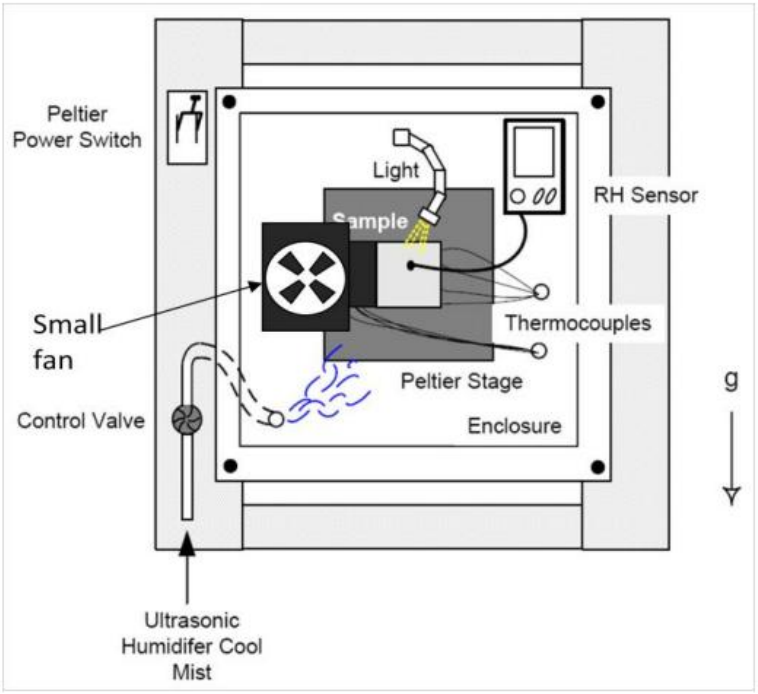


Figure 2.14 Schematic of a closed chamber for visualization

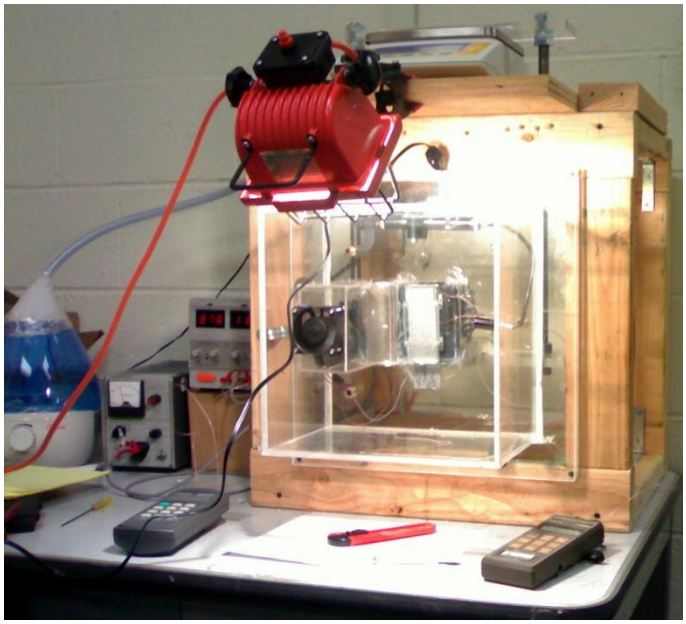


Figure 2.15 Closed visualization chamber: complete apparatus

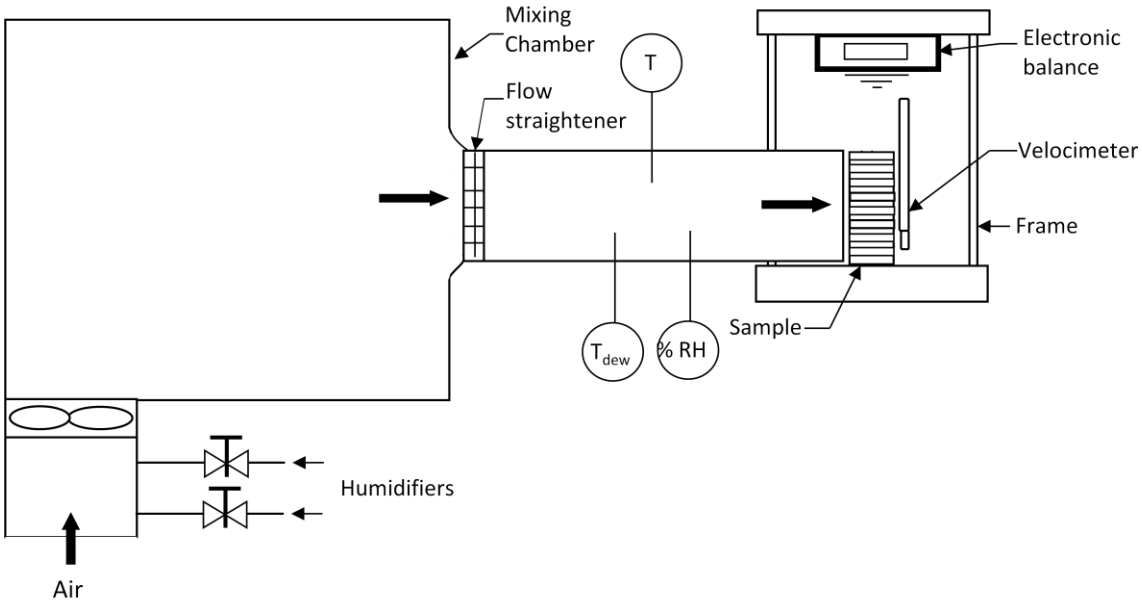


Figure 2.16 Schematic of the table-top wind tunnel

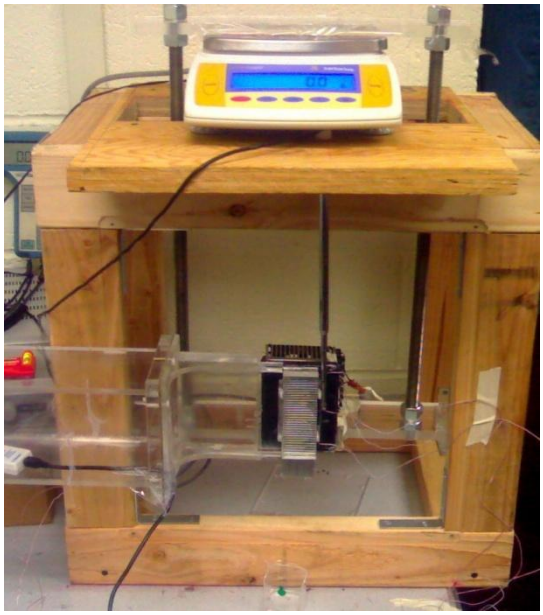


Figure 2.17 Close fit between the tunnel and the sample and the weighing mechanism

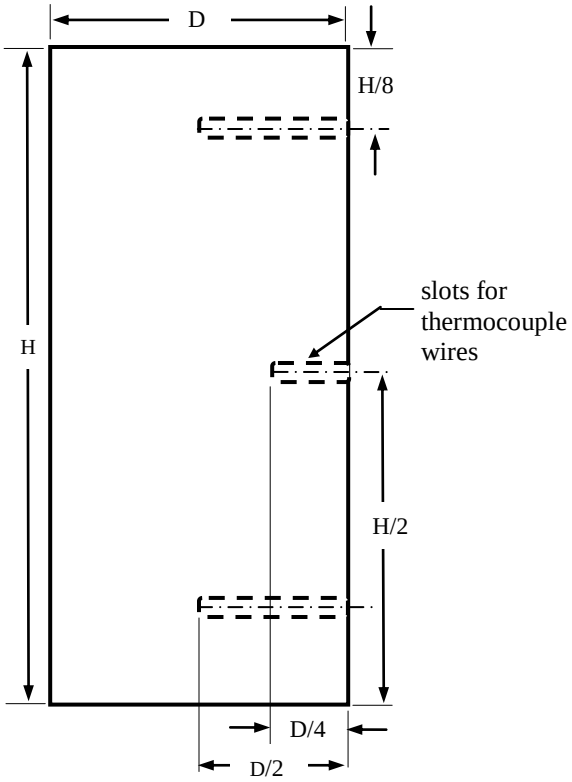


Figure 2.18 Temperature measurement locations in the heat exchanger base plate (length of the plate extending beyond the cold plate not shown)

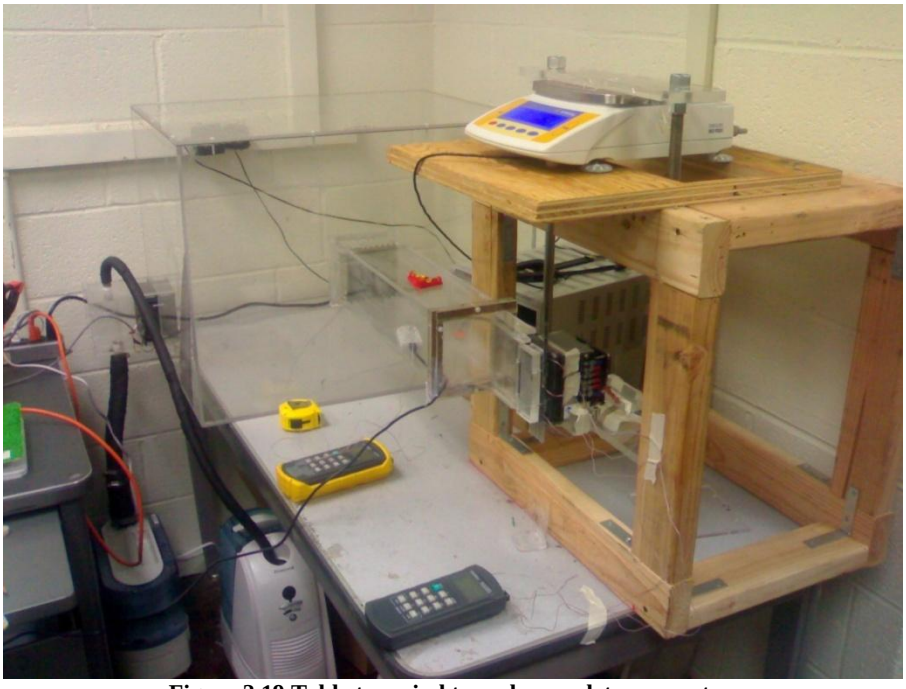


Figure 2.19 Table top wind tunnel: complete apparatus

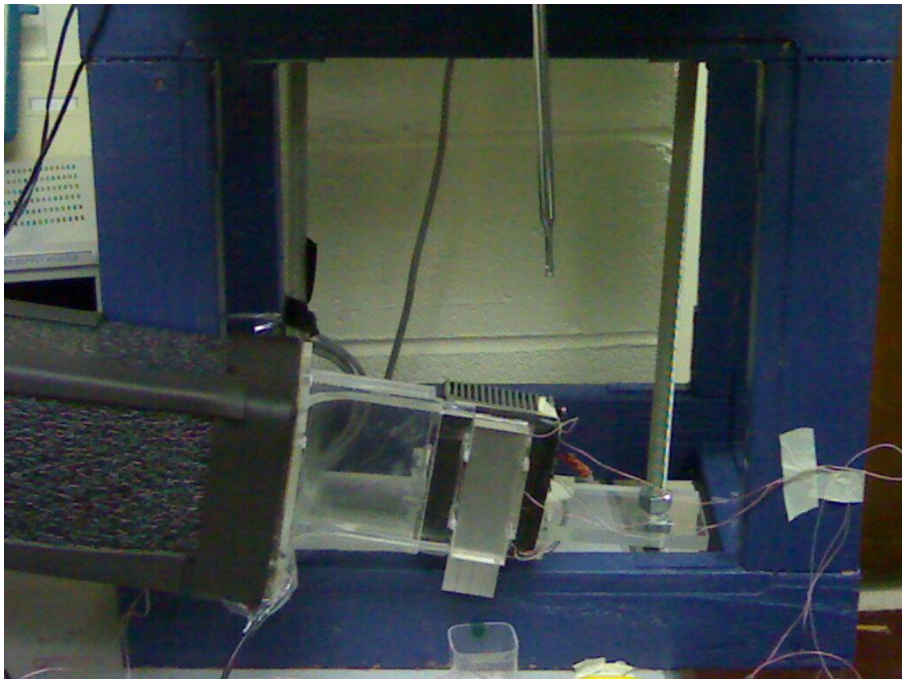


Figure 2.20 Inclined sample arrangement

Table 2.1 Channel geometries and dimensions used in the study

Channel Geometry	*Dimensions*	
	Dynamic Dip Tests	Condensation Experiments
Rectangular	1×1 mm[1] 1×2 mm 2×1 mm 2×2 mm	1×1 mm 1×2 mm 1×1 mm (non-vertical grooves)[4]
Triangular	90° 1 mm wide[2] 90° 1 mm deep[3] 45° 1 mm wide	90° 1 mm wide 22.5° 1 mm wide 45° 1 mm wide
Trapezoidal	1mm wide 120°[5]	1mm wide 120°

Table 2.2 Geometrical description of the fin stock designs[6]

	Design 1	Design 2	Design 3	Design 4
External Dimensions (H x D x W)	101.5[7] x 38 x 8.3	101.5[8] x 41.5 x 6.8	101.5 x 16 x 8.1	101.5 x 45 x 8.1
Louver Spacing L_P	1.38	0.88	1.4	1.4
Louver angle (^{0}) α	44	35	27	27
Louver Width L_W	6.7	5.2	6.4	6.4
Fin Width F_W	8.3	6.8	8.1	8.1
Fin Thickness δ	0.24	0.16	0.1	0.1
Fin Spacing F_P	1.53	1.1	1.20	1.25
Non-Louver length L_{NL}	1.6	1.6	1.7	1.7

[1] Expressed as wxd (Refer Figure 2.4 a)
[2] Specified are the included angle and the width at the contact with the fin stock (Refer Figure 2.4c)
[3] Depth of the channel and the included angle is fixed
[4] Channels inclined to 45^0 to the vertical (Refer Figure 2.13)
[5] Specified are the width at the contact with the fin stock and the angle β (Refer Figure 2.4d)
[6] All dimensions are in mm, unless specified
[7] The fin height was 195 mm for the dynamic dip tests
[8] The fin height was 200 mm for the dynamic dip tests

Chapter 3 - EXPERIMENTAL RESULTS AND DISCUSSION

The results and discussion presented in this chapter summarize all the important findings related to condensate drainage behavior. In the first section of this chapter, the results obtained from the dynamic dip tests are presented. Results from the contact angle measurements, and the need for the visualization and actual condensation tests are also presented. The final section discusses about the real time condensate retention results and their comparison to the dynamic drainage test results.

3.1 Dynamic Dip Testing Results

The dynamic dip tests provided the initial results for the drainage and retention characteristics of louver-fin heat exchanger samples, and the effect of drainage channels. The experiments were performed on a single row of fins assembled, as discussed previously.

3.1.1 Fin Design Comparison

Two different fin stock designs were tested for water retention/drainage behavior through the dynamic dip tests. Design 1 and Design 2, described earlier. The experiments were first conducted for the baseline case, i.e., without any drainage channels on the surrounding aluminum plates.

The water retention/drainage behavior of the two fin stock designs without any channels is provided in Figure 3.1. The results are presented in terms of water mass per unit air side heat transfer area (M_A) with time. The method/procedure for the calculation of the total air side area has been shown in Appendix-A. Design 1 has a much higher retention per unit area (almost 100% more) than Design 2. Although Design 2 looks more compact with smaller fin and louver spacing than Design 1 (see Table 2.2), the retention is much lower.

However, the non-louvered length, which also plays a critical role in determining the condensate retention [34], is same for both the designs. Also, only nominal fin spacing cannot be taken as the sole parameter for determining the compactness of the fin. It is interesting to note that the fin gap (distance between the fins) is different from the nominal fin spacing. As can be seen from Figure 3.2, which shows the cross section of a multi louvered fin, the fin gap can be given as,

$$F_{p,eff} = F_p - L_p sin\alpha \tag{3.1}$$

The fin gap for Design 1 is 0.57 mm, owing to its higher louver spacing and louver angle, while for Design 2, it is 0.56 mm. Thus despite having quite different fin spacing, the fin gap— important to inter-fin condensate/water bridge formation— is similar for both the designs.

Also clear from the results is the difference in the retention patterns in the two designs. Design 1 show a steady retention pattern (asymptotic retention is attained after a short time ~15-20 s), while Design 2 shows a continuous-drainage pattern [51]. Visual inspection of Design 1 after the dip test revealed that water accumulates between the fin surfaces causing fin "bridging". The water is retained there, as the gravity is not able to overcome the surface tension force, which caused the bridging, thus giving a steady and a higher retention. On the other hand, in Design 2, there was no bulk accumulation of water at any specific location; the final retained water was in the form of droplets on the fin stock surface. The difference in the drainage characteristics can also be explained from the difference in the fin shapes, i.e., the fin folding pattern (shown later in visualization test results). The difference is due to the slight triangular fin shape of Design 2, which may have eliminated fin bridging by sustaining a continuous drainage path.

3.1.2 Effect of Drainage Channels

Plates with drainage channels were then used for the two fin designs. The channel parameters were varied and the results are compared. The results obtained from the dynamic dip testing of the samples with drainage channels are presented here. First, the effect of changing the channel aspect ratio and geometry keeping a single dimension fixed (usually the channel width in contact with the fin stock) is presented. Then, the effect of changing channel dimension for the same fin geometry, and finally the effect of number of channels with the same geometry and specifications is presented.

3.1.2.1 Effect of Channel Geometry

The results for channels made as vertical grooves having different geometries/shapes but fixed width (usually =1 mm) in contact with the fin are shown in Figure 3.3 and Figure 3.4. The shapes considered are square, triangular (with θ=45° as the included angle, see Figure 2.4 (c)), and trapezoidal (β=120°, see Figure 2.4 (d)). It is clear from Figure 3.3 that the drainage channels significantly reduce condensate retention for Design 1. The triangular channels are most effective, followed by the square channels and the trapezoidal ones. An effective drainage channel should have a combination of strong capillary forces, and an optimum cross-sectional area (including effects of parameters like depth and width) to persistently maintain drainage through them. An important parameter which might give insight into the effects of surface tension and cross sectional area is the hydraulic diameter (D_H). The triangular channel which has the minimum hydraulic diameter provides the most reduction in retention, while the trapezoid which has the highest hydraulic diameter, provides the least reduction. Thus, an effective channel which provides stronger surface tension forces and the increased capillary attraction can suppress the formation of bulk accumulation, such as the inter-fin bridges observed in the retention pattern

of Design 1 earlier, without any channels. For Design 2, no improvement in the water drainage is evident from the results shown in Figure 3.4. The final retention mass is almost the same in all cases, with or without channels. The reasons for non-performance of the drainage channels with Design 2 are explored in later sections.

3.1.2.2 Effect of Changing Channel Dimensions

For the same channel geometry/shape, the effect of changing the dimensions (for example, the aspect ratio for rectangular channels, included angle for the triangular channels and so on) was studied. Figure 3.5, 3.6 and 3.7 show a comparison between channels with similar shapes but different dimensions. The results are shown for rectangular geometries, with varying depth and width of channel for Design 1, in Figure 3.5. The results clearly show that the best performance (among the channel geometries tested) is achieved by the square channel, having 1×1 mm as the dimensions, again the one with the least area and hydraulic diameter. A surprising result is that when the channel depth is increased to 2 mm (width fixed at 1 mm) more condensate is retained than with the 1mm deep channel. If the width is increased, while depth remains 1 mm, the results further deteriorate, and retention increases. Since the 2×1 mm and the 1×2 mm channels have the same aspect ratio and hence equal hydraulic diameters, it can be concluded from the results that condensate drainage is not a function of hydraulic diameter alone. The results presented are in contrast with those reported by McLaughlin and Webb [36], who observed that shallow channels (1 mm) are ineffective while deep channels (2 mm) are capable for some drainage. Increasing the width and the depth any further makes the channel ineffective, as can be seen from the condensate retained by 2×2 mm channel, which is almost equal to the baseline case.

A comparison between different aspect ratios of triangular channel geometry for fin stock Design 1is shown in Figure 3.6. As clear from Figure 3.3, the triangular geometries are the most

effective among all the geometries tested in promoting drainage for fin Design 1, with the width remaining fixed at 1 mm. Out of these triangular geometries, the channels having 45^0 included angle provided the sharpest edges and the maximum area for the flow, thus providing the largest reduction in the water retention (~39%). The channel with the 1 mm depth and 90^0 included angle hence having more width at the top possibly underperforms because of lack of sharp edged corners, as compared to the previous channel. Another case is the channel with 1 mm width at the contact and 90^0 included angle, which is less effective than the other two channels in consideration, as the area available for the water to flow in the channel becomes very small.

The results for Design 2, with channels of rectangular geometry and varying dimensions are shown in Figure 3.7. Similar to results shown in Figure 3.4, there are no improvements in the water drainage of Design 2. Even after modifying the dimensions of the channels, they did not cause any improvements in the drainage behavior of Fin Design 2. The experiments were also performed for different dimensions for the triangular geometry, but the result was the same. So, it is clear from the dynamic dip tests that drainage channels are ineffective for Design 2.

3.1.2.3 Effect of Number of Channels

Finally, the effect of increasing the number of channels on the plates was studied. The number of channels was increased from one to two, equi-spaced across the depth of the fin. The results for Design 1, with the triangular channel with 45^0 included angle, and the square channel, are shown in Figure 3.8 and Figure 3.9, respectively. The location of the two channels is shown in Figure 2.4 (b). The increase in number of channels from 1 to 2 makes a slight improvement for the triangular channel, while there is an insignificant difference for square channels, except for a slight change in the drainage pattern. On the other hand, increasing the number of channels did

not also change the retention behavior of fin stock Design 2. The final steady state retention still remained the same.

Further, the dynamic dip testing results obtained were tested for statistical significance, and the upper and lower bounds were obtained for 95% confidence interval. The bounds also included the uncertainty caused by the errors in the instruments (e.g., the electronic balance). The results obtained (see Appendix-B) show that the bounds for 95% confidence, were much less than the difference in the results produced by the channels. The overall uncertainty in the readings lies in the range 1.5-4%. Finally, the static retention data and the percentage reduction in the steady state retention for all the channels for design 1 are presented in Table 3.1.

3.1.3 Reliability of Dynamic Dip Tests: Contact Angle Variation

Though the dynamic dip testing has been verified and used frequently as a standard method to assess the retention/drainage behavior of heat exchangers by previous researchers including [36], [51], [52], the reliability of the test has not been proved for testing physically small sample sizes like those used in the current experiments. Also the drainage behavior under the influence of drainage channels has not been previously tested using the dynamic dip tests.

Further, it was observed during the experiments, that the retention behavior slightly changed after initial few cycles of experimentation; however, it remained the same thereafter. As was mentioned in Chapter 2, same fin stock was used for all the experiments to maintain consistency in the results. The fin stock sample was first washed using acetone, and then rinsed several times with water before putting it to actual experiments. Thus, to analyze the effect of surface wettability changes on the dynamic dip testing results, contact angle measurements were done to assess the effect of contact angle change on the dynamic dip test results.

The contact angles were measured at three different times; at first, on the unwashed fin stock, then after few cycles of experimentation, and finally just after washing with acetone solution. The representative images obtained for the two extreme cases are shown in Figure 3.10. The mean value of static contact angle measured initially was found to be 79^0, which changed to 75^0 after few cycles of experiments, which further changed to 65^0 after acetone treatment. The change in the static contact angle was not found to be much. The uncertainty analysis for the contact angle measurements has also been done to determine the 95% confidence intervals, and has been reported in the Appendix B- Uncertainty Analysis. The overall uncertainty in the measurement of static contact angle is 2-6%.

The results for the untreated/unwashed sample and the sample just washed with acetone are shown in Figure 3.11. The dynamic dip test results manifested a large change in drainage behavior with this small change in the contact angle.. The results are presented for the baseline case, the case with the square channels (1 x 1 mm), and ones having the rectangular channels (1 x 2 mm). The slight change in surface wettability though did not change the final steady state retention much, but significantly affects the drainage behavior. However, an important point to notice was the relative behavior of channels in reducing the retention in the reduction. The change in the surface wettability changes the drainage pattern/behavior; however the relative performance of the channels remained the same. The square-channeled exchanger remained better than the rectangular channeled one, which was again better than the baseline case. So, the dynamic dip tests are reliable with respect to the performance of different drainage channels.

3.2 Closed Visualization Chamber

To confirm the findings of the dynamic dip tests, and to analyze the behavior of condensate, in particular to identify the physical mechanisms relevant to retention and drainage, the

visualization tests were necessary. Thus, the idea of closed visualization chamber was first attempted because it had been previously used in the visualization of similar smaller samples [42]. The slightly modified set-up could not be used for visualization. The major difficulty was the visual obstruction posed by the chamber. It was not possible to see from outside the chamber the condensate behavior on the fin stock. Moisture was by an ultrasonic humidifier, which produced tiny, cool droplets. If the droplets did not evaporate they may affect the results. The fan power that could be used was very low as higher fan speed caused turbulence inside the chamber, making it difficult to maintain steady-state conditions. Due to the small size of the chamber, there were difficulties associated with keeping different instruments inside it (e.g.,velocimeter). Further, condensate formed on the front side of the glass plate, further complicating visualization. This closed chamber was abandoned.

3.3 Table-Top Wind Tunnel Results

The small wind tunnel apparatus, as described in detail in Chapter 2, allows for both the real time mass measurements as well as the visualization tests. As is clear from the literature review (Chapter-1), condensate retention has been shown to have a large affect on the heat transfer. Thus, the actual amount of condensate on the surface at a given time has an impact on the heat transfer. There might be oscillations in the condensate retention, which also might affect the thermal performance data. Further, the time required to achieve the steady-state conditions differs depending on various conditions and has a significant effect on the heat transfer characteristics. Real-time quantitative measurements are necessary to investigate the condensate loading characteristics, which have an impact on the heat transfer performance analysis. The quantitative results were obtained for the heat exchanger samples on the baseline case (i.e., without any channels), and with some of the best-performing channels in the dynamic dip tests.

Some new channel designs were also tried. Also, experiments were conducted over a large parameter space, including changes in the incoming air velocity, the inlet relative humidity and the temperature of the heat exchanger sample. The results presented in this section are arranged in the order of comparison of fin design, the effect of different drainage channels, the effect of changing the inlet relative humidity, and finally the effect of changing the air velocity on the condensate retention behavior.

3.3.1 Fin Design Comparison

The real time condensate retention experiments were performed on all the four fin designs mentioned in Table 2.2.The mass of condensate retained per unit area (M_A, please refer Appendix-A for detailed calculations) as a function of time is shown in Figure 3.12. Three or four readings were obtained for a single fin design (to ensure consistency in results), and one of them is plotted here. The retention data were recorded over a 90-minute interval. The conditions maintained (at steady state) for the shown results were:

- Inlet relative humidity of moist air = 85-87%
- Temperature of moist air= 22.5-24.5 ^{0} C
- Temperature of fin base= 15.0-16.5 ^{0} C
- Air velocity at the exit of fin column= 2.5-2.6 m/s[9]

The variation in the air temperature for a single reading was less than 1^0 C. The differences occur between different readings, because of the variation in the environmental conditions. For example, if the relative humidity of the environment is low on a particular day, and as the wind tunnel is open to the environmental air, to maintain the same relative humidity inside the tunnel,

[9] The air velocity was measured at the start of the experiment, and it varied with time due to the condensate retention and draining. The air speed was measured at the exit of the fin column.

more water is required to be injected into the flow. This was done through adjustment of valves with the humidifiers. Thus temperature of the moist air is higher for that set of conditions.

For all the graphs in the figure, there is an initial period of delay, when there is no formation of condensate on the surface. This is because of the time which the thermoelectric device takes to reach a temperature below the dew point of the moist air. As was reported earlier (Chapter-2), the relative humidity was first maintained for the given air flow rate, and then the thermoelectric cooling was initiated. The accumulation of condensate on a surface takes place by the processes of condensation and coalescence. The condensate is retained there by the surface tension forces. The water droplets are held until they are shed when the flow or the gravitational forces overcome the surface tension force, or the droplet is swept by another moving droplet. The movement of the water droplets can also be enhanced by drainage channels, as described in detail in the next section. The rate of deposition of condensate can be seen as the slope of the graphs for the initial period when the steady state is not attained (as there was no drainage observed in this period). The slopes depend on the operating conditions and also on the geometrical parameters of the fin surface, hence different for different fin designs. The slope of the graph can also be calculated as (if the quantities are known),

$$\dot{m}_c = \dot{m}_{da}(\omega_{in} - \omega_{out}) \tag{3.2}$$

The quantity of condensate retained increased asymptotically to a steady state value. The time required to attain steady-state conditions differed for different fin designs. At steady state, the rate of condensate formation becomes equal to the drainage rate, since the quantity of water removed from the airstream must also leave the heat exchanger at steady state.

$$\dot{m}_c = \dot{m}_d \tag{3.3}$$

Fin Design 1 and Design 2 were previously tested through the dynamic dip testing and Designs 3 and 4 were recently obtained. As can be seen from the figure, Design 1 has the highest retention per unit area, followed by Design 3 and 4, and then by fin Design 2. The results support the findings of the dynamic dip tests (see Figure 3.1), which showed that Design 1 has almost 100% more retention than Design 2. Design 3 and Design 4 have a steady state retained M_A close to Design 1. Design 4, which is similar in dimensions to Design 1, behaves very similar to Design 1, and almost has the same nature of retention curve. Design 3, which has the smallest depth (D in Table 2.2) for air flow, reaches the steady state quickest of all. The attainment of the steady state, however, in this case is not the steady value like other designs, but the steady state value of retention oscillates between the maximum and the minimum. Since the fin design has the smallest depth, the air shear forces easily push the condensate back to the end of the fin, even before it starts to drain under gravity, along the tube wall. The retained mass then goes to the maximum, until the draining along the wall starts occurring, which decreases the maximum value attained. This cycle continues, and hence oscillations are seen in the retention curve of Design 3. This observation is in accordance with the findings of Korte and Jacobi [11], who found two possible cases for condensate retention: a) The condensate accumulates until rate of deposition becomes equal to the rate of shedding, giving a steady state value at the end, or b) Cyclic condensate retention and oscillates between the maximum and the minimum value due to shedding characteristics.

The difference in the retention behavior for Design 1 and Design 2 is explored in more detail in the Visualization results section. Designs 3 and Designs 4 have similar fin gap as other designs and shape similar to Design 1. The fin gap for Design 3 is found to be 0.56 mm, while for Design

4 it is 0.61 mm. Thus, despite of having quite different fin and louver spacing, the designs have similar fin gap.

3.3.2 Effect of Drainage Channels

All the four fin designs were then experimented with the drainage channels on the side aluminum plates. The drainage channels selected for the purpose were the ones which performed well in the dynamic dip tests. Some new drainage channel designs/shapes were also experimented. Most of the channel designs were tested on Fin Design 1. The channels studied in these set of experiments are shown in Table 2.1.

The results are first shown for fin Design 1. For these experiments on a given fin design, with different channels, all the steady-state conditions remain the same as specified in section 3.3.1, except for the air velocity, which was kept at 3.5-3.6 m/s for these tests[10]. The retention behavior of Design 1 with different channel geometries is shown in Figure 3.13. The results are shown for the square, triangular and the trapezoidal geometry. It is clear from the figure that the channels have the potential to reduce the condensate retention of the heat exchangers. For all the channels, the initial slope of the graph which indicates the rate of condensation deposition is almost the same as the baseline case. This is the period during which no drainage was observed. This is because the rate of condensate formation depends only on the operating conditions and the geometrical parameters of the fin designs. The geometry remaining the same in these cases (same fin stock being used for all tests), the only cause of the slight difference might be small differences in the operating conditions. For these plots, three or four readings were taken, but only one of them is shown, so as to present the true real time behavior. Some of the operating conditions, like the inlet air temperature depending on the atmospheric temperature and the

[10] Again, this was the air velocity at the start of the experiment.

humidity, as explained earlier, were not under direct control, and that is probably why slight differences are evident.

After this condensate deposition phase when the channeled samples show the same behavior as the non-channeled one, the channels aid in improving the drainage characteristics, and hence the retention curves start to differ. One prominent difference between the retention characteristics of the baseline case and the behavior with channels is the asymptotic attainment of the steady state value in the baseline case, while the channeled samples seem to exhibit the oscillation mode (as discussed previously). There may be various drainage modes available for the condensate to drain. Some of these drainage modes, like the pure gravity driven ones, have the maximum rate constrained by the geometrical and other similar parameters. So, without channels, when this maximum rate is attained, which is usually equal to the deposition rate, the steady state conditions start prevailing. When channels are present, they provide a new drainage mode which drains the water effectively. As will be clear from the discussion in the Visualization results, this drainage provided by the channels is not continuous, but occurs in steps. These channels remove a considerable amount of water at a time, effectively resetting the heat exchanger surface to a partially loaded condition. The surface would then again start loading with deposition rate going higher than the drainage rate, thus causing the oscillations. However, in this process, the channels end up keeping the steady state value (average between the maximum and minimum values of the oscillations) lower than the baseline case.

Similar to the results obtained in the dynamic dip tests, the triangular geometry of the drainage channels performs the best, closely followed by the square one, and then the trapezoidal case. It seems like the presence of sharp corners (i.e., cause of strong capillary forces) and sufficient area to allow flow make the triangular channels perform the best. The reduction in steady state

retention[11] for the triangular, square and the trapezoidal channel geometry is found to be 23.2 %, 19.3 % and 16.1 % respectively, compared to the baseline case. The results here match closely with the dynamic dip test results (Figure 3.3), hence verify the reliability of the dip tests for the present set of experiments.

Further, for the same geometry, the dimensions of the channels were varied. The condensate retention/drainage behavior of Fin Design 1 with rectangular channels having different dimensions and orientation is shown in Figure 3.14. An important addition is the square channel with non-vertical orientation, as shown in Figure 2.13. The square channels are not vertical, but are inclined at 45^0 to the vertical. The channels drain into a secondary vertical channel which is located outside of the fin stock area, and finally drains the condensate to the exit. These channels were designed so as to combine the effects of air drag and gravity forces on the fluid flow in the channels.

As the figure shows, the square channels, having the vertical orientation, provide the maximum possible reduction among the rectangular geometry channels tested. It is surprising to note that increasing the depth of the channels to 2 mm does not promote drainage. The channels slightly change the retention/drainage behavior, as is clear from the figure. However, the difference between the performance of square (1x1 mm) and that of rectangular (1x2 mm) channels was very small in actual condensation tests, as compared to the dynamic dip tests. The square channels with the non-vertical orientation, did not perform as well as the vertical channels. The figure shows that the channels performed similar to the rectangular vertical channels (1x2 mm), and failed to promote drainage. From the visualization of the test section, it was seen that there were more instances of spilling the condensate at the fin-wall intersection, as compared to the

[11] Calculated as average of the readings for last 10 minutes of the test

vertical orientation. This might be mainly because of reduction in the effective gravity force. It was also observed by Mclaughlin and Webb [36] that the channels spill the condensate onto the fin wall intersection, if they are overfilled (See Figure 3.15). To verify the present findings, the experiments were also performed keeping the sample inclined to the vertical. The results are shown in the next section.

Figure 3.16 shows the effect of varying the dimensions of the triangular channel geometry. The operating conditions were same as described previously (air velocity=3.5-3.6m/s, RH=85-87%). The changes made were in the included angle, which was kept at three values- 22.5^0, 45^0 and 90^0. The width at the top (i.e. in contact with the fin) remained fixed at 1 mm. The depth thus changed, depending upon the included angle. The one having the smallest angle is the deepest while the one with the largest angle is most shallow. As is clear from the figure, the reduction in the steady-state condensate retention caused by the 90^0 included angle channels is the least (13.3 %), while the reduction caused by the 45^0 included angle channels was the most (23.2 %). The reason for the smaller effectiveness of the 90^0 channels could be the smallest area of flow provided by the channels. However, increasing the depth of the channel by making the included angle 22.5^0 instead of 45^0 does not enhance the performance much (16 % reduction with deeper channels). This observation is quite similar to the case of the rectangular channels, where making the channels deeper beyond a certain depth was not of much help. Thus, depth of the channels with included angle as 45^0 show the best performance among the dimensions studied, with respect to the reduction in the steady-state retention. Also, the 45^0 and the 22.5^0 channels start draining earlier than the 90^0 channels. This is clear from the condensate retention curve. This might also be a reason for differences in the retention slope being exhibited early than other geometries, and is explained in more detail in Visualization results. The deepest channels show a

continuous drainage characteristic curve, which implies that once the condensate is inside the channels, it flows without any interruption. This is different from the shallow channels, where overfilling might cause spilling and the drainage is not continuous.

For fin Design 2, the effect of drainage channels on the condensate retention and drainage characteristics was also tested. Figure 3.17 shows the effect of drainage channels on the condensate retention behavior of fin Design 2. The operating conditions are same as those specified in Section 3.3.1. Only results for square channels have been shown for the sake of clarity. As in the dynamic dip test results, the real time condensate retention results show that the channels are ineffective for fin Design 2. The reason for this cannot be attributed solely to differences in the geometrical parameters. The difference from other fin stocks could be the difference in the fin shape. This aspect has been closely examined through the visualization tests, and has been reported in the later sections.

The results for the condensation tests on Fin Design 3 are shown in Figure 3.18. The operating conditions maintained were same as previously specified, except the air velocity, which was kept at 3.5-3.6 m/s (at the start of the experiment). As was found in Figure 3.12, the fin design attained steady-state mass retention the fastest among all the designs tested. This was because of its small depth, which was less than half of other fin designs. (Table 2.2) Further, the drainage characteristics were slightly different from other designs, with it exhibiting the oscillation mode. The number of channels used across the depth of this design was only one and not three as was in other designs. Square channels and triangular channels (included angle = 45^0, width at the top = 1 mm) were experimented for this design. Furthermore, the effect of variation of number of channels was studied. Two square channels equally spaced across the fin depth were used. The reduction in the average steady state retention was 17%, 13 % and 25% using the single square

channel, the triangular channel and the two square channels, respectively. The reduction provided by the two square channels is the highest provided by all the channels tested on all the designs.

A difference between how the channels affect the characteristics of this fin design and the other designs can be seen clearly by comparing this figure with the retention characteristics of Fin Design 1 (Figure 3.13). As was previously discussed, the channeled and the non-channeled samples have the same retention behavior in the initial phase of the experiment, when no drainage takes place. In this design, owing to its small depth, the drainage starts even before the fin stock is completely wetted with condensate. Thus, here the channeled samples start behaving differently from the baseline case pretty early as compared to the other fin designs. Also, the steady-state is characterized by the oscillation mode, with the amplitude of oscillation (the difference between the maximum and the minimum retention) being highest for this fin stock design. The sample with the two square channels shows a large difference in the maximum and the minimum retention (characterizing the steady state), indicating the high effectiveness of the drainage channels.

The effect of drainage channels on the condensate retention characteristics of fin Design 4 is shown in Figure 3.19. As was provided in Table 2.2, the dimensions of fin Design 4 are similar to fin Design 3, except the fin depth, which is much larger for Design 4. The retention per unit area (M_A) without drainage channels for this fin design was almost same as Design 1, as was seen in Figure 3.1. The figure here shows the effect of square (1 x 1 mm) drainage channels. The channels reduce the steady-state retention by 19.6 %, which is close to the reduction provided by the square channels for fin Design 1 (19.32 %). The channeled sample behaves similar to the non-channeled one for the initial 50 minutes of the tests. This is the time when little or almost no

drainage occurs. The channels then start to enhance the drainage rate. Just like the fin Design 3, it attains the cyclic (oscillating) steady state.

Further, the real time condensation results obtained were tested for statistical significance, and the upper and lower bounds were obtained for 95% confidence interval. The bounds also included the uncertainty caused by the errors in the instruments (e.g., the humidity sensor, velocimeter, etc.). The uncertainty in each reading depends upon the uncertainty in the measurement of air velocity, the inlet humidity, and the fin base temperature. The uncertainty for each reading has been calculated and reported separately (Appendix-B). The average overall uncertainty in the readings lies in the range 1.5-4%. Finally, the static retention data and the percentage reduction in the steady state retention for all channels for fin designs 3 and 4 and Fin Designs 1 and 2 are presented in Table 3.1and Table 3.3, respectively.

3.3.3 Effect of Sample Inclination

To analyze in more detail the effectiveness of the inclined channels (described previously), and to assess the performance of drainage channels under non-vertical orientation of the heat exchanger sample, the sample was inclined to 15^0 to the vertical. The inclination was kept towards the leeward side. In these experiments, the humid air flow was maintained to be perpendicular and uniform into the fin front. Fin Design 1 was tested for the baseline and the square channeled (1 x 1 mm) case, with this non-vertical orientation. The results are presented in Figure 3.20 and are compared with the vertical orientation of the heat exchanger sample. For the baseline case (i.e., without any drainage channels), the inclination towards the leeward direction reduces the steady state condensate retention by around 8%. The steady state retention which was 9.5 g with the vertical arrangement was reduced to 8.7 g (Refer Table 3.4), by changing the orientation to 15^0 towards the leeward. The findings presented here contradict those of Osada *et*

al. [34], who reported that inclining the evaporator towards the leeward direction increase the condensate retention, and hence causes an increase in the air pressure drop. However, the findings are supported by Kim *et al.* [35], who found a decrease in the condensate retention by inclining the sample toward the leeward side. By inclining the sample to the leeward direction, but the air stream still remaining parallel to the fin surfaces (because of arrangements in the set-up), gravity forces combine with the air shear forces and enhance the drainage rate. Most of the drainage in this orientation takes place at the downstream end of the fin sample.

However, the inclination is not favorable for the effectiveness of the drainage channels, as can be seen in Figure 3.20. The present results also explain the less effectiveness of the inclined drainage channels[12], as compared to the vertical channels, as discussed in the previous sections. With this inclination of the sample, the condensate retention for the baseline case reduces and the retention for the channeled case remains similar, further leading to the degradation in the channel performance. The reduction in the steady-state condensate retention caused by the square channels, which was 19.6% with the vertical orientation, reduces to only 9.6% in this orientation.

3.3.4 Effect of Inlet Relative Humidity

To assess the effect of inlet air relative humidity on the retention characteristics of the heat exchanger, and on the performance of drainage channels, humidity levels were varied. The samples were tested at three different inlet relative humidity levels- 75-77%, 85-87% and 94-96%. The relative humidity, dew point and air temperature were measured using Omega Logger (OM-62). Typical variation of inlet relative humidity, dew point and the air temperature data within an experiment is shown in Figure 3.21. The inlet relative humidity fluctuates between a

[12] The channels were inclined at 45^0 to the vertical, and the performance was compared to the vertical square channels, described in section 3.3.2

maximum and a minimum value at steady state, while the air temperature reaches a constant value.

The variation in the condensate retention characteristics of fin Design 1 at three different inlet air humidity levels is shown in Figure 3.22. The results shown here are for the baseline case, i.e., without any drainage channels. It is evident from the figure that changing the humidity changes the slope of the retention curve, indicating the effect on the rate of deposition of condensate. With increasing humidity levels the slope becomes steeper, thus at higher humidity levels, the rate of deposition becomes higher. Time required to reach steady state was found to decrease with an increase in the inlet relative humidity. The steady-state retention was achieved in around 35 minutes for the inlet relative humidity of 95%, while it took 70 minutes to reach the steady state for the relative humidity of 75%. However, the steady state retention for all the cases remains almost the same. It is the maximum amount of condensate which can be retained under the given geometrical and other operating parameters. The effect of the inlet relative humidity on the steady state retention of Design 1 is shown in Figure 3.23. The steady state retention changes from 9.3 g to 9.8 g if the humidity is raised from 75% to 95%. Thus, the relative humidity has an important role in changing the deposition rate, but has little or no effect on the steady state retention value. It follows that the inlet relative humidity has little or no effect on the drainage characteristics.

Since the relative humidity does not modify the drainage characteristics, there was no significant effect observed on the performance of the drainage channels. Figure 3.24 shows the effect of drainage channels at higher humidity levels (95-96%). As can be compared to Figure 3.13, where the relative humidity was 85-87%, the drainage channels show essentially the same behavior.

The steady state retention shown by the different drainage channels at different humidity levels is compared in Table 3.5.

3.3.5 Effect of Air Velocity

Incoming air velocity has been shown to have an impact on the retention and drainage characteristics [12], [13], [38]. Air velocity in the present experiments was measured at the exit of the fin column, at 7 locations spaced equally along the length of heat exchanger sample. The effect of change of air velocity on the condensate retention/drainage characteristics of fin Design 1 is shown in Figure 3.25. The other operating conditions were kept as previously described. The air velocities considered were 1.5-1.6 m/s, 2.5-2.6 m/s and 3.5-3.6 m/s. As can be seen, once the condensate deposition starts, the slope of the curves (i.e., the rate of condensate deposition) remains almost same for all the three cases. At the highest velocity (3.5-3.6m/s), the drainage is governed mostly by air forces, and the curve of retained mass reaches an asymptotic steady state value after the initial deposition period. The air force pushes all droplets towards the downstream direction and generally drainage does not begins until the complete exchanger is wet, or droplets/bridges cover almost whole surface area. Thus, there is an increase leading to a slight overshoot, after which the drainage process starts. For the lowest velocity case, the major draining mode is the gravity driven flow. So, drainage starts occurring even before the water droplets have been pushed all the way back to the exit of exchanger. Drainage occurs mainly along the tube walls initially (detailed explanation in the visualization section).

However, dynamics of drainage and retention have an impact on the final steady state condensate retention, and thus the steady state retention is different for different cases. Figure 3.26 shows effect of air velocity on the steady state retention of the sample. Decreasing the air velocity from 3.5 m/s to 2.5 m/s increases the steady state retention by 10%, and further decreasing the air

velocity to 1.5 m/s increases the steady state retention by an additional 8%. This relationship between the air velocity and final retention is linear, as shown in the figure.

To assess the effect of change of air velocity on the performance of drainage channels, experiments were conducted for square channels at two different air velocities, and the results are shown in Figure 3.27. As for the baseline case, condensate deposition starts early with the lower velocity. The major difference in the effectiveness of the drainage channels can be seen when the actual drainage through the channels starts. With higher air velocities, the curve for the channeled sample deviates from the baseline case earlier than the lower velocity case. It takes around 20 minutes in the higher velocity case, while it takes more than 30 minutes in the lower velocity case, for the difference between channeled and non-channeled sample to become noticeable. With lower air velocity, as was previously discussed, drainage already starts along with condensate deposition, even before the sample is completely wet. So, the channels do not contribute much to that already occurring drainage initially. With higher air velocities, air forces also push the condensate into the drainage channels, leading to the early effectiveness of drainage channels. However, later when the sample is completely wet in the case of lower velocity, drainage channels start to act and reduce the steady state retention value. The final retention with drainage channels is almost same for cases with different air velocities. However, the retention for the baseline case increases with decreasing air velocity. Thus channels are more effective at lower air velocities.

3.3.6 Effect of Fin Base Temperature

The fin base temperature was measured using thermologgers and type-J thermocouple wires at three locations at the intersection of the sample and thermoelectric device. The temperature was recorded every 10 minutes during the experiment. Though any parametric study was not

performed for the change in the fin base temperature, but since the temperature usually varied within 1-2 ^{0}C for different readings, a plot has been obtained showing the dependence of the steady state retention on fin base temperature. Figure 3.28 shows the variation in steady state retention for the baseline case for fin Design 1 with change in fin base temperature. The plot is used in calculation on measurement uncertainty in Appendix-B.

3.4 Visualization Results

In order to gain deeper insights on the influence of geometrical parameters and operational conditions on condensate drainage and retention characteristics, and to identify physical mechanisms of retention and drainage, visualization experiments were conducted. As previously discussed, for the purpose of visualization, one side of the heat exchanger assembly was kept as a glass plate, and the other side the aluminum plate was extended. The visualization tests were conducted on the all the fin designs with and without channels.

Regardless of the fin geometry and operating conditions, the condensate formation mechanism was found to be same for all fin geometries. Condensate first appeared on the fin and tube surfaces in the form of small droplets. This droplet condensation, however, lasted for a small time, and the droplets grew in size and coalesced to convert to film wise condensation. The time required for the droplet formation and then conversion to the film wise mode, depended upon the operating conditions. Owing to the small size of the droplets and smaller thickness of the film, surface tension forces were dominant during the formation of the condensate.

But with the increase in the condensate film thickness, gravity and air forces also became important. The air shear and pressure force pushed the condensate towards the trailing edge, and hence the film thickness was less near the leading edge, especially for the cases with higher air

velocities. For lower air velocities, the condensate initially was concentrated more towards the leading edge, and then later when the leading section was completely filled, the condensate either drained or was pushed towards the trailing edge. That explains the gradual increase of retained condensate mass in case of lower velocities (Figure 3.25). Generally, the heat exchanger was found completely wet after this initial period.

The condensate film then increases in thickness leading to partially and/or completely filled inter-fin regions, i.e., fin bridges. The condensate menisci start to form and grow at the fin base, and move towards the fin opening. It is difficult for the condensate menisci to grow at the fin opening, because of the presence of sharp corners between the fin turns and the tube wall (Figure 3.29). These corners only promote small menisci, which allows for a drainage path along the tube wall [36]. This observation of growth of the inter-fin bridges was seen in all of the fin designs, except Design 3 (Discussed later in detail). The condensate is also pulled from the fin base to the louver cut end giving rise to louver bridging. Louver bridging also occurred whenever there was fin bridging and the louvers where the two fins bridged, were also bridged.

For all the fin designs, the condensate accumulation was first observed at the bottom of exchanger. Later the accumulation spread along the height of the exchanger and grew in size, but the bottom of the exchanger was always flooded. The rate of condensation does not vary along the entire height of the heat exchanger, because of uniform cooling provided by the thermoelectric device. Thus, condensate draining down the fin column height from top to bottom causes the amount of condensate to be more towards the bottom of the sample. The observation is also evident from Figure 3.30 which shows the velocity profile as measured at 7 different locations equally spaced, on the exit of the fin column. The graph shows the velocity profile at three different time instants. At the beginning of the experiment, when no condensate was

present between the fins and louvers, the air flow was least obstructed and the air velocity measured at the exit did not vary much from top to bottom. When the velocity was measured after 20 minutes of starting the experiment, the condensate was mainly concentrated on the bottom part of the exchanger, hence showing clear decrease in the velocity near the bottom of the exchanger. The velocity at the top and the middle did not change much. However, at the end of the experiment, the condensate was uniformly distributed along the length, again giving almost uniform velocity profile. Though the result is shown only for Fin Design 1, this was observed for every fin design.

In the visualization experiments, it was seen that a condensate droplet (or a larger droplet in the form of film) drains from the exchanger through either of these possible ways, or a combination of them: a) Droplet follows the fin/tube surface to reach the bottom of the exchanger. Different drainage paths were observed while the droplet drained through the fin structure, which have been discussed later. b) Because of air flow forces, the water droplet is pushed to the downstream edge of the fin array and drains down the edge of the fins. This way was observed with the cases where the air velocity was higher. c) The droplet is attracted to the drainage channel by the means of surface tension forces or is pushed by the air shear forces, and then drains down the channel under the action of gravitational pull.

The discussion has been generally applicable to all fin designs, irrespective of the geometry. From this point, each fin design has been separately considered and corresponding observations have been reported. The retention pattern at the fin outlet at the exit and view from the front few minutes after the start of the experiment for Design 1 is shown in Figure 3.31. Initially, i.e., as seen in this figure, fin bridges were observed at the bottom of exchanger. Moreover, the condensate accumulates more towards the downstream end of the exchanger, as can be seen in

the front view, because it was pushed by the air flow forces. However, at lower air velocities, condensate accumulations were first seen on the left end (near to the air entrance). Later the fin bridges increased along the height and depth of the exchanger and grew in size. At the end of the experiment lot of fin bridges were seen.

The drainage pattern at the fin outlet at the exit at three different times during the experiment for Design 1 fin is shown in Figure 3.32. The conditions maintained for this experiment were air velocity=3.5-3.6 m/s and RH=85-86%. At time t=35-40 minutes, the drainage of the condensate just starts. As can be seen from the figure, condensate moves from the top and middle part of the heat exchanger towards the bottom by following a path along the cooling plate. The sustainability of this drainage path along the cooling plate is ensured by the presence of smaller condensate menisci at the fin openings, which exist due to the sharp corners between the fin and plate (Figure 3.29). At this time, partially filled inter-fin regions were seen mainly near the bottom of the exchanger. Also no condensate menisci were present on the glass surface, as it was not cooled. At later times (t=55-60 minutes), inter-fin bridges start growing across the height of the exchanger. The occurrence of completely filled inter-fin regions was also observed. Apart from the drainage path along the cold plate, few new drainage paths were seen. The path following the filled louvers was seen quite a few times. This path occurs intermittently and drains a lot of condensate at a time. Large amounts of condensate build up in a small number of inter-fin regions mostly near the top of the fin column. Suddenly all of this condensate drained down a large portion of the fin column height following the filled louvers, travelling in a zig-zag pattern.

The channels were also seen to be effective from this time in the experiment. As Mclaughlin and Webb [36] have pointed out, all forces act to push/pull the condensate into the drainage channel.

At the louver-cut end, air flow forces push the condensate on the plate surface towards the channel, and the sharp corners cause the surface tension forces to pull the condensate into the channels. Once the condensate is attracted it is pulled down by the gravity. (Figure 3.34) The drainage was first seen through the middle or the rightmost channel (most downstream, away for the air entrance), in case of higher velocities, while it was seen from the first channel in the case of lower velocities. This is because of the reasons already discussed. At later times all drainage channels aided in draining the condensate. In the samples with drainage channels, almost all the drainage occurred through the drainage channels, as seen on the extended portion of the aluminum plate. Figure 3.35 shows the image of draining occurring through the drainage channels, where all of them are effective. The drainage channels mainly acted on the condensate flowing following the drainage path along the aluminum plate, through the louver-cut end.

However, sometimes, a completely or partially filled inter-fin region suddenly drained into the channel, triggering a sudden momentum change for the condensate above it. The zig-zag draining pattern, discussed earlier, is highly momentum dependent. So the trigger caused by sudden draining of a large amount of condensate which was present as a fin bridge, initiates the movement of the partially filled stationary inter-fin bridges above the drainage location. Thus, drainage of condensate from one completely or a partially filled inter-fin region through a drainage channel leads to a cascade of drainage from above that location. This process occurs very quickly. It only takes approximately 5 seconds for condensate draining from near to the top of the fin height to reach the bottom through the drainage channels. This type of drainage is not steady but occurs intermittently. The intermittent drainage is explicit in Figure 3.13 which shows the effectiveness of the drainage channels for fin Design 1. For this fin design, the baseline case shows attainment of an asymptotic steady state, because the drainage path is mainly along the

wall. However, with drainage channels, this steady state is usually an oscillation between maximum and minimum values. Since drainage channels promote the intermittent drainage, this pattern is bound to show up. As the condensation rate is constant, the mass of condensate retained and bridges start forming, when suddenly lot of condensate drains down the channels. Note that this is not the only way the channels drain. As discussed already, they increase the steady drainage occurring along the side wall.

At further later times (t=75-80 minutes), the number of fin bridges increased and the condensate bridges were seen even at the topmost fin. A new drainage path was seen which followed the air water interface at the partially filled inter-fin regions. However, the prominent drainage path was still the one along the plate, as shown in the figure. The drainage path following the bridged louvers (the path along the fin surface, zig-zag path, shown in the figure) occurs rarely, without the drainage channels. So inter-fin bridges once formed, usually stay in the place until the end. In the samples with drainage channels, however, these bridges are not seen that often, as the channels promote the steady state drainage process by pulling condensate from the louver-cut end, which is following the drainage path along the plate. Even if an inter-fin bridge is formed, it is drained by the mechanism of intermittent drainage, explained above. Most of the draining thus takes place through drainage channels.

Another advantage of the drainage channels is that they have the capability to reduce the louver bridging. The drainage channels pull the condensate from the louver-cut end. This was evident by looking at the drainage paths which occur with the drainage channels. All the drainage paths which were seen without drainage channels, and depended on louvers being bridged, drained insignificant amount of condensate with the drainage channels in place. With drainage channels,

all the other drainage paths become less frequent, and the paths through the channels drained the maximum amount of condensate.

The effectiveness of shallow channels has been in question in the previous research related to drainage channels [36]. However, in the experiments performed here, the shallow channels also worked well, and in some cases better than the deeper channels. The reason was clear in the visualization tests. As already discussed, drainage channels enhance the drainage either thorough pulling the condensate from the louver cut end, or by the cascading effect caused by the sudden drainage of an inter-fin bridge. Now, if the channel is deep enough to carry that volume of water, it will directly drain it at the bottom of the exchanger. But if the channel is not deep, there are a lot of chances of spilling and overflowing. Again, if the channel overflows onto an inter-fin region which is empty, it might cause bridging in some cases. However, in most of the cases, the spilling of condensate takes place mostly at the bottom or the middle part of the exchanger. Now, for the reasons discussed before, these regions are mostly partially or completely filled. Sudden spilling of water over these filled regions disturb the equilibrium, transfer momentum to the stationary filled regions and hence trigger the release of condensate already present there. Thus, again, the zig-zag type of drainage comes into play, and enhances the drainage. Figure 3.36 shows in detail this phenomenon of working of channels illustrating how the pulling and spilling of the condensate further enhances the drainage process.

This effect of overfilling and spilling the condensate is further demonstrated in Figure 3.14 and Figure 3.16 which show the effect of changing dimensions for a given geometry of a drainage channel. For the rectangular geometry, the channels having dimensions 1x1 mm show lot of oscillations in the retention pattern, indicating lot of intermittent draining, as compared to the 1x2 channel, which shows almost a steady increase of retained mass until the final steady state is

attained. Similarly, for the triangular geometry, the channel with 45^0 and 90^0 included angles show much more oscillations than the deeper 22.5^0 included angle channel, which shows the steady increase.

However, decreasing the depth of the channel does not always increase the performance. For example, the 90^0 include angle channel, which have the lowest depth perform worse than the deeper channel. If a channel is very shallow, it will not even be able to carry the condensate until the next or the further next inter-fin region, after pulling the condensate from the inter-fin region or the louver cut end. The shear caused by the channel walls on the condensate inside the channel reduced the velocity of the condensate drastically. The channels were always found overfilled and due to this, it failed to attract more condensate from the louver-cut end. The location of spilling the condensate is also important. With the angled square channels, due to their orientation (Refer Figure 2.13), the spilling not only took place at the bottom part of the exchanger, but also above the middle. The spilling mostly occurred at the regions which were already empty, hence in this way it caused the fin bridging to increase near that region. Moreover, spilling was more in this case as the gravity force was not directly acting on the condensate inside the channel, but was reduced by a factor due to the inclination.

The drainage pattern at the fin outlet at the exit at three different times during the experiment for Design 2 fin is shown in Figure 3.33. The conditions maintained for this experiment were air velocity=3.5-3.6 m/s and RH=85-86%, the same as were maintained for fin Design 1. Design 2 differed from Design 1 in terms of geometrical parameters, but the major difference is in the shape of the fin structure, as viewed from the air side. Design 1 has a more flat fin design, while Design 2 has a slight triangular orientation of the fin.

At t=35-40 min, and at times before that, the retention characteristics were similar to those of Design 1. Droplets first emerge, which coalesced to form film, and due to gravitational force, the partially filled inter-fin regions were first spotted at the bottom of the fin. At later times, t=55-60 min, drainage paths started appearing. Apart from the drainage path along the wall, which was prominently seen in Design 1, there was another drainage route which was seen more frequent than the former. As seen in the figure, the zig-zag wavy path following the fin geometry was one of the prominent routes for condensate drainage. This was similar to the drainage path which occurred with the presence of drainage channels in Design 1. The drainage was not steady, but intermittent with this path.

At further later times (t=75-80 minutes), the drainage path discussed above was found the prominent route for drainage. Also, not many bridges were seen as compared to Design 1. Complete filling of inter-fin regions was very rarely observed. The bridges occurred only as the partial filing of the inter-fin region. Moreover, the bridges were not stationary as were observed in the non-channeled samples of Design 1. They changed in size and location a lot of time during the experiment. The variability of the location and size of the inter-fin bridges could be the effect of the existence of intermittent drainage path and the triangular shape of the fin.

Again, the existence of this intermittent drainage path and very rare occurrence of completely filled inter-fin regions can be justified by the triangular shape of the fin. Also, despite the small louver and fin spacing, this fin design showed the least amount of condensate retention among all the fin designs tested. (Refer Figure 3.12 and Figure 3.1) The least retention might be the result of different drainage characteristics caused by the triangular shape of the fin. Previous researchers [36], [51], however, have found that triangular fin shape leads to increase in the condensate retention.

In order to understand the effect of the fin shape on condensate retention/drainage characteristics, it is important to know the mechanism of formation of inter-fin bridges, as the bridges contribute a major part in the total mass retained. Usually, the formation of fin bridges starts at the fin base, and not at the fin opening, because of the presence of sharp corners. (Refer Figure 3.29). When the condensate meniscus reaches the louver cut end, the combined effect of surface tension and the gravity force causes it to grow towards the fin opening. Further, if the fins have slope, as the ones shown in Figure 3.37 , it becomes easier for the bridge to grow. The gravity force pulls the condensate at the upper fin, which makes the air-water interface skewed. This causes the surface tension force to act on the air water interface at the lower fin, to make the interface non-skewed again (i.e., to make the contact angle equal to the water-metal contact angle). In this way, the bridge grows as more water flows into that region.

The fins tested earlier (in the previous works) were the ones which have negative slope at the upper fin and positive slope at the lower fin for an inter-fin bridge, making the fin opening smaller than the fin base. In the present experiments, due to the slope of the fins, the fin opening is larger in size than the fin base. Now, in this case, gravity causes the air water interface to move towards the fin opening at the bottom fin, causing the interface to skew at the top fin. Surface tension force thus acts, and causes the interface to move, and the filled region to grow. This growth, however, works up to a certain size of the filled region. If the size becomes large, the gravity force is large causing the surface to skew, but the surface tension forces cannot pull the heavy bulk of water. This causes the gravity to dominate, and the interface is completely pulled at the bottom fin, causing the inter-fin condensate bridge to suddenly break and flow the condensate to the next bottom fin. This sudden flow again disturbs the equilibrium at the bottom inter-fin region, causing a cascade of drainage to occur. This phenomenon is shown in Figure

3.38. This type of drainage is similar to the intermittent drainage caused due to the presence of drainage channels, discussed earlier in the drainage characteristics of fin Design 1. Thus, caused by the combined action of gravity, which is the dominating force in this case, and slope of the fins, the fin bridges did not grow much in size and draining occurred through the wavy path. Thus, only partially filled inter-fin regions were observed. At the end, condensate was only retained at the fin base, but because of very small non-louvered length of the fin, this amount was small. Nonetheless, that amount was sufficient to sustain the drainage path along the wall. Thus this fin design had the least amount of steady-state condensate retention.

Further, the nature of the retained condensate was much more dynamic than in Design 1. The fin bridges quite often varied a lot in location and size with time. This variation might be the explanation for the continuous drainage pattern of this fin design as observed in the dynamic dip tests (Refer Figure 3.1). In Design 1, without the drainage channels, fin bridges once formed usually stayed there until the end, as there was no strong action of any dominating force like in Design 2. But with drainage channels, fin bridges were reduced, due to the ability of the channels to pull the condensate from the louver-cut end.

An interesting observation with this fin design was the inability of drainage channels in reducing the condensate retention or modifying the drainage characteristics (Refer Figure 3.4, Figure 3.7, Figure 3.17) Now, with the visualization results, that inability can be understood. First and foremost, as already discussed, the drainage is pretty good in Design 2 even without drainage channels, due to the shape of fins, so there is very little scope of improvement. Unlike Fin Design 1, there was not any presence of completely filled inter-fin regions. The inter-fin regions were either partially filled or only that much which enabled sustainability of the drainage path along the wall. This observation was made at the end of the dynamic dip tests, when Design 1

showed a lot of bridging, while Design 2 had little or almost no inter-fin bridging. Further, for Design 1, drainage channels generally acted on completely filled inter-fin bridges, and cause the cascade above that bridge to occur, resulting in enhanced drainage. A form of zig-zag intermittent drainage was exhibited. Here, as there was not any presence of filled bridges, intermittent drainage already occurred due to the shape of fins, hence channels had little opportunity to act on.

Further, the amount of condensate draining along the tube wall was quite similar to that in Design 1, other than the intermittent draining. The non-louvered length for both the designs was same; hence, effectively the amount of condensate draining along the wall would be the same. Moreover, channels acted on the condensate draining along the wall, and on the condensate which was filled in louvers by pulling it from the louver-cut end, in Design 1. This action of channels reduced the louver bridging in Design 1 up to some extent. The ability of a channel to attract water from the louver-cut end depends on the geometrical parameters of the fin and the channel. The ineffectiveness of drainage channels could also be explained on the basis of louver gap. The louver gap is the distance between two louvers in the horizontal plane. It can be obtained, using:

$$L_g = L_p \sin \alpha \tag{3.4}$$

For Design 1, the louver gap is 0.96 mm, owing to its higher louver angle (Refer Table 2.2) almost equal to the channel dimension (1 mm). For Design 2, it is 0.50 mm, much lower than the width of almost all channel geometries tested (the minimum width is 1mm). So, the magnitude of the capillary pressure caused by the channels may not be higher than the capillary pressure caused by the louver gaps, and therefore not capable of attracting water from the fin stock.

Fin Design 3 and Design 4 were also tested with visualization experiments, with and without drainage channels. They had geometrical parameters different from those of Design 1 and 2, but their shape was similar to Design 1. As already observed in the quantitative measurements (Figure 3.12), the designs had a similar retention/drainage behavior as Design 1. This fact was also observed in the visualization tests. Similar to Design 1, most of the drainage occurred through the drainage path along the wall, in the absence of drainage channels. Completely and partially filled inter-fin regions were also identified, which were more or less stationary. Rare occurrence of the intermittent drainage pattern was observed, in the absence of the drainage channels. Drainage channels were effective as was previously observed in the quantitative tests (Figure 3.18, Figure 3.19), and enhanced the drainage through creation of new drainage routes.

Though the louver gap for fin Designs 3 and 4 was lower than Design 1, and also lower than the channel dimension, the channels seemed to enhance drainage by promoting the drainage path caused by sudden draining of one inter-fin bridge. However, the louver gap for this design was higher than Design 2, which had no effect of drainage channels on its retention characteristics. Also, although all the fin designs have very different fin and louver spacing, still Designs 1,3 and 4 have almost the same retention per unit area (M_A), as seen previously. As discussed already, the fin gap for all the fin designs is almost the same which determines the ease for a fin design to form inter-fin bridges. The fin gap and louver gap for all the fin designs is reported in Table 3.6. As can be seen, Design 2 has also similar fin gap as other designs, still has lower retention. This discrepancy is because of different fin shape. Thus, even with smallest fin and louver spacing, Design 2 has the lowest retention.

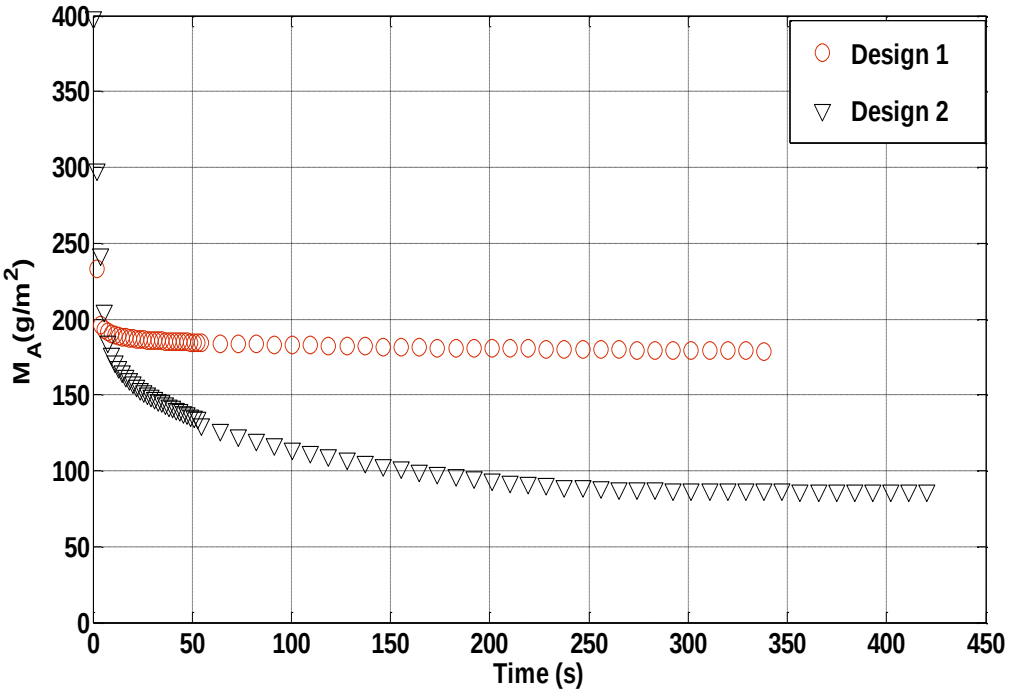


Figure 3.1 Effect of fin design on water retention characteristics (dynamic dip tests)

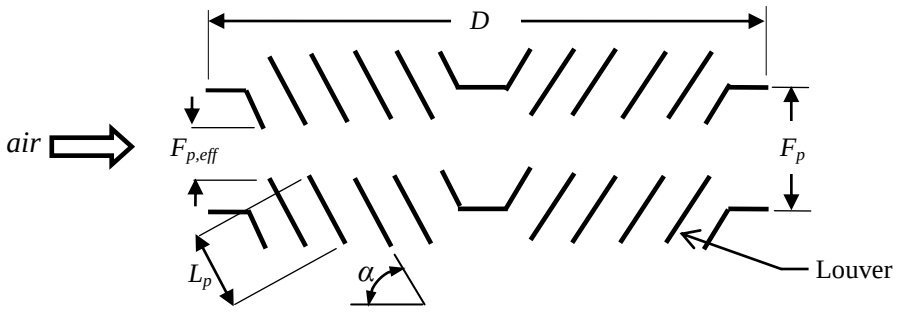


Figure 3.2 Cross section of a multi louvered fin showing the effective fin spacing

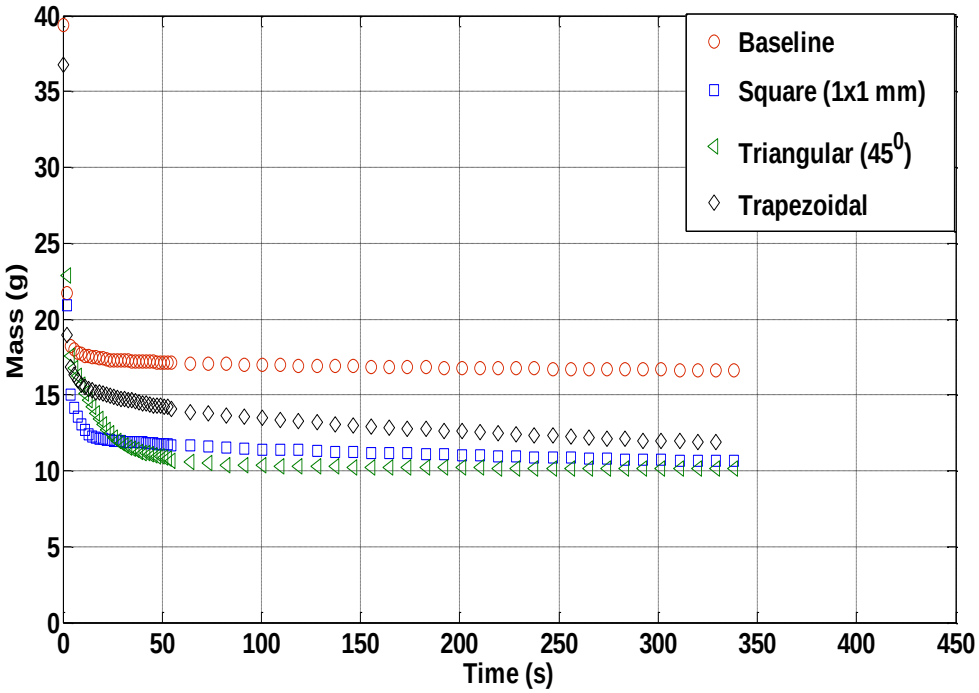


Figure 3.3 Effect of channel shapes on condensate retention for fin Design 1

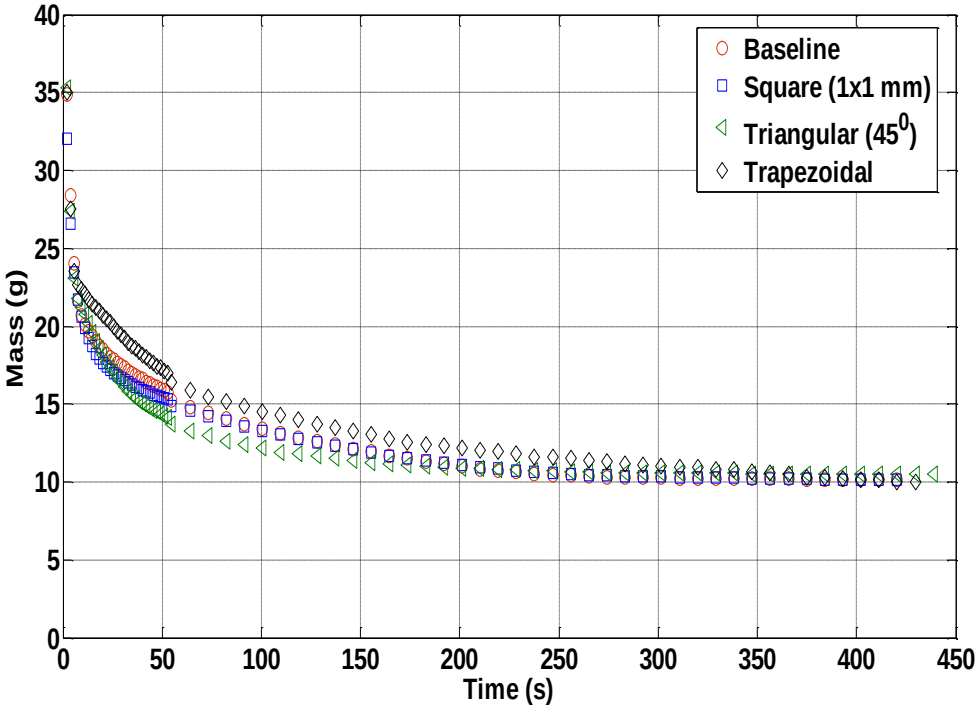


Figure 3.4 Effect of channel shapes on condensate retention for fin Design 2

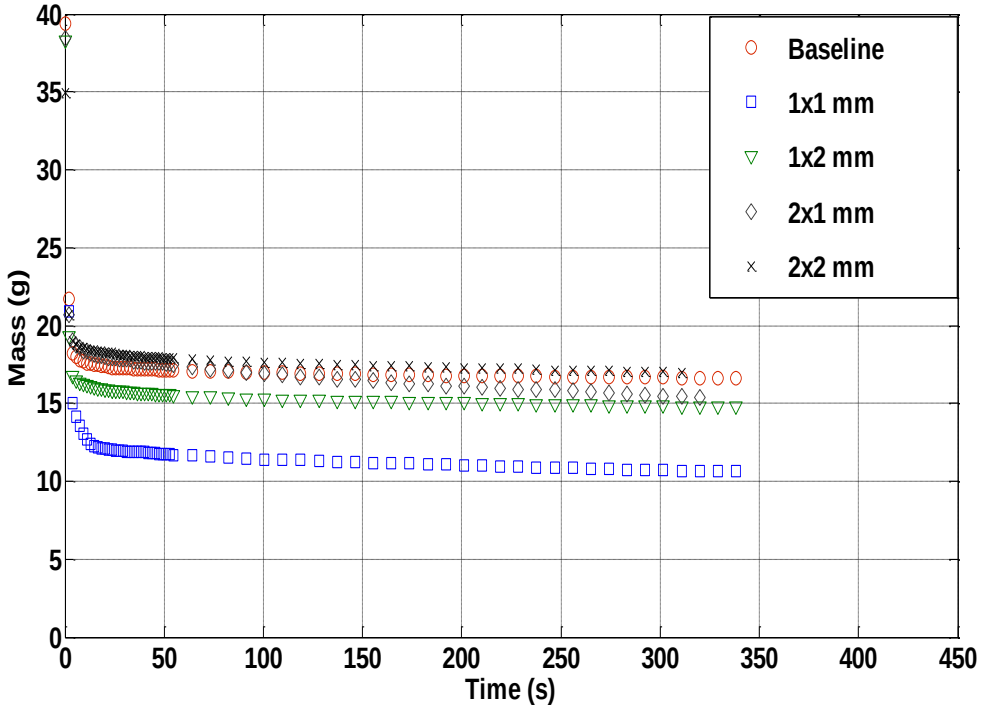


Figure 3.5 . Effect of changing dimensions on water drainage for rectangular geometry fin Design 1 (dimensions specified as wxd)

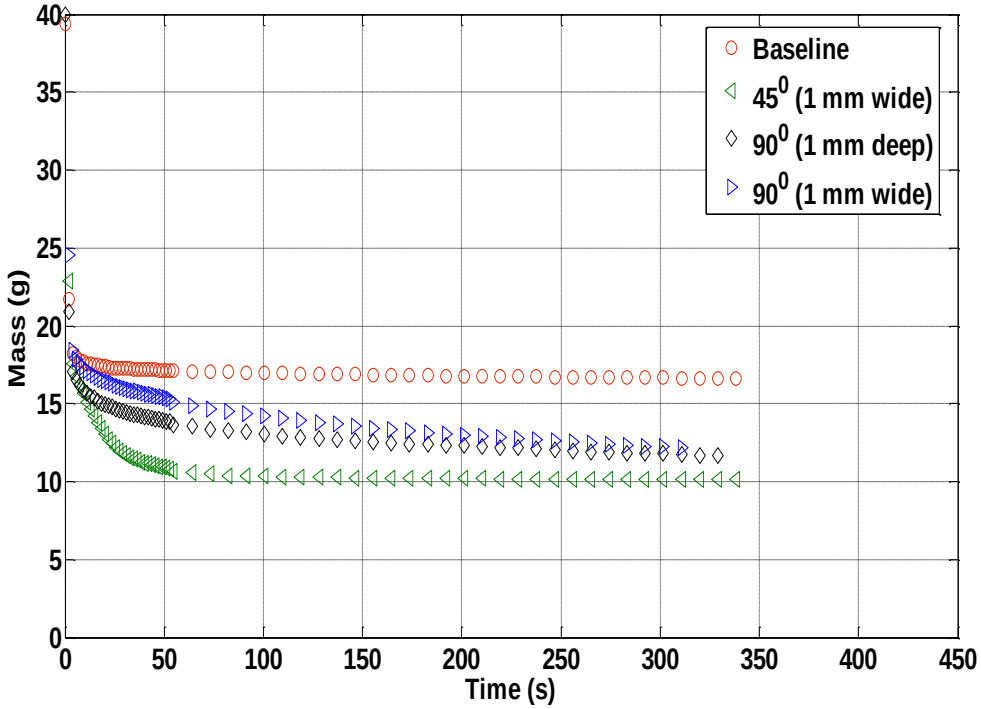


Figure 3.6 Effect of changing dimensions on water drainage for triangular geometry fin Design 1

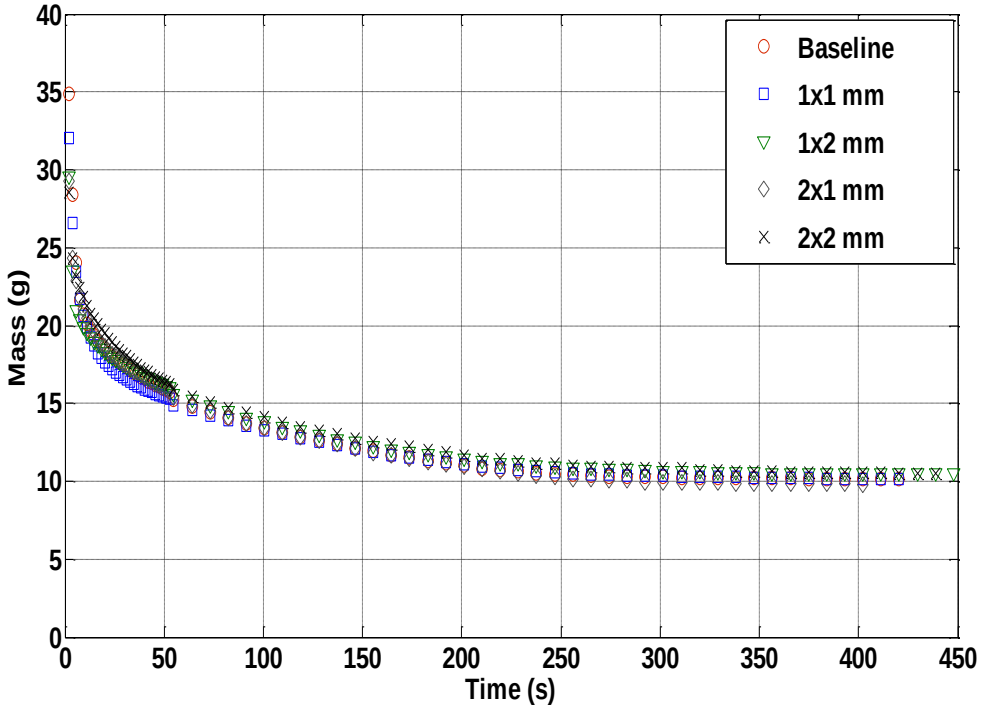


Figure 3.7 Effect of changing dimensions on water drainage for rectangular geometry fin Design 2 (dimensions specified as wxd)

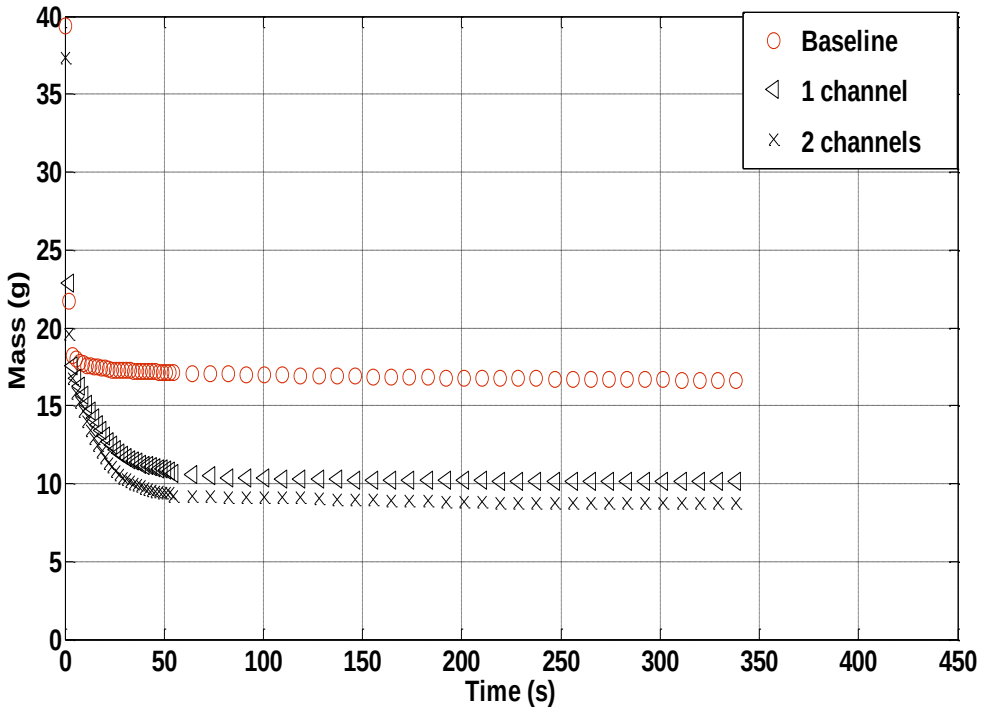


Figure 3.8 Effect of Number of Channels on Retention for Fin Stock Design 1 for Triangular (45°) Channels

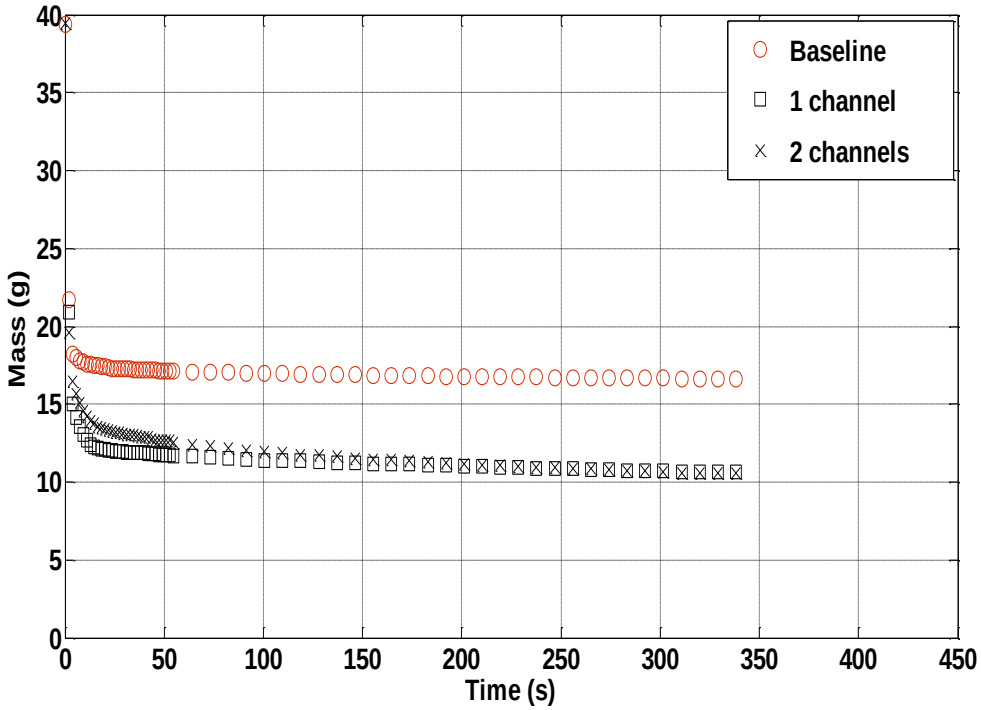
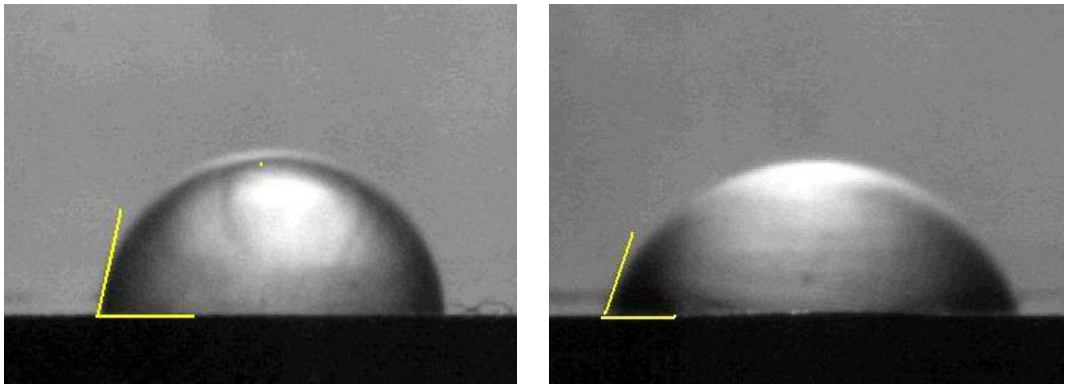


Figure 3.9 Effect of number of channels on retention for fin Design 1 for square (1×1 mm) channels



a) **b)**

Figure 3.10 Contact angle on aluminum surface a) before acetone washing, b)after acetone treatment

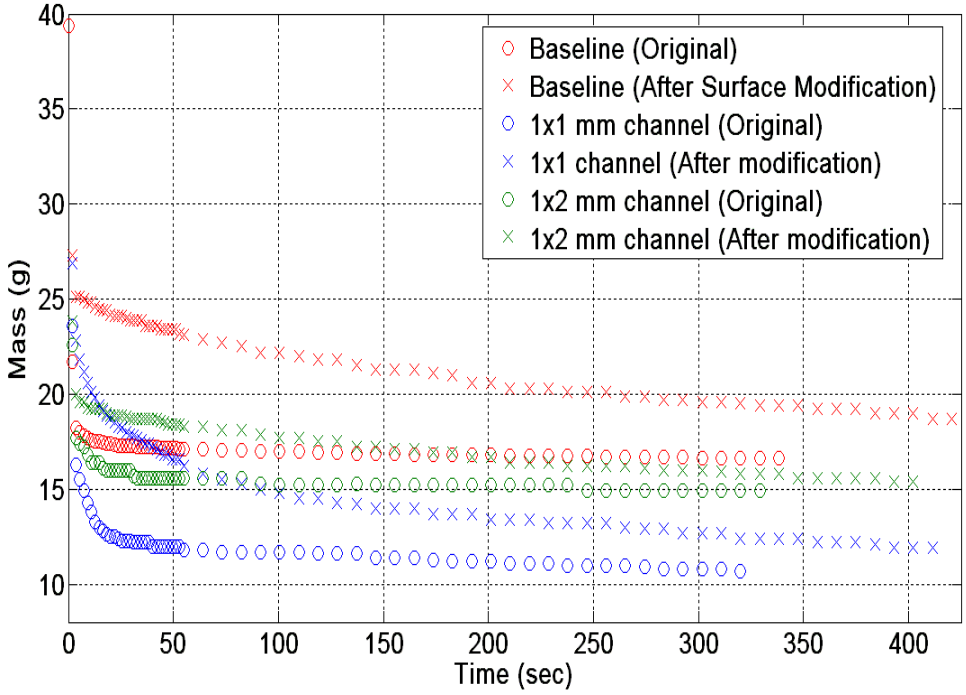


Figure 3.11 Effect of changing surface wettability on retention characteristics for fin Design 1

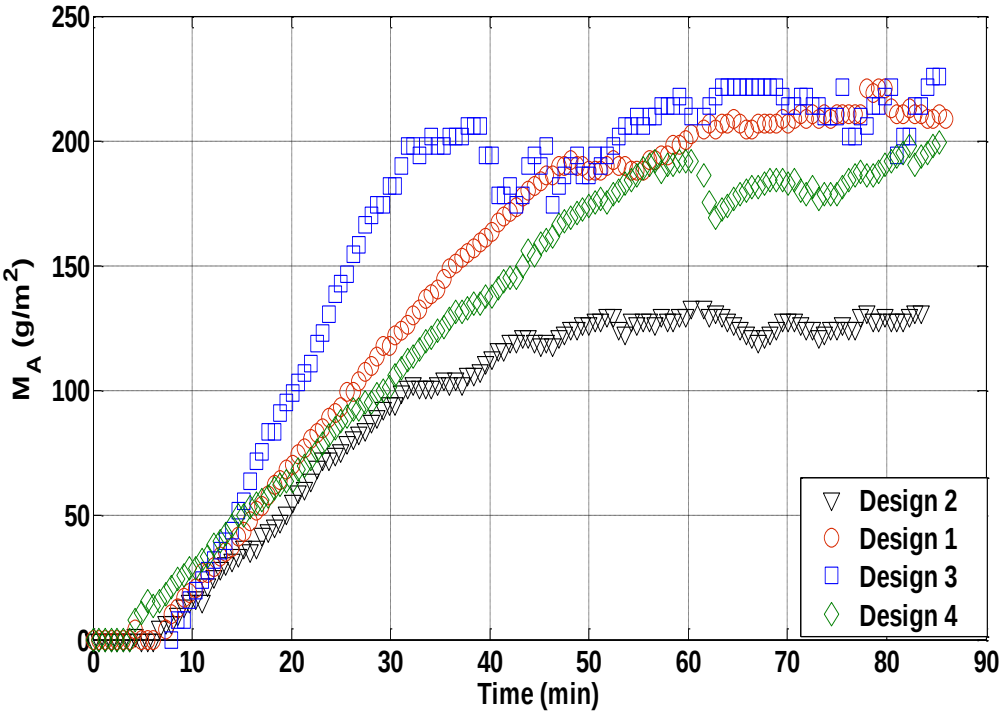


Figure 3.12 Comparison of fin stock designs using the small wind tunnel tests

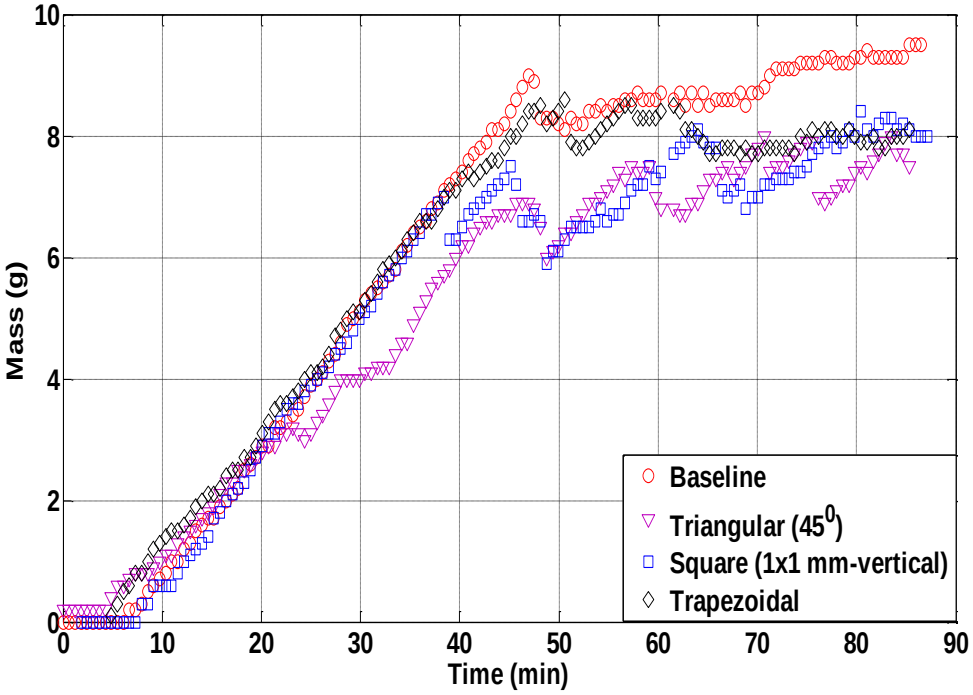


Figure 3.13 Effect of different channel geometries on condensate retention behavior of fin Design 1 (actual condensate retention tests)

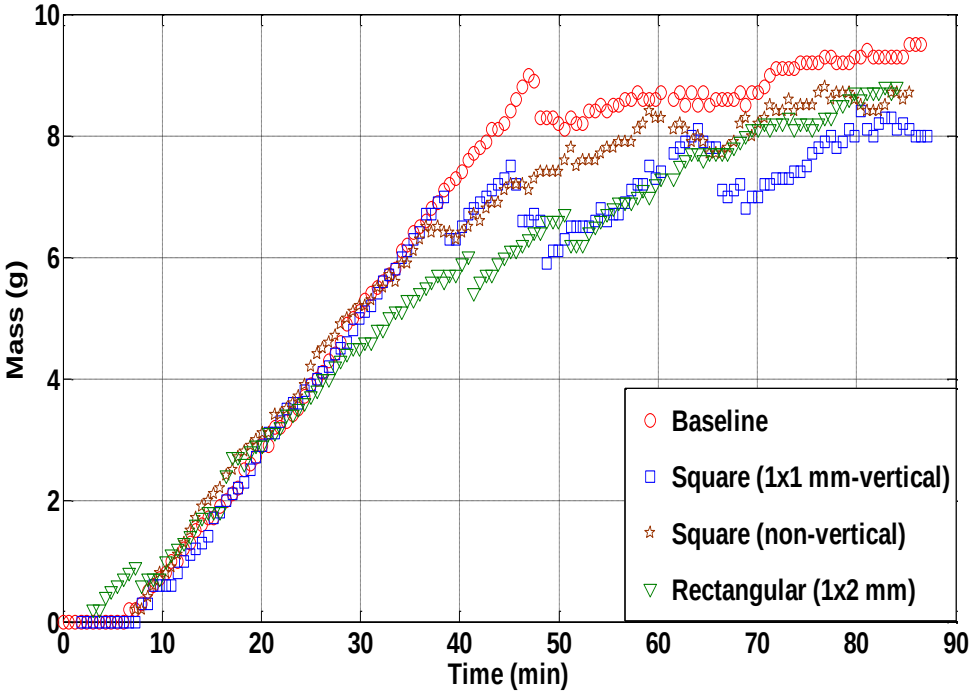


Figure 3.14 Effect of changing dimensions and orientation of the rectangular shaped channels on condensate retention characteristics of fin Design 1

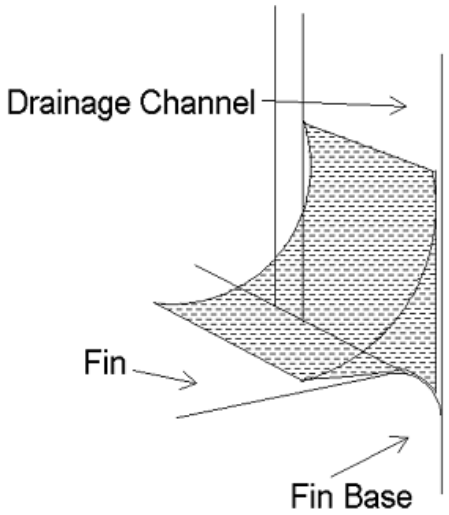


Figure 3.15 Spilling of the condensate onto the fin-channel intersection [36]

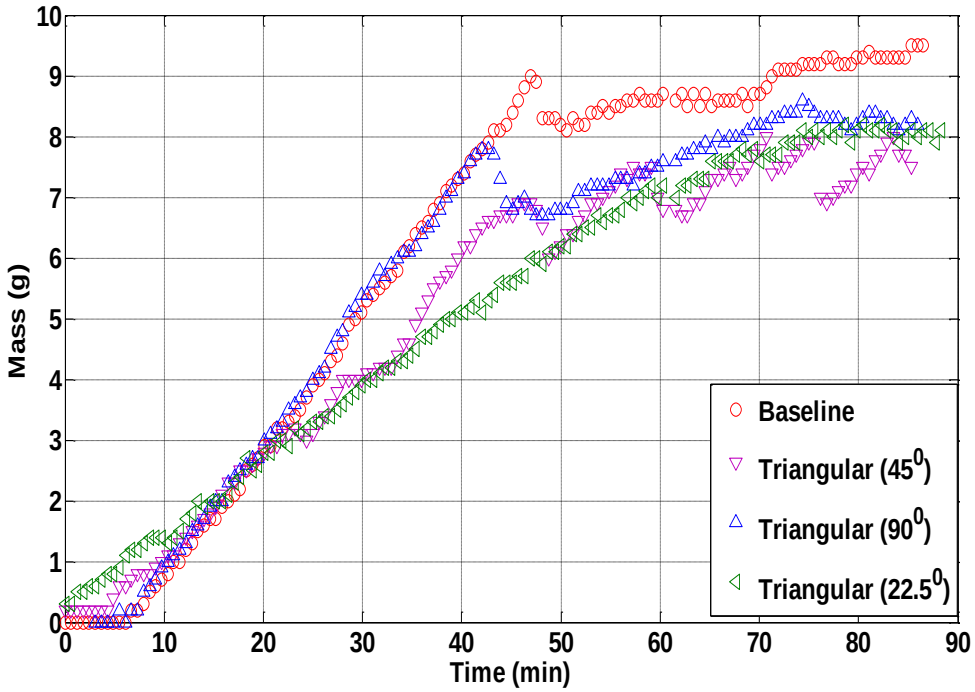


Figure 3.16 Effect of changing dimensions of the triangular shaped channels on condensate retention characteristics of fin Design 1

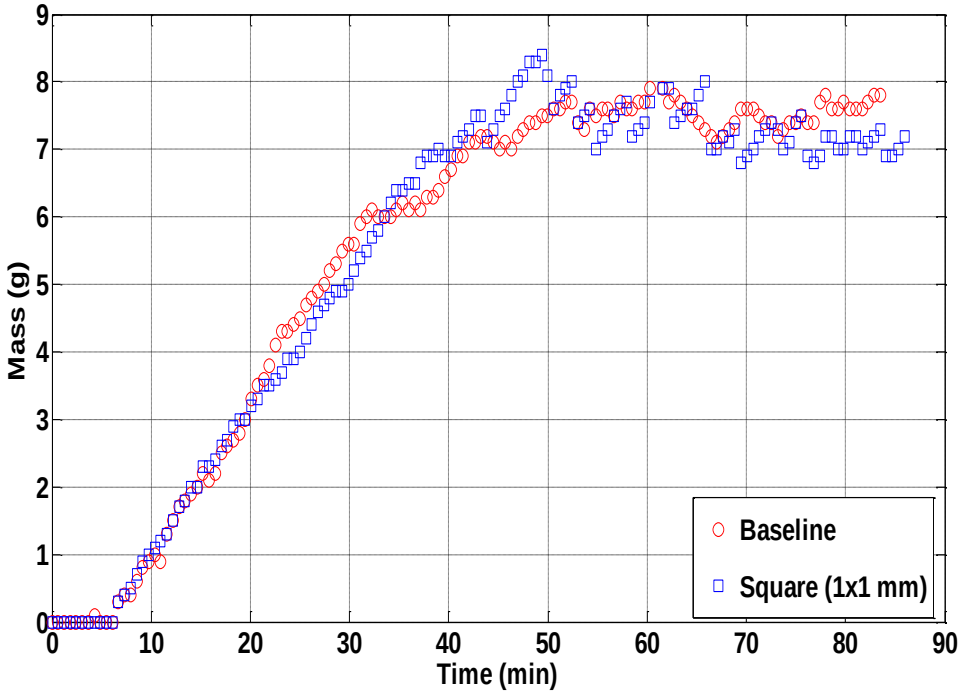


Figure 3.17 Effect of drainage channels on condensate retention of fin Design 2

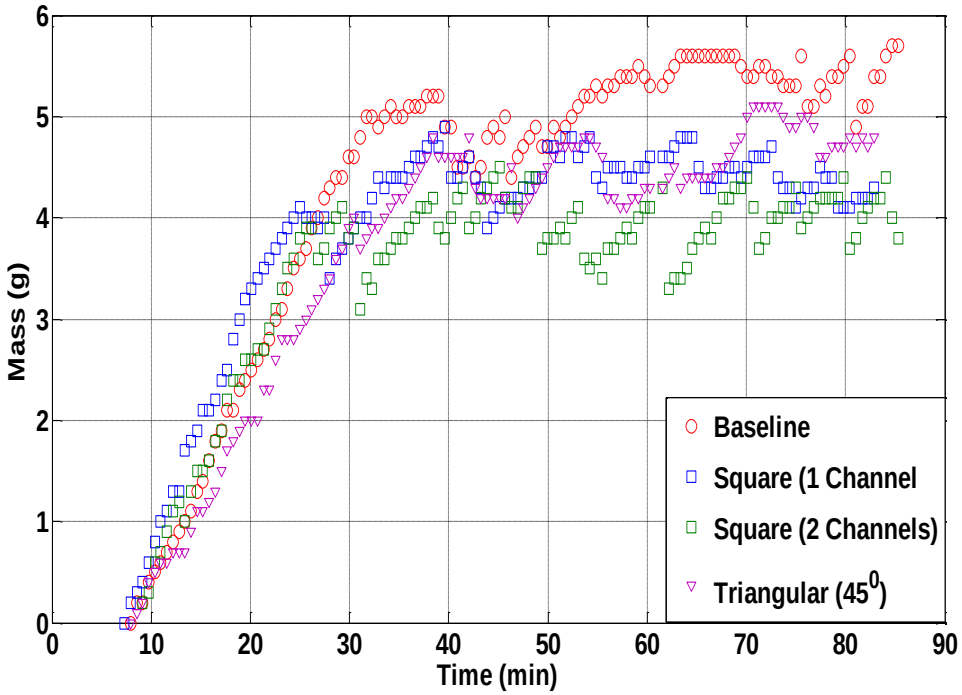


Figure 3.18 Effect of drainage channels on retention characteristics of fin Design 3

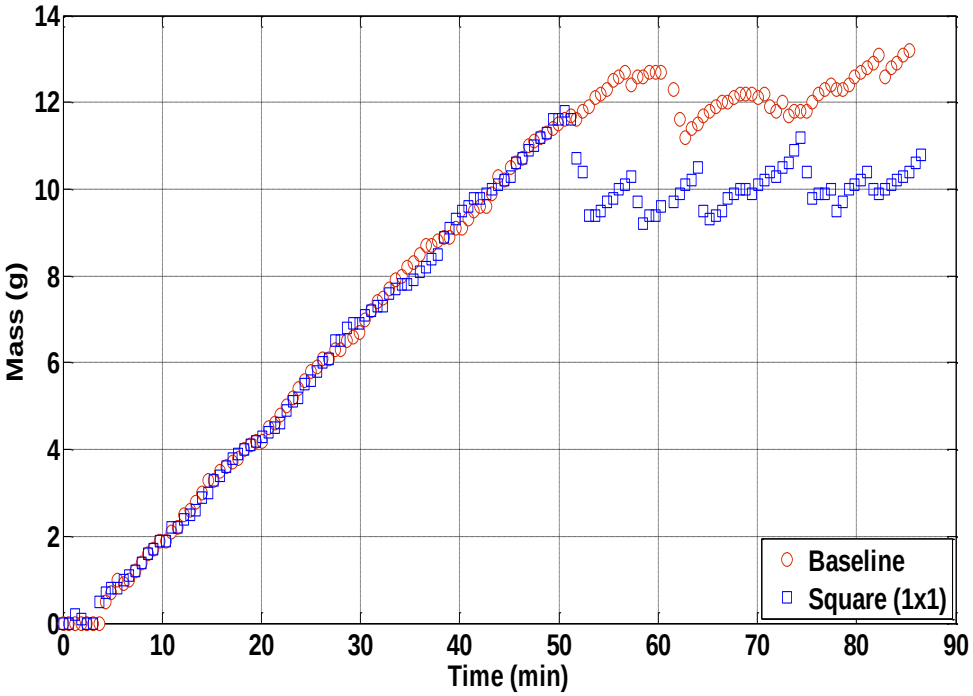


Figure 3.19 Effect of drainage channels on retention characteristics of fin Design 4

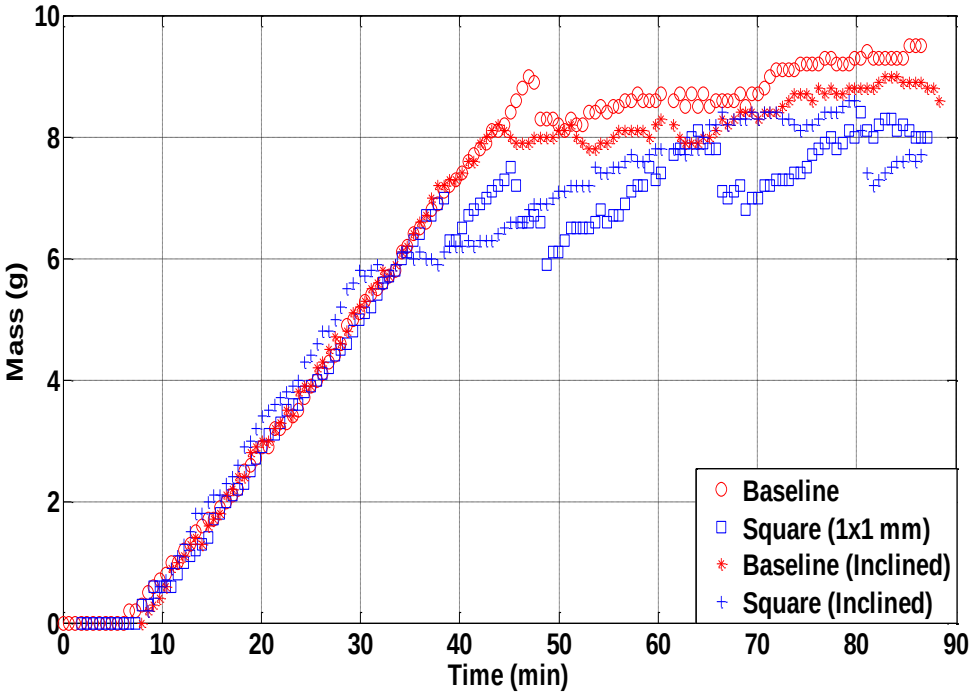


Figure 3.20 Effect of inclining sample at 15^0 to the vertical on the condensate retention of Design 1

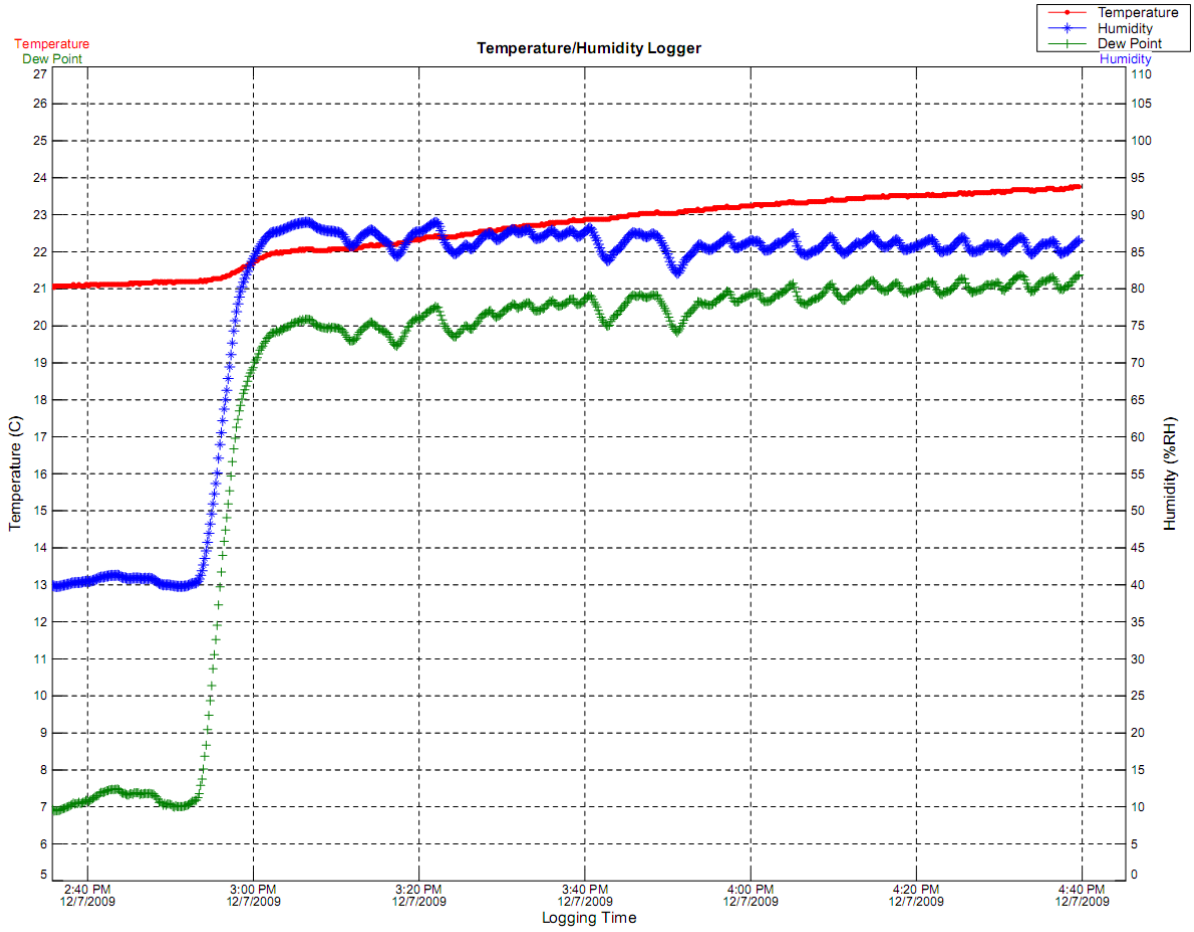


Figure 3.21 Typical humidity and air temperature measurement data[13]

[13] Data obtained using Omega Log Logger (OM-62) and processed by a software (Omega Log Logger Interface Software) provided by Omega Engineering, Inc., Stamford, CT, USA

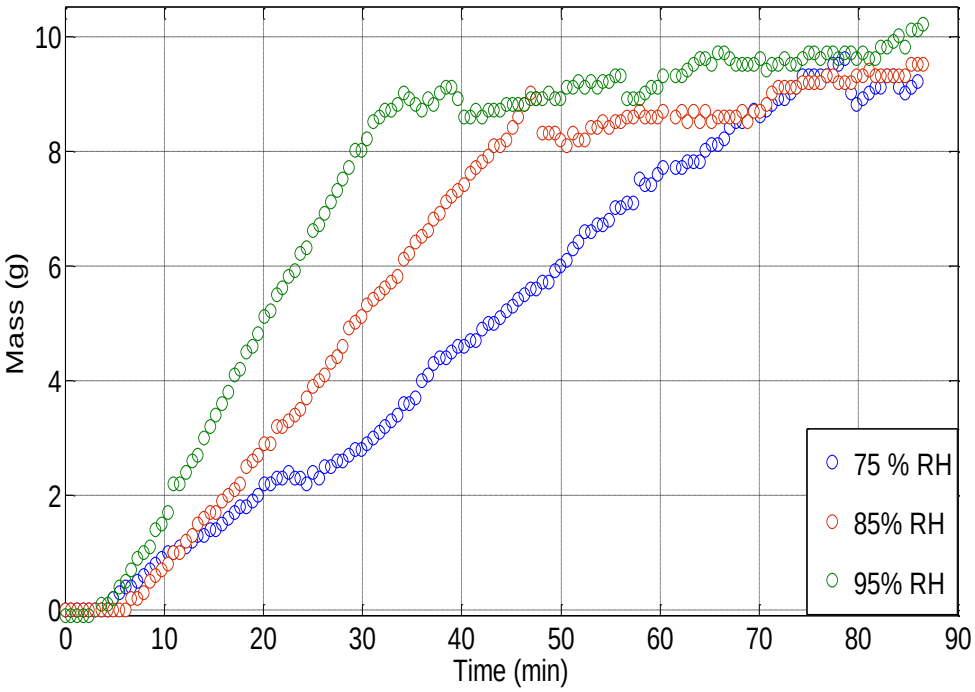


Figure 3.22 Effect of inlet relative humidity on the condensate retention of fin Design 1

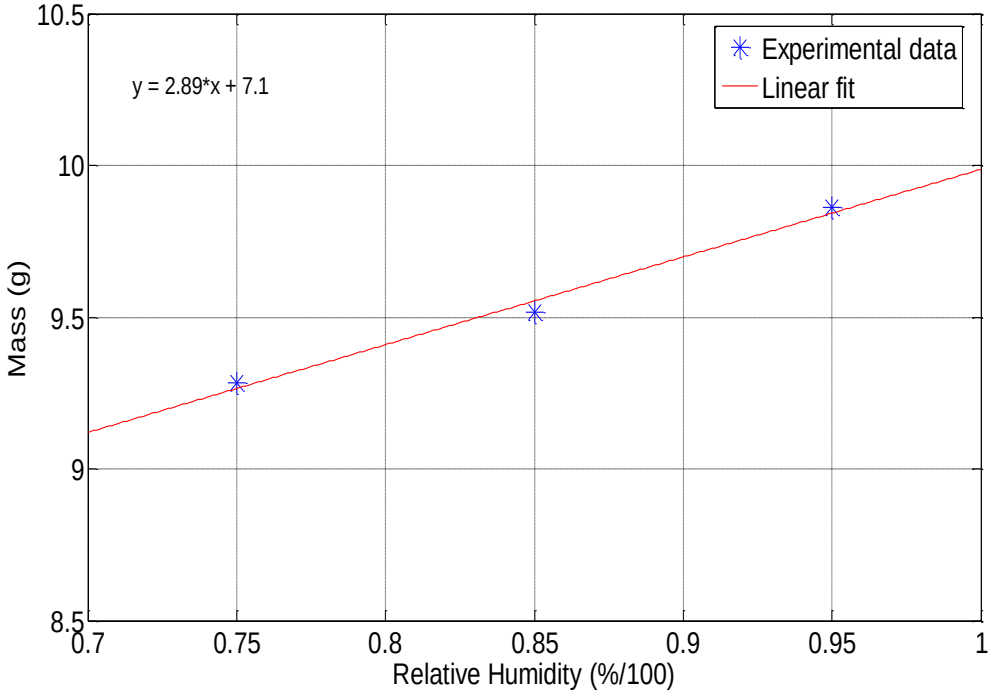


Figure 3.23 Linear fit showing the effect of inlet relative humidity on steady state retention of fin Design 1

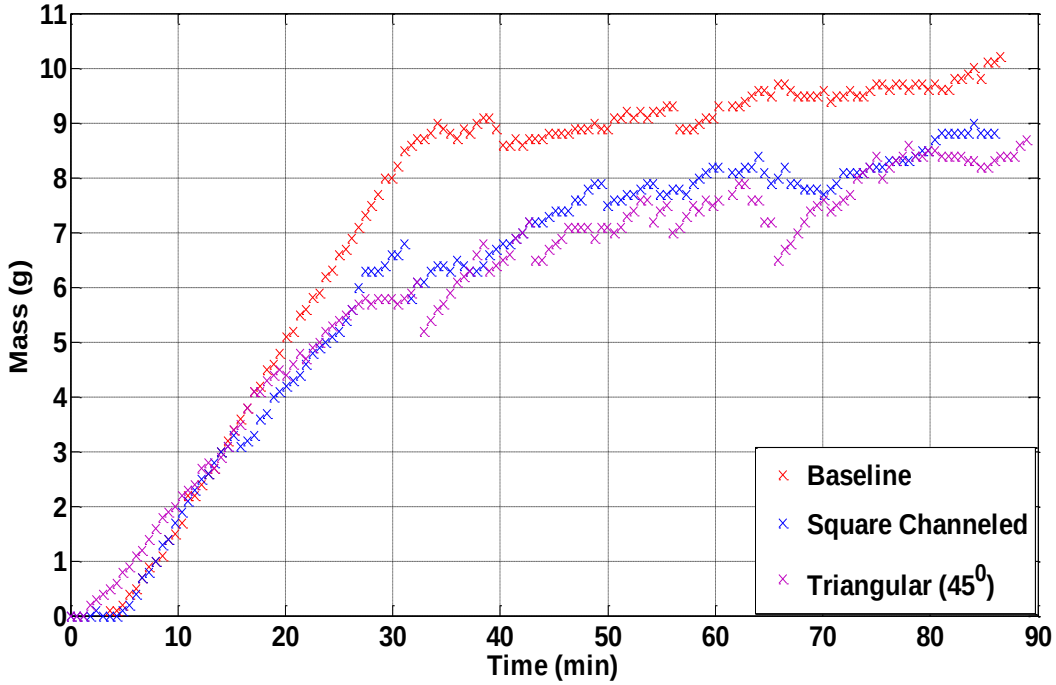


Figure 3.24 Effect of drainage channels at high humidity (95-96%) on fin Design 1

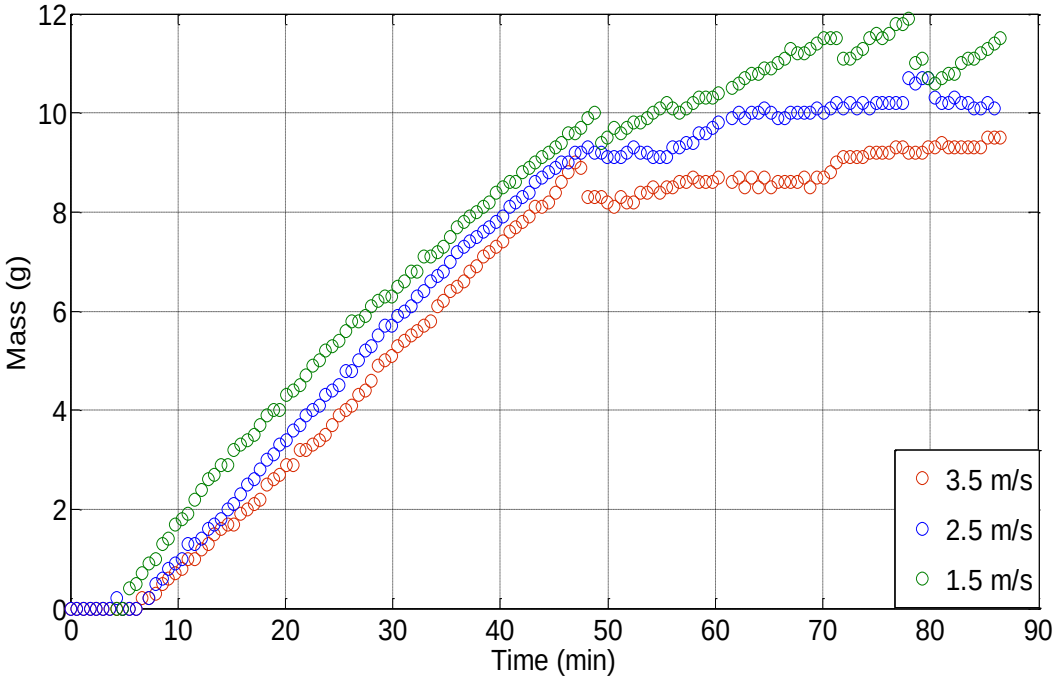


Figure 3.25 Effect of air velocity on the condensate retention characteristics

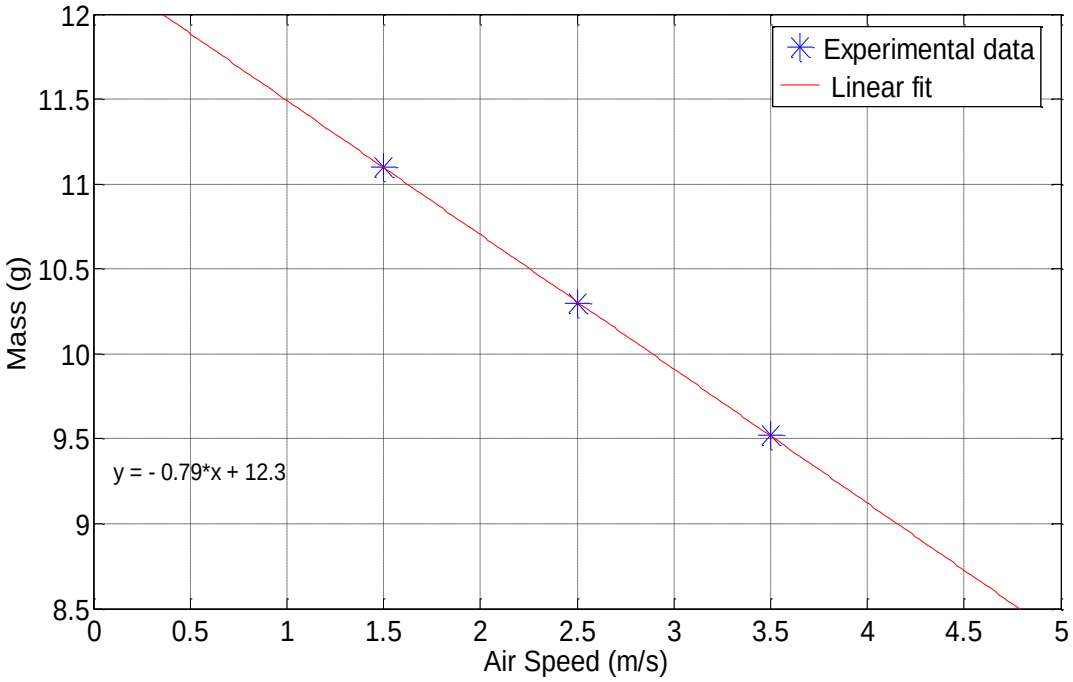


Figure 3.26 Linear fit showing the effect of air velocity on steady state retention of fin Design 1

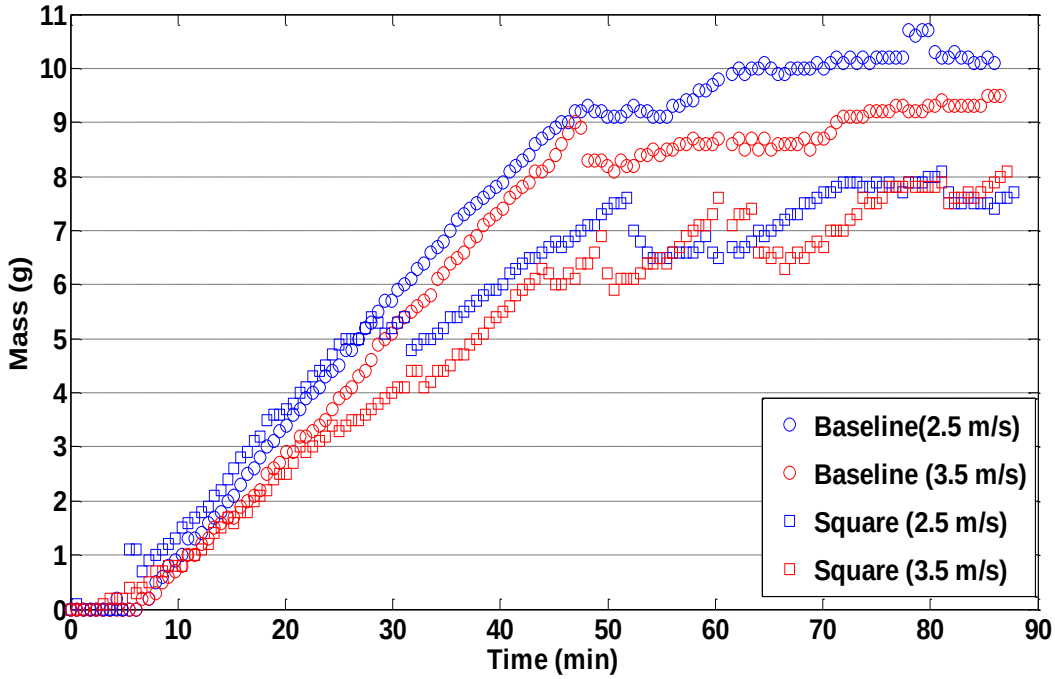


Figure 3.27 Effect of air velocity on the drainage channel performance

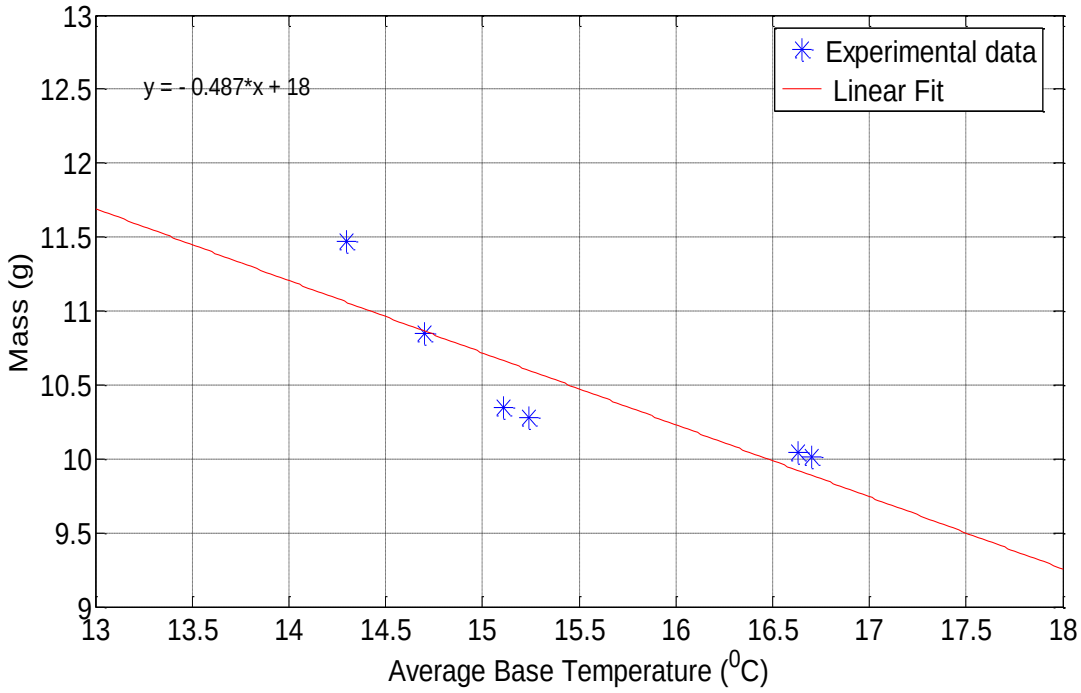


Figure 3.28 Linear fit showing the dependence of final retention on fin base temperature

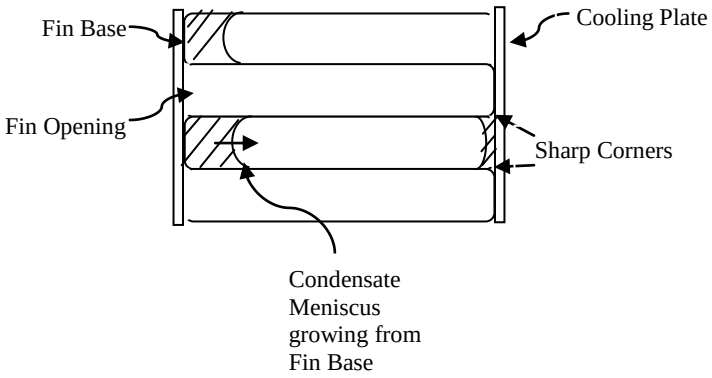


Figure 3.29 Formation and growth of inter-fin bridges at fin base

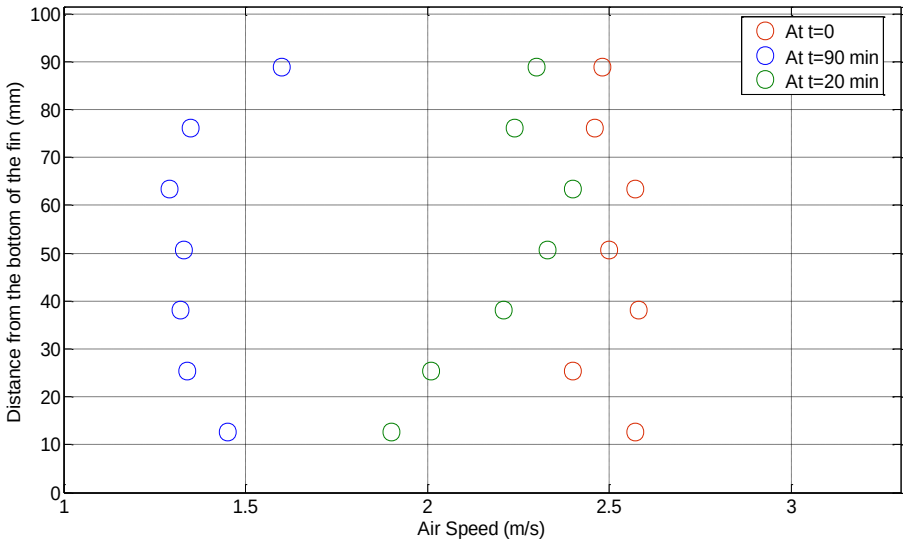


Figure 3.30 Air velocity profile at the exit of fin column for fin Design 1

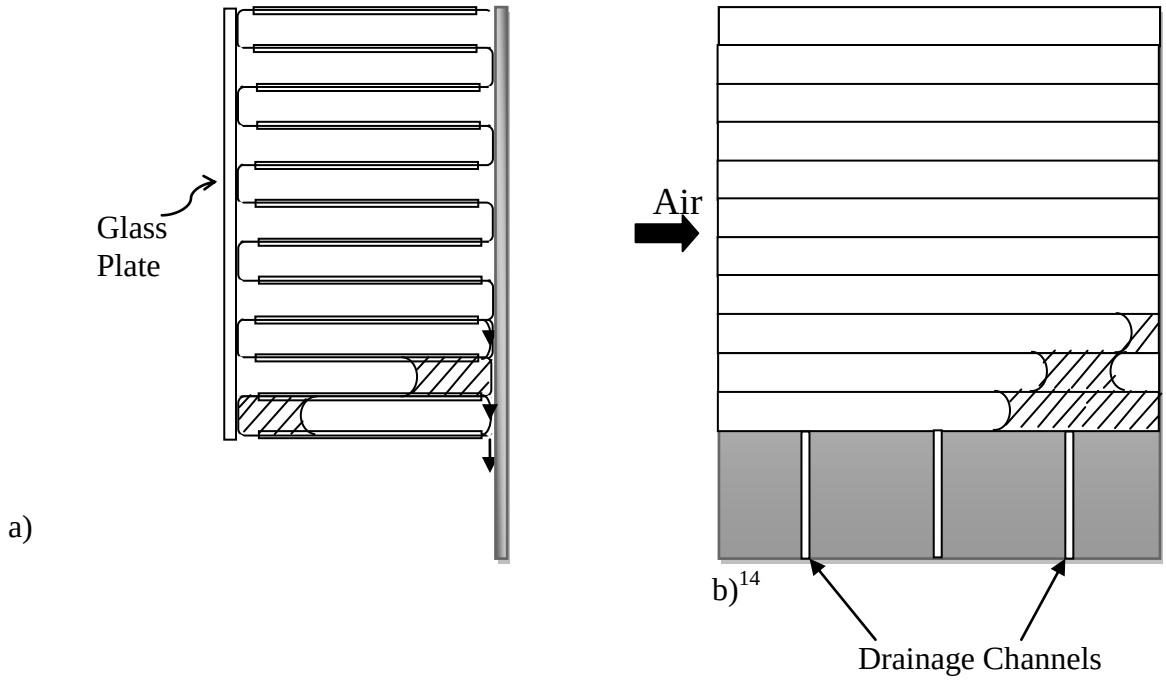


Figure 3.31 a) Downstream and b)front view of fin design 1 at the initial stages of the experiment

[14] The exact view from the front side should be the alternate patches of condensate, as two adjacent inter-fin spaces are not visible in that view. However, for the sake of understanding, this exaggerated view is presented.

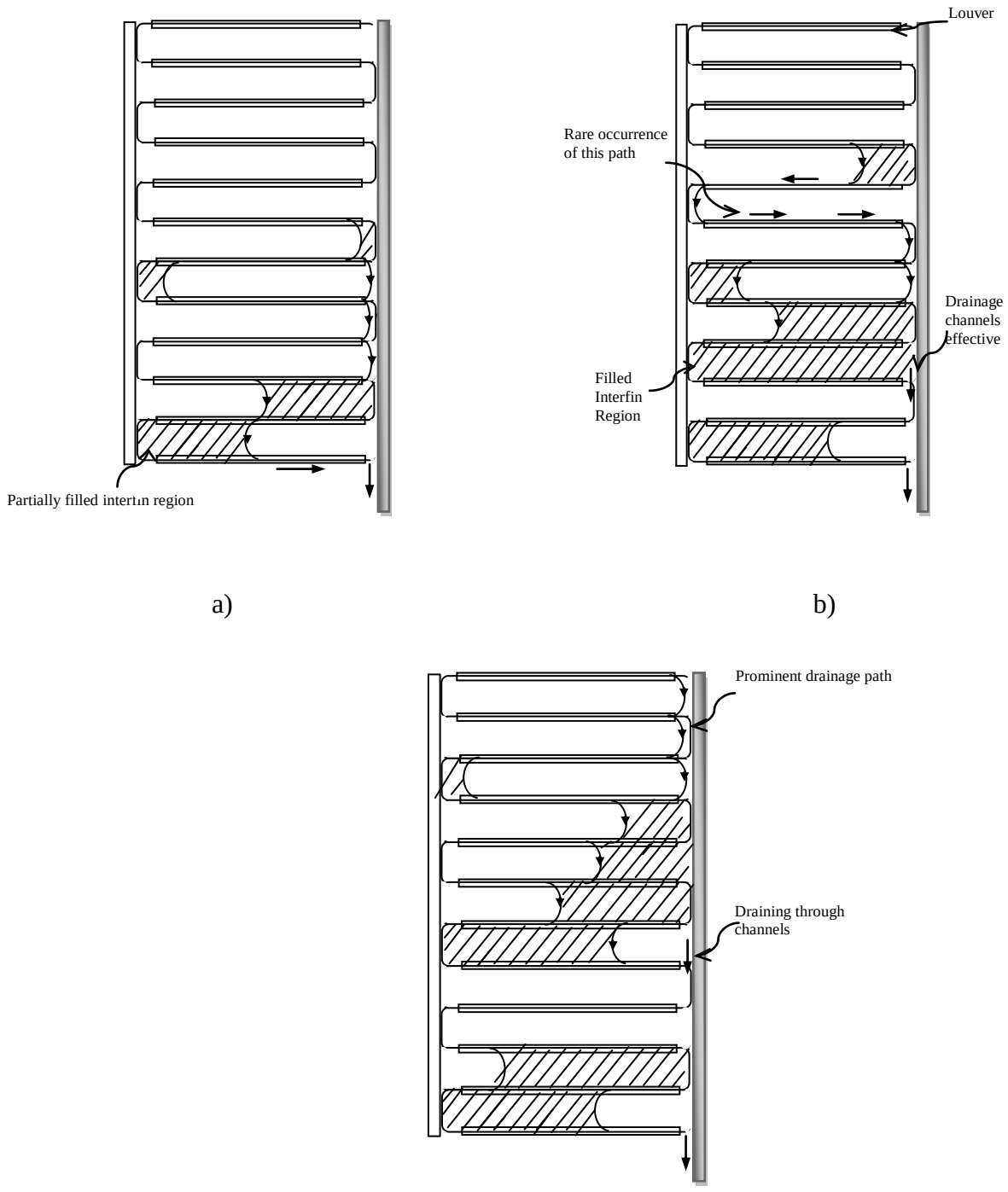


Figure 3.32 Schematic diagram of draining pattern at fin outlet for fin design 1 at a) t=35-40 min, b) 55-60 min, c)t= 75-80 mins, after the start of the experiment

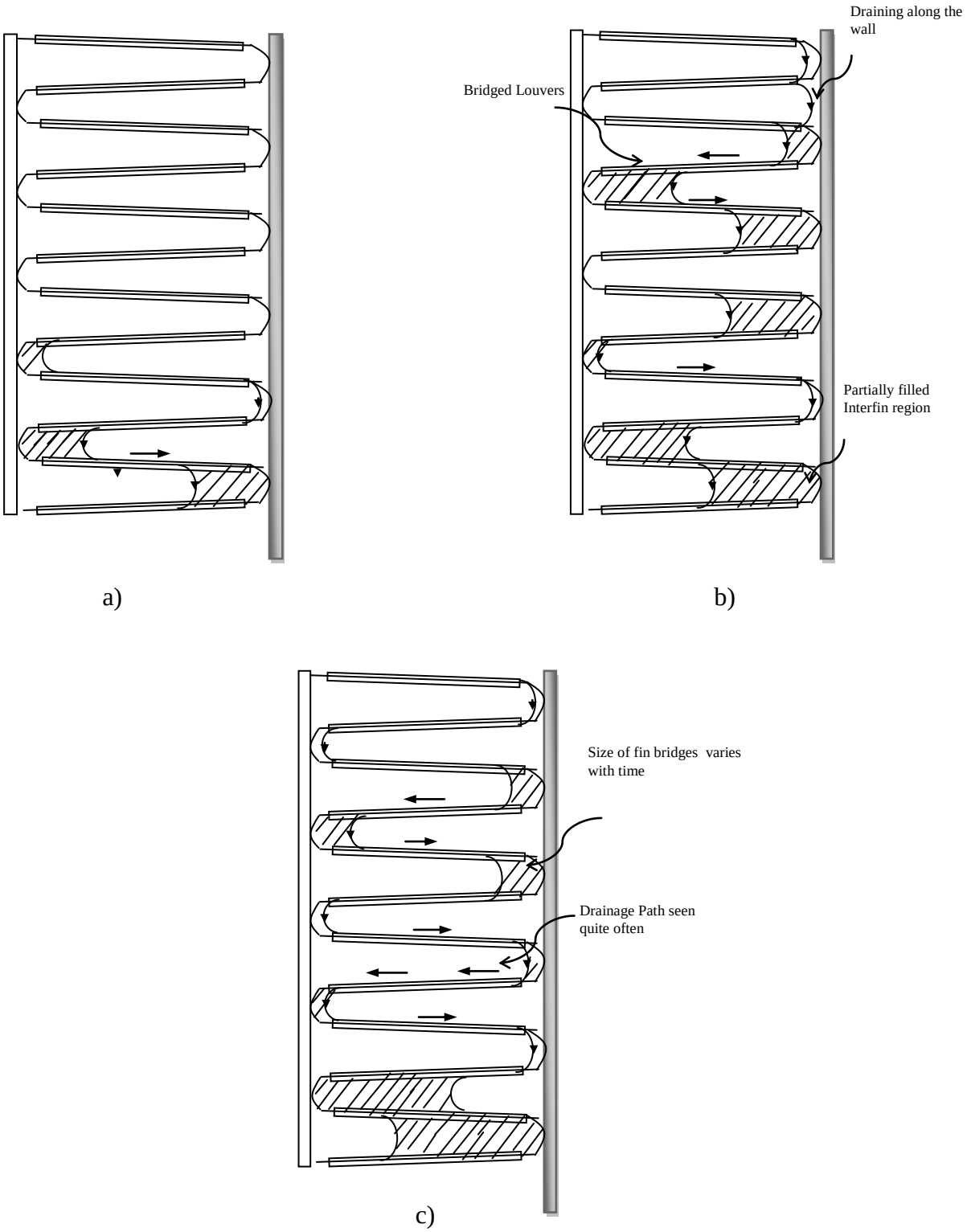


Figure 3.33 Schematic diagram of draining pattern at fin outlet for fin design 2 at a) t=35-40 min, b) 55-60 min, c) t= 75-80 mins, after the start of the experiment

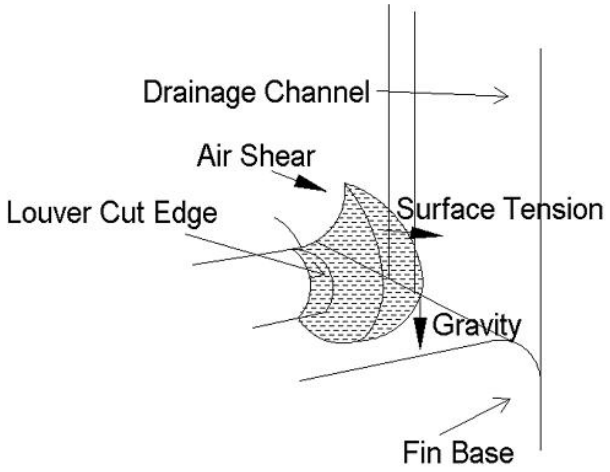


Figure 3.34 Forces acting on a droplet near a drainage channel [36]

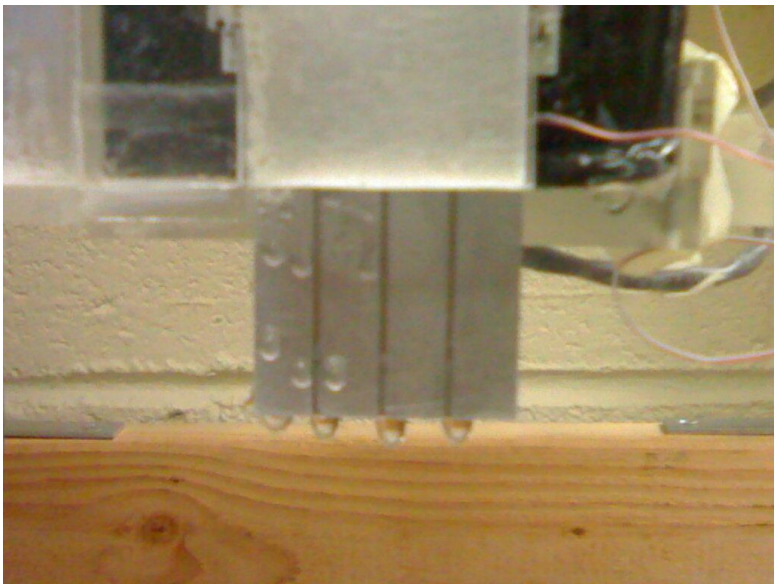


Figure 3.35 Draining occurring through drainage channels

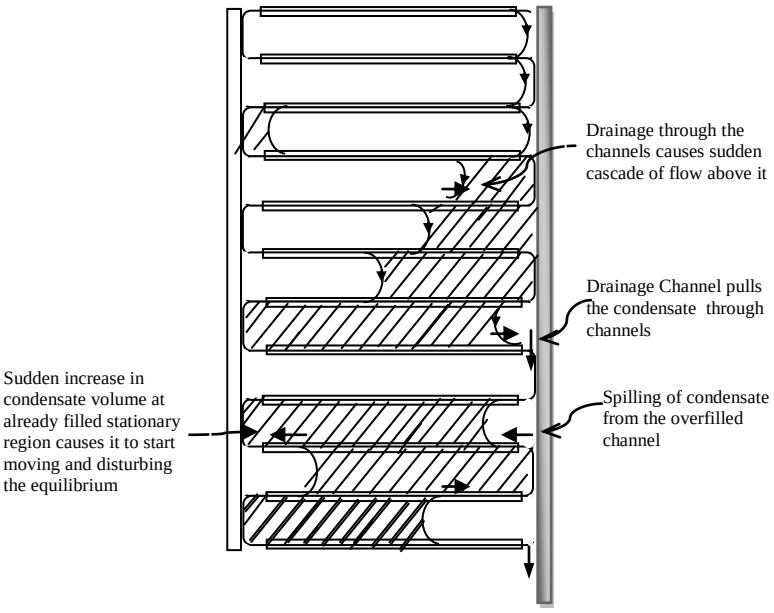


Figure 3.36 Effect of drainage channels: pulling and spilling

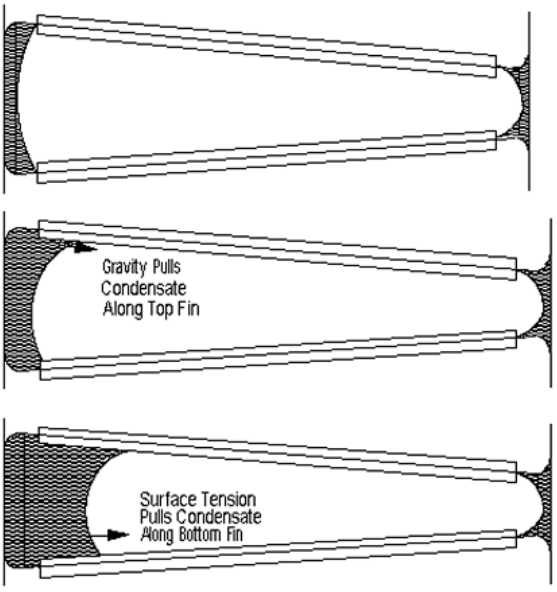


Figure 3.37 Growth of fin bridge for the triangular fins tested by [36]

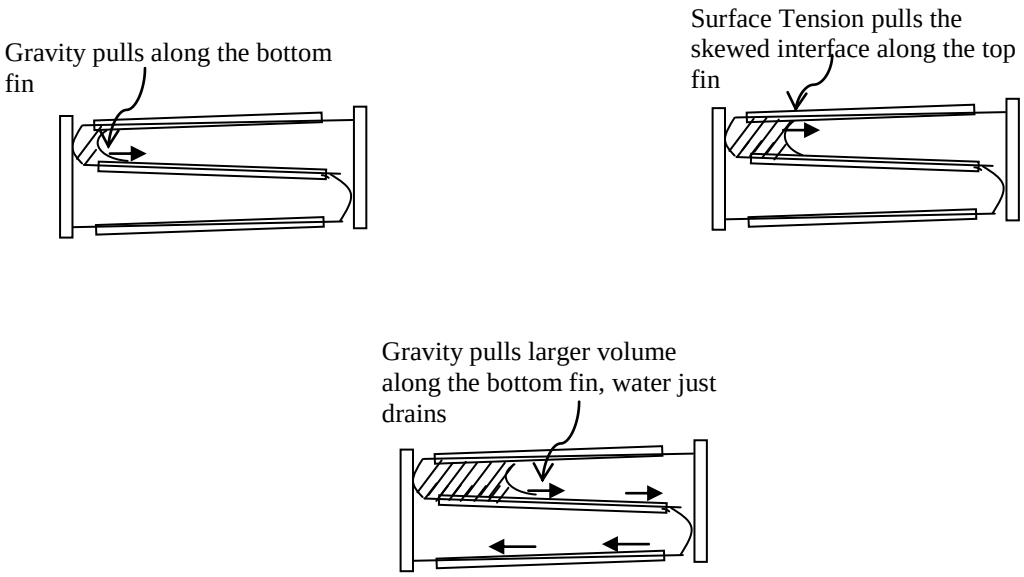


Figure 3.38 Drainage occuring due to shape of fins of Design2

Table 3.1 Static retention data for design 1 samples (dynamic dip tests)

Channel	*Static Retention[15] (g)*	*% retention reduction*
Baseline	16.7	---
Rectangular:		
1×1 mm		
1 channel	10.8	35%
2 channels	10.7	36%
1×2 mm	14.9	11%
2×1 mm	15.4	8%
2×2 mm	16.9	-2%
Triangular:		
45° 1 mm wide		
1 channel	10.2	39%
2 channels	8.8	47%
90° 1 mm wide	12.3	26%
90° 1 mm deep	11.9	29%
Trapezoidal		
1mm wide 120°	12.1	28%

Table 3.2 Static retention data for design 3 and design 4 samples (table top wind tunnel tests)

Channel	*Design 3[16]*		*Design 4[17]*	
	Static Retention[18](g)	% reduction	Static Retention(g)	% reduction
Baseline	5.4		12.6	
Rectangular:				
1×1 mm	4.4	18.4%	10.1	19.6%
1×1 mm (2 channels)	4.0	26.5%		
Triangular: 45° 1 mm wide	4.6	15%		

[15] The static retention is calculated by taking average of the readings for the last minute of test
[16] Tests were conducted at air speed=3.5-3.6 m/s, and RH=85-87%
[17] Tests were conducted at air speed=2.5-2.6 m/s, and RH=85-87 %
[18] The static retention is calculated by taking average of the readings for the last 10 minutes of the test

Table 3.3 Static retention data for design 1 and design 2 samples (table top wind tunnel tests)

Channel	*Design 1*[19]		*Design 2*[20]	
	Static retention[21](g)	% reduction	Static retention(g)	% reduction
Baseline	9.5		7.56	
Rectangular:				
1×1 mm	7.7	19.3%	7.27	4%
1×1 mm (non-vertical grooves)	8.7	8.4%		
1×2 mm	8.5	10.9%	7.3	3.4%
Triangular:				
22.5° 1 mm wide	8.0	16%		
45° 1 mm wide	7.3	23.2%		
90° 1 mm wide	8.3	13.3%		
Trapezoidal:				
1mm wide 120°	8.0	16%		

Table 3.4 Effect of sample inclination on the static retention of fin Design 1

Sample	*Vertical Orientation*[22] *($\theta_F=0^0$)*	*Inclined Sample ($\theta_F=15°$)*
Baseline	9.5	8.7
Square Channeled (1 x 1 mm)	7.7 (19.3%)[23]	7.9 (9.6%)

Table 3.5 Effect of inlet relative humidity on the static retention of fin Design 1

Sample	*Low Humidity*[24] *(%RH=85%)*	*High Humidity (%RH=95%)*
Baseline	9.5	9.9
Square Channeled (1 x 1 mm)	7.7 (19.3%)[25]	8.3 (16.2%)
Triangular Channeled (45° included angle)	7.3 (23.2%)	8.0(19.2 %)

[19] Tests were conducted at air speed=3.5-3.6 m/s, and RH=85-87%
[20] Tests were conducted at air speed=2.5-2.6 m/s, and RH=85-87%
[21] The static retention is calculated by taking average of the readings for the last 10 minutes of the test
[22] Retention expressed in grams.
[23] The numbers inside the brackets indicate the % reduction in the steady-state condensate retention caused by the drainage channels, over the baseline case
[24] Retention expressed in grams.
[25] The numbers inside the brackets indicate the % reduction in the steady-state condensate retention caused by the drainage channels, over the baseline case

Table 3.6 Fin gap and louver gap for all fin designs[26]

Fin Design	*Louver Gap (L_g)*	*Fin Gap ($F_{p,eff}$)*
1	0.96	0.58
2	0.50	0.6
3	0.66	0.54
4	0.66	0.59

[26] All dimensions are in mm

Chapter 4- IMPLEMENTATION OF DRAINAGE CHANNELS IN FULL-SIZE HEAT EXCHANGERS

In the previous chapter, it was reported that the drainage channels have the capacity to reduce the steady-state condensate retention by up to around 30%. Now, how this effect in the condensate retention translates into an effect in the heat transfer performance and the pressure drop characteristics becomes an important issue to analyze. In this chapter, modeling a louver-fin heat exchanger with drainage channels incorporated into it is undertaken. The first section of this chapter explains a simple heat exchanger design with drainage channels on a given fin design, with the maximum effect of drainage channels on condensate retention. The next section explains the modeling of heat transfer and pressure drop, based on the simple suggested design of louver-fin flat-tube heat exchanger. The obtained results are then discussed, focusing on comparison between the channeled and the non-channeled sample and the corresponding effect on the heat transfer and the pressure drop characteristics.

4.1 Implementing Drainage Channels: Sample Design

A sample design for making full-size heat exchangers with drainage channels is suggested, and it was actually manufactured so as to assess the corresponding constraints. The drainage channel-fin design combination with the maximum effect of drainage channels on the condensate retention was selected. As can be seen in Table 3.2, two vertical square channels engraved on the side walls provided the maximum reduction in steady-state retention for fin design 3, and hence that combination was selected for analysis.

Due to the small thickness of the commonly available flat tubes for louver-fin heat exchangers, engraving a 1-mm-deep square channel on the flat tubes was not feasible. The channels were

fabricated on the flat tube by adhering aluminum plates onto the thin tubes on both sides (Figure 4.1). The figure shows the channeled and the non-channeled sample for comparison. Thermal epoxy with the highest thermal conductivity available was used (Arctic Silver thermal adhesive, k=7.0 W/m-K). The additional thermal resistance due to the epoxy was taken into account in the thermal calculations. The fin stock was then attached to the aluminum plates. Small exchangers with 4-5 flat tubes were manufactured. The overall justification of using fin Design 3 with square channels can be provided as:

- 2 square channels used with Design 3 gave the maximum reduction in retention in the condensation tests (~30%).
- Square channels are the easiest to be incorporated in the exchanger design, using the present method of adhering flat aluminum plates to the flat tubes (Figure 4.1).

Complete heat exchanger assembly is shown in Figure 4.2

4.2 Heat Transfer and Pressure Drop Estimation

Modeling for heat transfer and pressure drop was performed to assess the effect of drainage channels on heat transfer and pressure drop characteristics. The complete problem was formulated and solved using EES (Engineering Equation Solver). The inputs required by the program were the inlet conditions (temperature, inlet relative humidity, and pressure, air velocity, and heat exchanger geometrical specifications). The program gave the exit conditions, the heat transfer and its sensible and latent components, pressure drop across the heat exchanger, all quantities obtained for both the channeled and the non-channeled cases. This section describes in general the calculation/estimation strategy and the corresponding results. Details on the EES program and the equations used can be found in Appendix-C.

4.2.1 Calculation Methodology

The calculation methodology consisted of estimating the air-side heat transfer coefficient from a correlation for the Colburn *j*- factor, then calculating the coolant side and the air side thermal resistance followed by performing a mass transfer and heat transfer analysis across the heat exchanger to evaluate the heat transfer and the exit conditions of the moist air and the coolant. Similarly for the pressure drop, a correlation for the fanning friction *f*- factor was used. The fin geometries analyzed were fin design 1, 3 and 4. The calculations were performed both for the channeled and the non-channeled case, with the assumption that the heat exchanger is completely wet without the drainage channels.

Correlations developed by Park and Jacobi [31] were used to estimate the Colburn *j*-factor and the friction *f*- factor for louver fin heat exchangers. The correlations are the latest and cover a wide design space. The correlations used are of the simplified form,

$$j, f = function(operating\ conditions, fin\ geometrical\ parameters) \quad (4.1)$$

Thus, given the operating conditions of air temperature, relative humidity, pressure, air flow rate, and the fin geometrical specifications (fin spacing, louver spacing, etc.), the value for the factors can be evaluated. Once the *j*- factor was calculated, the concept of wet-surface multipliers was used to evaluate the properties under completely wet conditions. The wet-surface multipliers define a method to evaluate the heat transfer rate when the exchanger is fully wet. The multipliers are calculated using a similar form of equation used to calculate the *j*-and the *f*-factors, i.e. Eq. (4.1). The factors under the wet conditions are then given by,

$$j_{wet} = j \times \varphi_j \quad (4.2)$$

and a similar relation for the friction factor.

To account for the effect of drainage channels, the reduction in the steady state condensate mass retention using drainage channels was directly related to the wetness of the surface. A simple approximation using a weighted mean to evaluate the j and f factor for the channeled samples was used,

$$j_{channeled} = 0.3 \times j_{dry} + 0.7 \times j_{wet} \tag{4.3}$$

Once the factors are determined, the heat transfer coefficient was calculated. With wet surface fin efficiency taken into account, the air side thermal resistance was calculated.

The coolant side thermal resistance was calculated assuming the flow inside the tubes is hydro-dynamically developed and thermally developing. Specific relation between the Nusselt number and the fluid properties for constant heat flux on the tube walls was used to evaluate the liquid side heat transfer coefficient and the corresponding liquid-side thermal resistance. The fluid used for the calculation was ethylene glycol solution (53.6% by weight). The thermodynamic properties for the fluid are evaluated as function of temperature from the developed correlations. Finally the thermal resistance due to the epoxy used to attach the flat tubes to the fin stock and the conductive resistance was added to the coolant and the air resistance, to obtain the overall heat transfer coefficient. The overall heat transfer coefficient was used to calculate the number of transfer units (NTU), and in turn to estimate the effectiveness (ε) to determine the sensible component of heat transfer.

Mass transfer analysis using the mass driving potential method was undertaken to calculate the change in the absolute humidity of the air crossing the heat exchanger, and hence determine the

latent component of heat transfer. On the other hand, a relation between the friction factor and the pressure drop given by Kays and London [14] was used to calculate the pressure drop for the channeled and non-channeled cases. All the equations were solved in an iterative manner using EES. More detail about the equations used and the EES program are provided in Appendix-C.

The calculations performed here are for the suggested heat exchanger design, which involves resistance caused by epoxy used to hold together the plates. However, the exchangers could also be manufactured by brazing, and hence that resistance could be removed. Also, the fluid considered is ethylene glycol[27], which has higher thermal resistance than the refrigerants. So under actual operating conditions with higher fraction of the thermal resistance due to the air-side than the present case, the effect of drainage channels will be larger than what is obtained in these calculations.

4.2.2 Effect of Drainage Channels on Heat Transfer Performance

Using the method described above, the heat transfer rate and its latent and sensible components were evaluated for the channeled and the baseline case. To find the maximum effect of drainage channels on the heat transfer performance, the maximum reduction in the condensate retention caused by the drainage channels was considered (~30%). The effect of drainage channels on the heat transfer was evaluated at different inlet operating conditions of air temperature, velocity and relative humidity.

The change in the total heat transfer rate expressed as a percentage change by the use of drainage channels with varying Reynolds number based on the louver spacing is shown in Figure 4.3. The results shown are for heat exchanger consisting of fin Design 3, and the size of the heat

[27] The calculations were performed modeling an experiment in the lab, where only ethylene glycol could be used.

exchanger fixed at a value within the limits of actual size of automotive evaporators to obtain the maximum effect of drainage channels. From the figure, it is clear that the increase in total heat transfer which is maximum at the lowest Reynolds number (~12.0%), decreases with increasing Reynolds number, indicating a strong dependence on the incoming air velocity. This is in accordance with the previous research findings [13] that with increasing air velocity, the effect of retained condensate on the heat transfer performance decreases. Furthermore, it was also observed in real-time retention tests, that the air velocity also has a significant effect on the condensate retention. Hence, incoming air velocity becomes an important factor in the heat exchanger design.

The variation of change in heat transfer rate with varying inlet air temperature for fin design 3 is not significant. The change in the heat transfer rate varies from 11.3% at 30 ^{0}C air inlet temperature to only 11.5% at 40 ^{0} C air temperature. The variation with the inlet relative humidity is shown in Figure 4.4. With increasing inlet relative humidity, the difference in the heat transfer rate caused by drainage channels increases. Again, the variation is small.

It is interesting to compare the latent and the sensible heat transfer with the use of drainage channels. The latent and the sensible components of heat transfer rates with and without the use of drainage channels, with increasing relative humidity is shown in Figure 4.5. As can be seen from the figure, at lower humidity drainage channels cause an increase in both the components. However, the increase in the latent component is more than for the sensible component. With increasing relative humidity of the incoming air, the latent component increases and the sensible component decreases. The difference caused by the drainage channels increase more for the latent component, and surprisingly becomes lower for the sensible component. Interestingly, beyond a certain humidity, the change in the heat transfer coefficient caused by the drainage

channels does not have any effect on the sensible heat transfer. All the increase in the heat transfer comes from the latent component. The variation of change in heat transfer rate caused by drainage channels with varying inlet mass flow rate of coolant is shown in Figure 4.6. With increasing coolant mass flow rate, the change caused by the channels on the heat transfer performance increases. It rises from 10.9% to 11.7 % if the mass flow rate is changed from 0.05 kg/sec to 0.1 kg/sec. The main reason behind this increase can be linked to the decrease in the coolant side thermal resistance with increase in the mass flow arte. As the mass flow rate of the coolant increases, the coolant side heat transfer coefficient increases, and the thermal resistance decreases. Thus, the contribution of the coolant resistance to the overall resistance decreases with increasing mass flow rate of the coolant. As the drainage channels only cause a change in the air side thermal resistance, and with increasing mass flow rate of the coolant, the relative contribution of the air side resistance on the overall resistance increases, thus magnifying the effect of drainage channels.

All the parameters like air velocity, inlet mass flow rate of coolant, inlet relative humidity and inlet temperatures were varied and the optimum ones (inside the range of variation) were selected to calculate the maximum change in the heat transfer rates obtainable through the use of drainage channels. The comparison of percentage increase in the heat transfer rate caused by the drainage channels on the heat exchangers is shown in Figure 4.7. The heat exchanger sample considered for all the fin designs had the similar air transfer area, so as to keep the comparison reasonable. As is clear from the figure, the change caused by the drainage channels is maximum for Design 3, followed by Design 2 and Design 1. Design1 had a very different percentage change caused because of large difference in the fin geometry as compared to the other two fin designs. Finally, the operating conditions used for calculating the maximum obtainable

difference with the drainage channels, again with the constraint of maintaining realistic conditions for automotive evaporative environments is summarized in Table 4.1.

4.2.3 Effect of Drainage Channels on Pressure Drop

From the estimated friction factor for a given heat exchanger geometry, the pressure drop was calculated from the relation given by Kays and London [15]. Pressure drop across the heat exchanger was evaluated for the channeled and the non-channeled sample. Again to find the maximum effect of drainage channels, the maximum reduction in the condensate retention was considered. The effect of drainage channels on the pressure drop was estimated for different operating conditions.

The change in the total air-side pressure drop expressed as a percentage change by the use of drainage channels with varying Reynolds number (based on the louver spacing) is shown in Figure 4.8. The results shown are for heat exchanger consisting of fin Design 3, and the size of the heat exchanger already fixed at a value, so as to obtain the maximum effect of drainage channels. The change (decrease) in the pressure drop caused by the drainage channels decreases with increasing Reynolds number, as is clear from the figure. With increasing velocity, the condensate retained does not cause much variation in the pressure drop as compared to the dry case. Hence, channels have little to act on, and thus cause less difference with increasing Reynolds number.

All parameters were varied and the optimum ones (within the range of variation) were selected to calculate the maximum change in the pressure obtainable through the use of drainage channels. The comparison of percentage increase in the pressure drop caused by the drainage channels on the heat exchanger sample made with fin Design 1, 3 and 4 is shown in Figure 4.9. Again, the

size of heat exchangers simulated has been kept same for all the designs having almost the same pressure drop. As is clear from the figure, the change is maximum for Design 3, followed by Design 2 and Design 1. Design1 had a very different percentage change caused because of large difference in the fin geometry as compared to the other two fin designs.

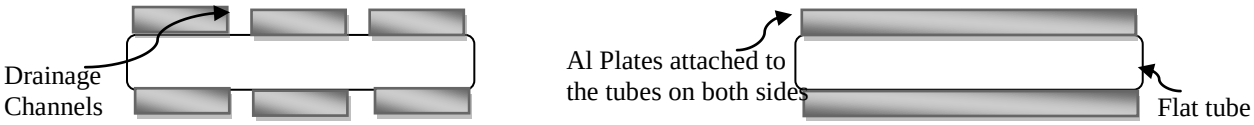


Figure 4.1 Drainage channels incorporated in full size heat exchangers

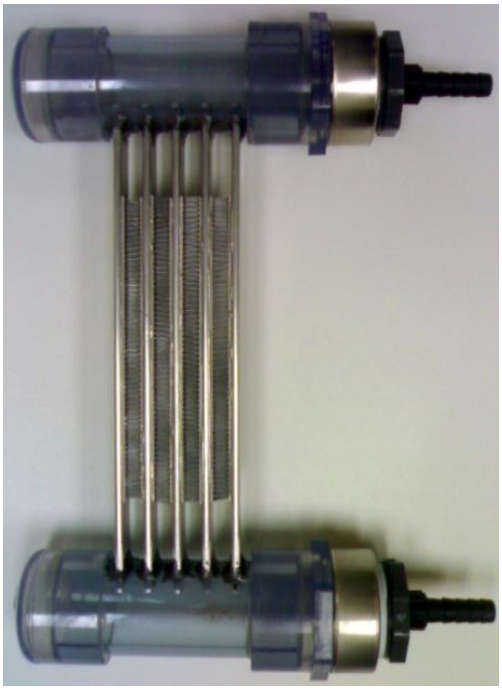


Figure 4.2 Full size heat exchanger with drainage channels: a sample design

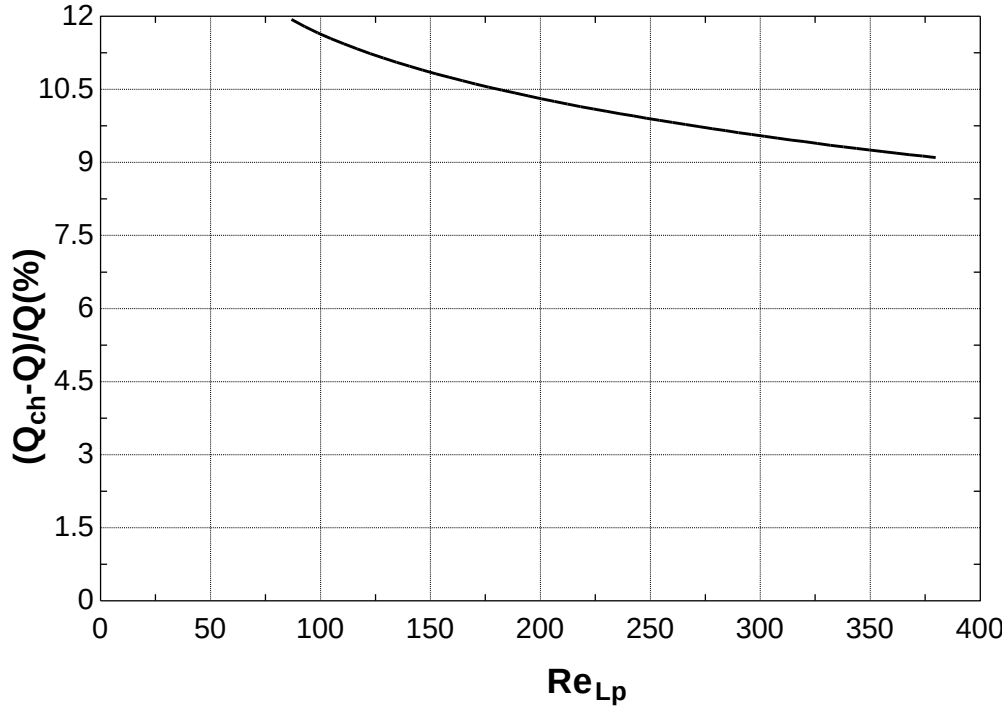


Figure 4.3 Percentage change in heat transfer rate caused by drainage channels with Reynolds number for fin Design 3

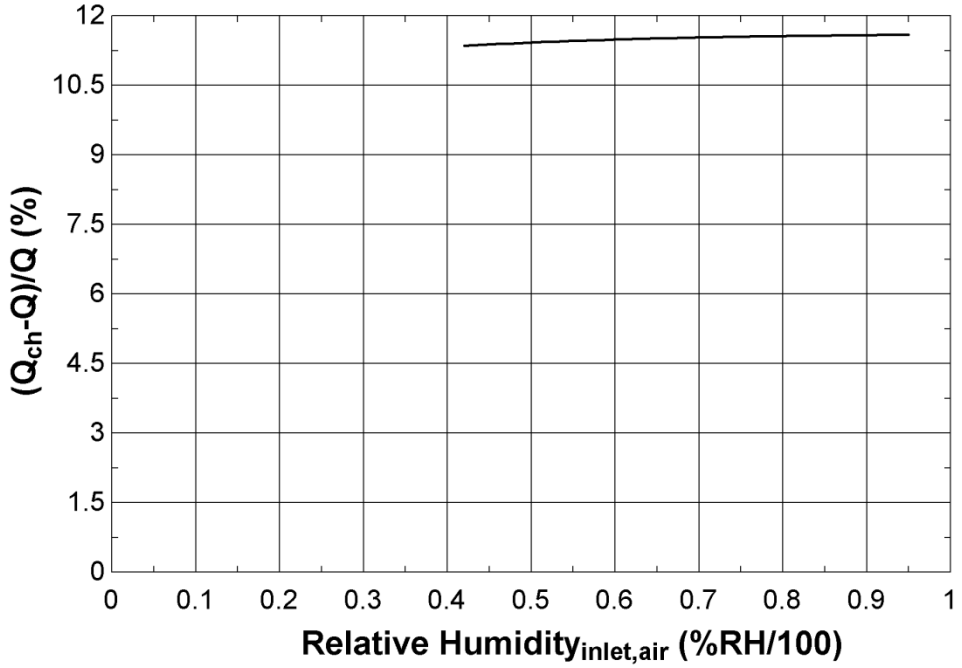


Figure 4.4 Percentage change in heat transfer rate caused by drainage channels with inlet relative humidity for fin Design 3

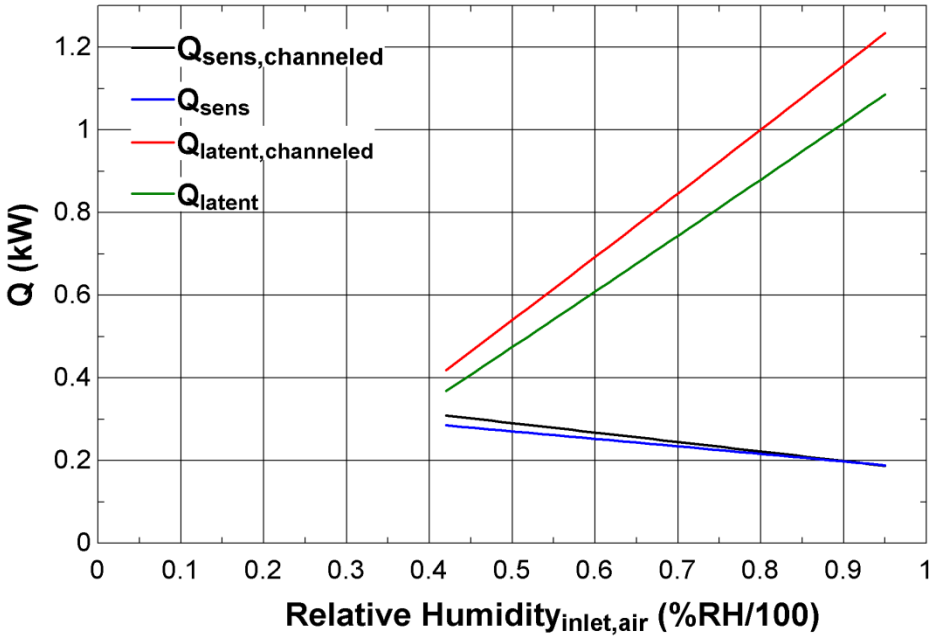


Figure 4.5 Variation in latent and sensible heat transfer rates caused by drainage channels with varying inlet relative humidity for fin Design 3

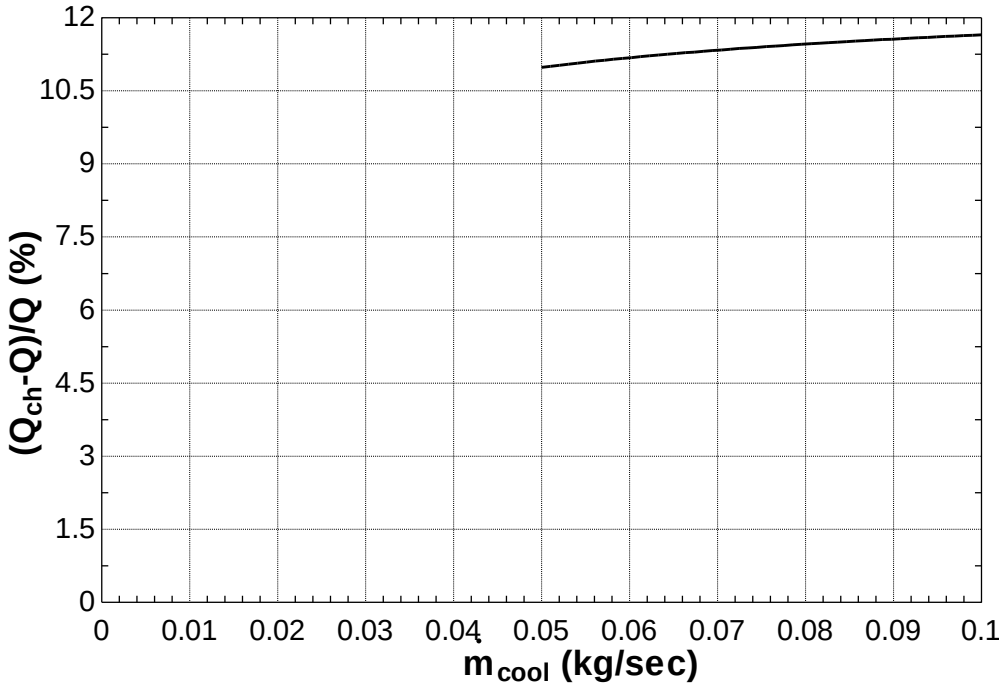


Figure 4.6 Percentage change in heat transfer rate caused by drainage channels with varying mass flow rate of coolant for fin Design 3

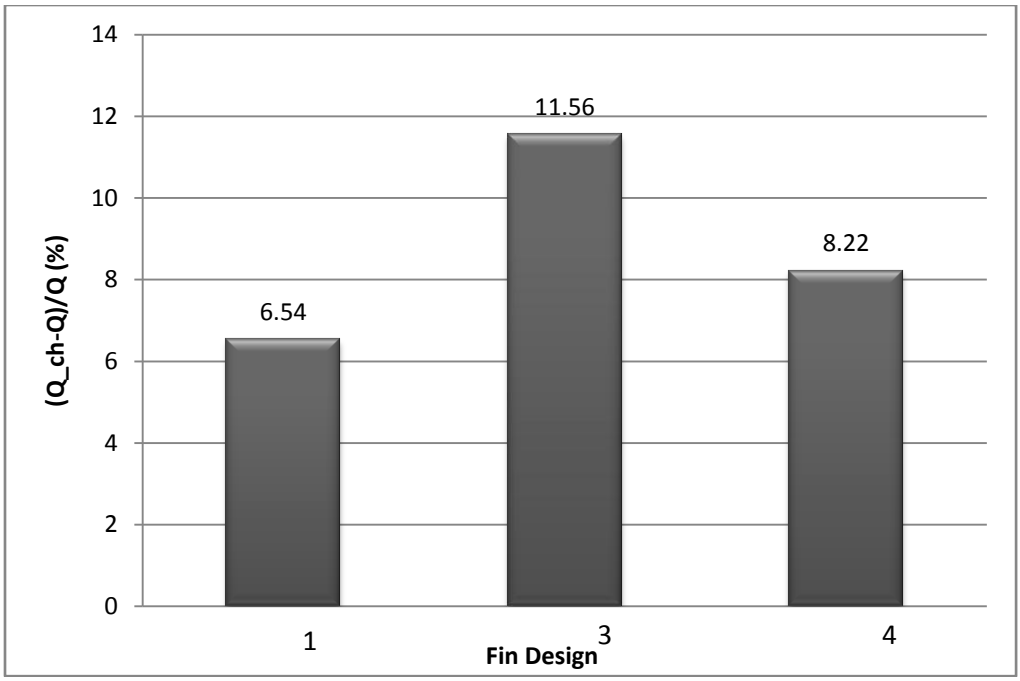


Figure 4.7 Maximum percentage change obtained in the heat transfer rates by using drainage channels with different fin designs

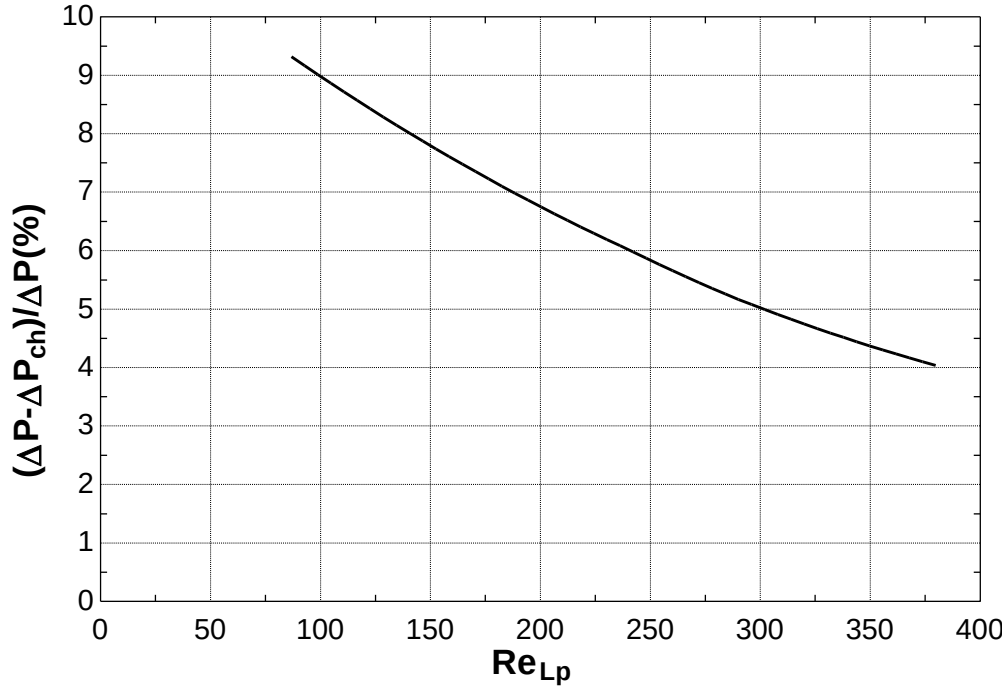


Figure 4.8 Percentage change in pressure drop caused by drainage channels with Reynolds number for fin Design 3

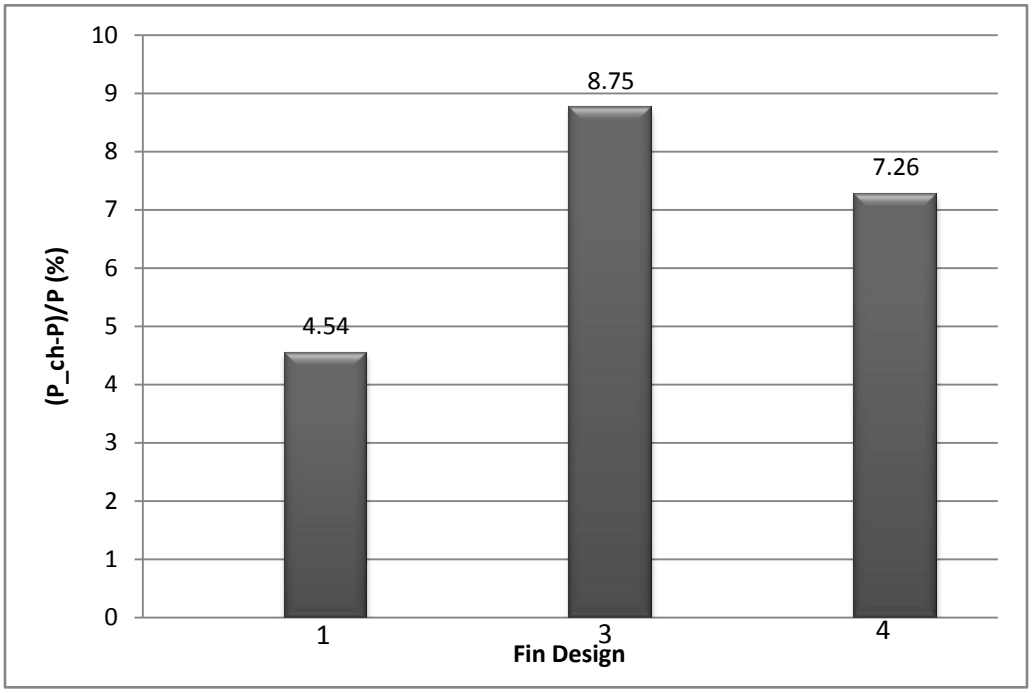


Figure 4.9 Maximum percentage change obtained in the pressure drop by using drainage channels with different fin designs

Table 4.1 Sample inlet conditions and the calculated values showing the difference in heat transfer and pressure drop through the drainage channels for a full size heat exchanger

Inlet Conditions		
V_{fr} (m/s)	1.0	
$\dot{m}_{cool}$ (kg/s)	0.09	
$T_{cool,in}$ (^{0} C)	3	
$T_{air,in}$ (^{0} C)	35	
Relative Humidity $_{air,in}$	0.8	
Calculated Parameters		
	Channeled	Non-Channeled
$T_{cool,out}$ (^{0} C)	7.4	6.9
$T_{air,out}$ (^{0} C)	33.1	33.2
Relative Humidity $_{air,out}$	0.73	0.76
$Q_{sensible}$ (KW)	0.23	0.21
Q_{latent} (KW)	1.0	0.87
LHR	0.82	0.8
Air side heat transfer coefficient, h (W/m^2-K)	86.8	73.7
ΔP (Pa)	12.6	13.7

Chapter 5- CONCLUSIONS AND RECOMMENDATIONS

Condensate retention on louver-fin flat-tube compact automotive heat exchangers and the effect of drainage channels has been investigated and analyzed in detail. Several conclusions can be drawn from the real-time and the steady-state experiments conducted during this study. Further, the condensate retention and drainage behavior has been analyzed through the visualization tests performed on a single fin. The effect of changing parameters on the drainage channel performance has been studied. The effect of drainage channels has been assessed on different fin geometries. Variations in the drainage channel geometry, location and dimension have been considered. The effect of drainage channels on full-size heat exchanger thermal-hydraulic performance was then analyzed, based on Colburn *j*- factor and friction *f*- factor correlations available for the automotive-style heat exchangers. This chapter contains general conclusions about the effects of drainage channels on the condensate retention and drainage behavior.

5.1 Dynamic Dip Testing

Dynamic dip testing was performed on a single column of louver-fin for 2 different fin geometries, and for 4 different geometries of drainage channels and total 24 combinations. The effects of fin design, channel geometry and channel dimensions on measured retention results are discussed. Some conclusions from the dynamic dip testing include:

- The two different fin designs studied had different retention and drainage behavior, with fin "bridging" causing more retention in one design than the other. The apparent "compactness" of fins usually specified by the fin and the louver spacing is not necessarily an important criteria, as the fin design (Design 1) having higher fin spacing was found to have a higher retention than the one with a smaller fin spacing. However, the fin gap, i.e., the effective distance for bridge formation for both the designs was found to be the same. Furthermore,

Design 1 exhibited the steady retention pattern while Design 2 showed the continuous drainage pattern, in spite of having lower louver and fin spacing than the former design.

- Drainage channels were found effective in decreasing the water retention for the fin Design 1, which had higher retention mass and steady retention pattern as observed in the dynamic dip tests. All types of channels tested were found ineffective for the fin Design 2, which had continuous drainage pattern.
- The triangular channel geometry provided the maximum reduction in retention, if the channels are compared with fixed width (w) at the contact with the fin. Further, for the triangular geometry, channel with 45° as the included angle and having 1 mm as width, provided the largest reduction in condensate retention. The reduction is around 40%, when the channels are used with fin Design 1.
- For the rectangular geometry, the channel with dimensions 1×1 mm provides the maximum reduction in retention. Increasing the dimension reduce the performance, as making the channel dimensions to 2×2 actually has retention equal to the baseline case.

5.2 Real-Time Condensate Retention and Visualization Experiments

Real-time condensate retention and visualization experiments were performed using a table-top wind tunnel apparatus. Four different fin designs, including the two tested in dip tests, and different channel geometries and dimensions were tested for mass retention and for analyzing condensate drainage behavior. The experiments were also performed for different operating conditions of air velocity, inlet relative humidity, and temperature. Important conclusions from the real-time mass measurements and the visualization tests can be summarized as:

- For all fin designs studied, the mass of retained condensate increased with time and reached a steady state, where the rate of condensate formation balances the rate of drainage, or a cyclic

condensate retention pattern in which a steady state value between a maximum and a minimum prevails. For fin Design 3, which had the minimum depth for air flow, the cyclic steady state was attained in the shortest time.

- Similar to the findings from the dynamic dip testing, fin Design 2 had much lower steady-state retention per unit area, as compared as to fin Design 1. Fin Design 3 and Design 4 had a similar steady state retention value to that of fin Design 1. From the visualization experiments, it was clear that the low steady state retention of Design 2 is due to its different shape (triangular, when viewing the face), which enabled a clear drainage path.
- Drainage channels are effective in decreasing the retention for all the fin designs except fin Design 2, again a finding similar to that obtained in dynamic dip testing. Channels were found to enhance drainage in the fins by pulling condensate through the louver cut end and creating new drainage paths. These drainage paths were already present for fin Design 2 without the use of drainage channels, as was observed in the visualization tests. Further, the minimum length scale for the channels used was much more than the louver gap of fin Design 2. Channels probably failed to create enough capillary pressure to pull the condensate from the louver-cut end.
- Drainage channels enhance drainage not only by pulling the condensate from the louver-cut end or by providing a clear path for drainage, but also by initiating a cascade of drainage causing the filled inter-fin regions to drain. The drainage provided by the drainage channels is usually not continuous, but takes place in steps. Thus channels promote the oscillation mode, where the steady state retention is between a maximum and a minimum limit.

- Among all drainage channel geometries examined, the triangular channel geometry provided the maximum reduction in retention with fin Design 1 (~24%), followed by the rectangular and the trapezoid geometry. The trend remains same as in the dynamic dip tests.
- For the same channel geometry, increasing the channel depth does not cause any improvement in the steady-state retention. This trend was observed with the triangular geometry when the included angle was changed to 22.5^0 from 45^0 and with the rectangular geometry when depth was increased to 2 mm from 1mm. It is an important observation from manufacturing point of view, as making deep channels on the thin flat tubes can be difficult.
- Shallow drainage channels work similar to or sometimes even better than the deeper channels, because of overfilling and spilling of the condensate on the already filled inter-fin space. This process leads to sudden movement of the settled condensate and promotes cascade of drainage to occur.
- Inclined drainage channels (45^0) to the vertical were not as effective as the vertical grooves for the same channel geometry. Further, inclination of sample without drainage channels decreased the steady-state retention and but does not affect the retention for samples with the drainage channels. This difference changes the effect of the drainage channels on the retention from 20% to only 10%, as compared to the baseline.
- Changing the inlet relative humidity only changes the initial slope of the condensate retention curve, and hence affects the time required to attain the steady state retention. The steady-state retention, however, does not change with changing humidity, as humidity has no or little effect on the drainage characteristics. For the very same reason, changing humidity also has almost no effect on performance of drainage channel.

- Changing the air velocity changes the retention and drainage characteristics and as well as the steady state retention for the non-channeled sample. Increasing the air velocity from 1.5m/s to 3.5 m/s decreases the steady state retention by 18%. However, channeled samples have no significant effect of the air velocity on the steady state retention; hence channels perform better at lower air velocities.
- The maximum reduction in the steady-state retention was obtained with 2 square channels located equispaced along the fin depth with fin Design 3 (~27%). The design had the smallest fin depth.

5.3 Heat Transfer and Pressure Drop Calculations

Heat transfer and pressure drop calculations based on the *j*- and *f*- factors correlations were performed to assess the effect of drainage channels on the overall thermal-hydraulic performance of the heat exchanger. Calculations were performed for a sample design suggested to implement the drainage channels in full size heat exchangers. The fin design for the sample was chosen as Design 3 with two square vertical drainage channels, as it had the maximum obtained reduction n the real-time condensation tests. Some of the important findings from the heat transfer and pressure drop analysis include:

- The decrease in the condensate retention caused by the drainage channels translates to an increase in the air side heat transfer coefficient and a decrease in the air side pressure drop. For the calculations performed, the channels were found to have the capacity to increase the heat transfer rate up to 11.6% and decrease the pressure drop up to 9%.
- The effect on the heat transfer and pressure drop was maximum for heat exchanger with fin Design 3, followed by fin Design 4, which had increase in heat transfer performance of 8.2%

and decrease in pressure drop of 7.3%. The smallest change was calculated for fin Design 1, which had a heat transfer increase of 6.5% and pressure drop reduction of 4.5%.

- The effect of drainage channels on the heat transfer performance and the pressure drop decreased with increasing air-side Reynolds number. On the other hand, increasing the fluid-side Reynolds number increases the effect caused by drainage channels. Further, changing the inlet air and the coolant temperatures does not have much effect on the heat transfer increase.
- Drainage channels not only cause a change in the total heat transfer and the pressure drop, but also cause a slight increase in the latent heat ratio (up to 2.5%).

5.4 Recommendations for Future Studies

There are several interesting areas where additional research could extend the present work. Some of the recommendations for future research in this area are discussed in this section.

- The present experimental work on the effectiveness of the drainage channels to reduce the condensate retention can be supplemented by a theoretical model taking into account capillary, air flow force, gravity and other related forces which govern the movement of condensate on the fin geometry. The model should also take into consideration the different louver fin geometry and the corresponding effect of drainage channels.
- Implementation of drainage channels in full-size exchangers still needs to be explored further. Though a method to incorporate drainage channels has been suggested in this work, more efficient methods can always be found to enhance the effect on the thermal-hydraulic performance.

- Experimentation of full-size heat exchangers with the drainage channels incorporated can be undertaken, in order to verify the findings of the calculations presented in this work, with respect to the change in heat transfer and pressure drop performance.
- Though many drainage channel shapes and geometries were considered in this study, some were not tested because of manufacturing constraints. More studies also can be performed with respect to the location of drainage channels in the heat exchangers. In this study, channels engraved on the flat tubes were tested. There can be ways by which channels could be incorporated in the fin design itself.
- Research could be performed in finding solutions to the problem of condensate retention in heat exchangers which involve combination of drainage channels with other condensate retention reduction techniques such as surface treatments and micro-grooves.
- In this study, the effect of drainage channels was assessed only on louver fin flat tube heat exchanger geometry. Drainage channels can also be studied with other complex fin geometries such as slit-fin heat exchangers with flat tubes. Methods to implement drainage channels in other types of heat exchangers such as plain-fin and round tube can be explored.

Bibliography

[1] Tafti D. K., Zhang X. , Huang W. , and Wang G. , "Large-Eddy Simulations of Flow and Heat Transfer in Complex Three-Dimensional Multilouvered Fins," University of Illinois at Urbana Champaign, ACRC TR-165, 2000.

[2] Simmons R. B., Rose L. J., Crow S. A., and Ahearn D. G., "The Occurence and Persistence of Mixed Bio Films in Automobile Air Conditioning Systems," *Current Microbiology*, vol. 39, pp. 141-145, 1999.

[3] Bryan W. L., "Heat and Mass Transfer in Dehumidifying Surface Coils," *ASHRAE Transactions*, vol. 67, pp. 393-405, 1961.

[4] Bryan W. L., "Heat and Mass Transfer in Dehumidying Extended Surface Coils," *ASHRAE Transactions*, vol. 68, pp. 237-247, 1962.

[5] Bettanini E. , "Simultaneous Heat and Mass Transfer on a Vertical Surface," *International Institute of Refrigeration Bulletin*, vol. 70, pp. 309-317, 1970.

[6] Yoshii T. , Yamamoto M. , and Otaki T. , "Effects of Dropwise Condensate on Wet Surface Heat Transfer of Air Cooling Coils," in *Proc. 13th Int. Congress of Refrigeration*, 1973, pp. 285-292.

[7] Guillory J. L. and McQuiston F. C., "An Experiemental Investigation of Air Dehumidification in a Parallel Plate Heat Exchanger," *ASHRAE Transactions*, vol. 79, no. 2, pp. 146-151, 1973.

[8] McQuiston F. C., "Heat, Mass and Momentum Transfer in a Parallel Plate Dehumidifying Exchanger," *ASHRAE Transactions*, vol. 82, no. 2, pp. 87-107, 1976.

[9] Tree D. and Helmer W. , "Experimental Heat and Mass Transfer Data for Condensing Flow in a Parallel Plate Heat Exchanger," *ASHRAE Transactions*, vol. 82, no. 1, pp. 289-299, 1976.

[10] Jacobi A. M. and Goldschmidt V. W., "Low Reynolds Number Heat and Mass Transfer Measurements of an Overall Counterflow, Baffled, Finned-Tube, Condensing Heat Exchanger," *International Journal of Heat and Mass Transfer* , vol. 33, pp. 755-765, 1990.

[11] Korte C. M. and Jacobi A. M., "Condensate Retention and Shedding Effects on Air-Side Heat Exchanger Performance," University of Illinois at Urbana Champaign, ACRC TR-132, 1997.

[12] Yin J. and Jacobi A. M., "Condensate Retention Effects on the Air-Side Heat Transfer Performance of Plain and Wavy-Louvered Heat Exchangers," University of Illinois at Urbana-Champaign, ACRC TR-158, 2000.

[13] Kim G. J. and Jacobi A. M., "Condensate Accumulation Effects on the Air-Side Thermal Performance of Slit-Fin Surfaces," University of Illinois at Urbana-Champaign, ACRC CR-26, 2000.

[14] Kays W. M. and London A. L., "Heat Transfer and Flow Friction Characteristics of Some Compact Heat Exchanger Surfaces," *ASME Transactions*, vol. 72, pp. 1075-1085, 1950.

[15] Kays W. M. and London A. L., *Compact Heat Exchangers*, 2nd ed. New York: McGraw-Hill, 1984.

[16] Beauvais F. N., "An Aerodynamic Look at Automobile Radiators," *SAE*, no. 650470, 1965.

[17] Davenport C. J., "Correlation for Heat Transfer and Flow Friction for Heat Transfer and Flow Friction Characteristics of Louver Fin," in *AIChE Symposium Series*, vol. 79, Seattle, 1983, pp. 19-27.

[18] Davenport C. J., "Heat Transfer and Flow Friction Characteristics of Louvered Heat Exchanger Surfaces ," in *Heat Exchangers: Theory and Practice*. Washington D.C.: Hemisphere, 1983, pp. 397-412.

[19] Kajino M. and Hiramatsu M. , "Research and Development of Automotive Heat Exchangers," in *Heat Transfer in High Technology and Power Engineering*. Washington D.C.: Hemisphere Publishing Corp., 1987, pp. 420-432.

[20] Achaichia A. and Cowell T. A., "Heat Transfer and Pressure Drop Characteristics of Flat Tube and Louvered Plate Fin Surfaces," *Experimental Thermal and Fluid Science*, vol. 1, pp. 147-157, 1988.

[21] Achaichia A. and Cowell T. A., "A Finite Difference Analysis of Fully Developed Periodic Laminar Flow in Inclined Louvered Arrays," in *Proceedings of 2nd UK National Heat Transfer Conference*, vol. 2, Glasgow, 1988, pp. 883-888.

[22] Webb R. L. and Trauger P. , "The Flow Structure in the Louver Fin Heat Exchanger Geometry," *Experiemental Thermal and Fluid Science*, vol. 4, pp. 205-217, 1991.

[23] Webb R. L. and Jung S. H., "Air Side Performance of Enhanced Brazed Aluminum Heat Exchnagers," *ASHRAE Transactions*, vol. 98, no. 2, pp. 391-401, 1992.

[24] Suga T. and Aoki H. , "Numerical Study on Heat Transfer and Pressure Drop in Multilouvered Fins," in *Proceedings of the 1991 ASME/JSME Joint Thermal Engineering Conference*, vol. 4, 1991, pp. 361-368.

[25] Cui J. and Tafti D. K., "Computations of Flow and Heat Transfer in a Three-Dimensional Multilouvered Array Fin Geometry," *Int J Heat Mass Transfer*, vol. 45, pp. 5007-5023, 2002.

[26] Kim J. H., Yun J. H., and Lee C. S., "Heat Transfer and Friction Characteristics for the Louver-Fin Heat Exchanger," *J. ThermoPhysics Heat Transfer*, vol. 18, no. 1, pp. 58-64, 2004.

[27] Chang Y. J. and Wang C. C., "A Generalized Heat Transfer Correlation Louver Fin Geometry," *Int J Heat Mass Transfer*, vol. 40, no. 3, pp. 533-544, 1997.

[28] Chang Y. , Wang C. , and Chang W. , "Heat Transfer and Flow Characteristics of Automotive Brazed Aluminum Heat Exchangers," *ASHRAE Transactions*, vol. 100, no. 2, pp. 643-652, 1994.

[29] Kim M. H. and Bullard C. W., "Air-Side Thermal Hydraulic Performance of Multi-Louvered Fin Aluminum Heat Exchangers," *Int J Refrigeration*, vol. 25, no. 3, pp. 390-400, 2002.

[30] Dong J. , Chen J. , Chen Z. , Zhang W. , and Zhou Y. , "Heat Transfer and Pressure Drop Correlations for the Multi-Louvered Fin Compact Heat Exchangers," *Energy Conversion and Management*, vol. 48, pp. 1506-1515, January 2007.

[31] Park Y. G. and Jacobi A. M., "Air-Side Heat Transfer and Friction Correlations for Flat-Tube Louver-Fin Heat Exchangers," *ASME Journal of Heat Transfer*, vol. 131, no. 2, p. 021801, February 2009.

[32] Wang C. C.et al., "Experimental Study of Heat Transfer Characteristics of Automotive Evaporators," *ASHRAE Transactions*, vol. 100, no. 2, pp. 575-582, 1994.

[33] McQuiston F. C., "Fin Efficiency with Combined Heat and Mass Transfer," *ASHRAE Transactions*, vol. 81, pp. 350-355, 1975.

[34] Osada H. , Aoki H. , Ohara T. , and Kuroyanagi I. , "Research on Corrugated Multi-Louvered Fins under Dehumidification," *Heat Transfer- Asian Research*, vol. 30, no. 5, pp. 383-393, 2001.

[35] Kim M. H., Youn B. , and Bullard C. W., "Effect of Inclination on the Air-Side Performance of a Brazed Aluminum Heat Exchanger under Dry and Wet Conditions," *International Journal of Heat and Mass Transfer*, vol. 44, no. 24, pp. 4613-4623, 2001.

[36] Mclaughlin W. J. and Webb R. L., "Condensate Drainage and Retention in Louver Fin Automotive Evaporators," in *Proceedings of the SAE International Congress*, Detroit, 2000.

[37] Mclaughlin W. J. and Webb R. L., "Wet Air Side Performance of a Louver Fin Automotive Evaporator," in *Proceedings of the SAE International Congress*, Detroit, MI, 2000.

[38] Kaiser J. M. and Jacobi A. M., "Condensate Retention Efects on the Air-Side Heat Transfer Performance of Automotive Evaporator Coils," University of Illinois at Urbana-Champaign, ACRC CR-32, 2000.

[39] Tang A. D. and Jacobi A. M., "Air Side Heat Transfer with Highly Interrupted Surfaces: An Experimental Study of Condensate Retention Effects," University of Illlinois at Urbana-Champaign, ACRC TR-185, 2001.

[40] Kim M. H. and Bullard C. W., "Air-Side Performance of Brazed Aluminum heat Exchangers Under Dehumidifying Conditions," *International Journal of Refrigeration*, vol. 25, no. 7, pp. 924-934, 2002.

[41] Park Y. and Jacobi A. M., "The Air-Side Thermal-Hydraulic Performance of Flat-Tube Heat Exchangers With Louvered, Wavy, and Plain Fins Under Dry and Wet Conditions," *ASME Journal of Heat Transfer*, vol. 131, p. 061801, 2009.

[42] Sommers A. D. and Jacobi A. M., "Using Anisotropic Micro-Scale Topography to Manipulate the Wettability of Aluminum and Reduce The Retention of Water," University of Illinois at Urbana-Champaign, Urbana, IL, ACRC TR-260, 2007.

[43] Liu Liping , Jacobi A. M., and Chvedov Dmitri , "A Surface Embossing Technique to Create Micro-Grooves on an Aluminum Fin Stock for Drainage Enhancement," *Journal of Micromechanics and Microengineering*, vol. 19, p. 035026, 2009.

[44] Goodremote C. E. and Hartfield J. P., "The Effect of a Hydrophilic Surface on the Performance of a Serpentine Automotive Air Conditioning Evaporator," *SAE Technical Paper Series*, no. 850036, 1985.

[45] Fu W. L., Wang C. C., Chang W. R., and Chang C. T., "Effect of Anti Corrosion Coating on the Thermal Characteristics of Louvered Finned Tube Heat Exchangers under Dehumidifying Conditions," *Advances in Enhanced Heat/Mass Transfer and Energy Efficiency*, vol. 320, pp. 75-81, 1995.

[46] Hong K. and Webb R. L., "Performance of Dehumidifying Heat Exchangers With and Without Wetting Coatings," *J. Heat Transfer* , vol. 121, no. 4, p. 1018, 1999.

[47] Hong K. , "Fundamental Characteristics of Dehumidifying Heat Exchangers With and Without Wetting Coatings," Pennsylvania State University, PA, PhD Thesis 1997.

[48] Ha S. , Kim C. , Ahn S. , and Dreitser G. A., "Hydraulic Performance of Wet-Fin-and-Tube Heat Exchanger for Various Wettability Surfaces," in *Proceedings of the International Conference on Compact heat Exchangers and Enhancement Technology for the Process Industries*, 1999, pp. 463-470.

[49] Wang C. C. and Chang C. T., "Heat and Mass Transfer for Plate Fin and Tube Exchangers, With and Without Hydrophilic Coating," *International Journal of Heat and Mass Transfer*, vol. 41, pp. 3109-3120, 1998.

[50] Jacobi A. M., Park Y. G., Zhong Y. , Michna G. , and Xia Y. , "High Performance Heat Exchangers for Air-Conditioning and Refrigeration Applications (Non-Circular Tubes)," University of Illinois at Urbana Champaign, ARTI final report, 2005.

[51] Zhong Y. , Joardar A. , Gu Z. , Park Y. G., and Jacobi A. M., "Dynamic Dip Testing as a Method to Assess the Condensate Drainage Behavior from the Air-side Surface of Compact Heat Exchangers," *Experimental Thermal and Fluid Science*, vol. 29, pp. 957-970, 2003.

[52] Liu L. and Jacobi A. M., "Issues Affecting the Reliability of Dynamic Dip Testing as a Method to Assess the Condensate Drainage Behavior from the Air-side Surface of Dehumidifying Heat Exchangers," *Experimental Thermal and Fluid Science*, vol. 32, pp. 1512-1522, 2008.

[53] Dieck R. H., *Measurement Uncertainty: Methods and Applications*, 4th ed. NC, USA: The Instrumentation, Systems and Automation Society, 2006, ch. 3, pp. 39-62.

[54] Mills A. F., *Heat Transfer*, 2nd ed. Concord: Irwin, 1992.

[55] Xia Yanping and Jacobi Anthony M., "Air-side Data Interpretation and Performance Analysis for Heat Exchnagers with Simultaneous Heat and Mass Transfer: Wet and Frosted Surfaces," *International Journal of Heat and Mass Transfer*, vol. 48, pp. 5089-5102, October 2005.

[56] Incropera F. P. and DeWitt D. P., *Fundamentals of Heat and Mass Transfer*, 4th ed. New York: Wiley, 1996.

[57] Lienhard IV John H. and Lienhard V John H., *A Heat Transfer Textbook*, 3rd ed. Cambridge: Phlogiston Press, 2006.

Appendix A- Calculation of Air Side Area

Total air-side area (i.e., the total area exposed to air for heat transfer) for a heat exchanger is an important quantity which can be used to standardize the estimation and comparison of data like mass retained for different fin designs. Calculation of the total air-side area becomes complex with the increasing complexity of the fin design. Thus, for automotive-style louver fins, which are highly complex in geometry and design, this calculation is tedious and requires the use of various parameters. In the present set of experiments, total air-side area was used to define the mass of condensate/water retained per unit area by different fin designs and has been used for the comparison. (Refer Figure 3.1 and Figure 3.12)

For a full-size heat exchanger, total air side area is the summation of the total fin and the tube areas, i.e.,

$$A_{total} = A_{fin} + A_{tube} \tag{A.1}$$

And the total fin area can be given in terms of total no. of fins and fin single side area, as

$$A_{fin} = N_f \times A_{fin,single} \times 2 \tag{A.2}$$

Also the fin single side are can further be expressed in terms of fin width and the air flow depth, as,

$$A_{fin,single} = D \times F_w \tag{A.3}$$

The total number of fins can be obtained by dividing the core height by the fin spacing,

$$N_f = \frac{H}{F_p} \tag{A.4}$$

Similarly, the tube area can be expressed in terms of tube single side area as,

$$A_{tube} = A_{tube,single} \times 2 \tag{A.5}$$

The evaluation of tube single-side area takes into account the fin tube interaction, and is given in terms of other geometrical parameters including the fin depth and spacing, as,

$$A_{tube,single} = H \times D \times \left\{1 - \left(\frac{\delta}{F_p}\right)\right\} \qquad (A.6)$$

Equations (A.1) to (A.6) give the major component of the total air side area. There are however, other smaller components of area which are usually neglected in calculations. However, for the sake of closure, the equations used for the minor area component calculations are shown here.

The fin front and back side area is given as,

$$A_{fin,fb} = N_f \times \delta \times F_w \times 2 \qquad (A.7)$$

Similarly, the tube front and back side area,

$$A_{tube,fb} = d_t \times H \times 2 \qquad (A.8)$$

The tube minor diameter is then given by,

$$d_t = t_p - F_w \qquad (A.9)$$

Finally, total air side area including the minor and major components and important geometrical parameters for all the four fin designs tested, have been shown in Table A.1.

Table A.1 Total air side area calculations for all fin designs[2829]

	Design 1	*Design 2*	*Design 3*	*Design 4*
No. of fins (N_f)	66	92	85	80
Fin Single Side Area ($A_{fin,single}$)	315.4	282.2	128	364.5
Total Fin Area (A_{fin})	41632.8	51924.8	22032	58320
Total Tube Area (A_{tube})	6503.96	7199.12	2984.3	4196.25
Other Minor Area	262.94	200.19	249.6	282.2
Total Air Side Area	48399.7	59324.1	25265.9	62798.5

[2828] All dimensions are in mm^2

[29] The calculations are shown for a sample core height of 101.5 mm used in the small wind tunnel tests

Appendix B- Uncertainty Analysis

Uncertainty analysis is presented in this Appendix for the experimental data. The uncertainties in the measurement of mass of retained water through the dynamic dip tests are presented first, followed by the uncertainty analysis of the contact angle measurements, and then the uncertainty associated with the real-time condensate retention measurements.

B.1 Dynamic Dip Tests

The dynamic dip tests were conducted on a much smaller sample as compared to samples previously tested using the technique. Thus, the chances of random errors were much more than the bias error, which is only associated with the accuracy of the electronic balance used for the measurement.

To calculate the overall uncertainty in measurement of a variable (mass, for the present case), both bias (system) and random errors have been taken into account. [53]

- Bias (Systematic uncertainty),

  B=b/2=0.1/2 g (uncertainty in the balance used-Sartorius GP-8201)

- Random uncertainty,

$$S_{\bar{x}} = {S_x}/{\sqrt{N}} \tag{B.1}$$

where,

S_x= standard deviation of the given dataset,

The dataset is obtained by taking the mean of last minute readings for each dip test.

N = number of data points taken

Total number of dip tests done on a given sample=20, so as to make the value of student's t-distribution to be close to 2. One data point was obtained from each test by taking the last minute readings.

To obtain 95% confidence bounds on the mean, we use the following relation for overall uncertainty:

$$U_{95} = \pm t_{95}\left(B^2 + S_{\bar{X}}{}^2\right)^{1/2} \quad \text{(B.2)}$$

where,

t_{95} is the coefficient for student's t-distribution obtained from tables, for a given degree of freedom and then the estimated mean is bound by ,

$$\mu - U_{95} \leq \mu \leq \mu + U_{95} \quad \text{(B.3)}$$

A sample calculation is provided here for the baseline case for fin Design 1.

Mean of the sample (mean of the 20 tests obtained by taking the mean of the last minute reading of each tests),

$\bar{X}$= 16.67 g

Standard deviation of sample mean,

S_x= 0.523 g

Standard deviation of the population, (random uncertainty)

$S_{\bar{x}} = {S_x}/{\sqrt{N}}$ = 0.523/sqrt (20)=0.117 g

Coefficient for t-distribution for N=20 readings (i.e., N-1=19 degrees of freedom)

t_{95}=2.093

Bias in the instruments, b=0.1g,

Therefore, Bias uncertainty= B=b/2=0.05g

Overall uncertainty,

$U_{95} = \pm t_{95}\left(B^2 + S_{\bar{X}}{}^2\right)^{1/2} = \pm 2.093(0.05^2 + 0.117^2)^{1/2}$ =0.2664 g

Relative Uncertainty, $U_{95}/\bar{X}$ % = 1.6 %

Uncertainty bounds for estimated mean,

$$16.67 - 0.2664 \leq \mu \leq 16.67 + 0.2664$$

$$16.41 \leq \mu \leq 16.94$$

Therefore, the estimated mean for the baseline case for Design 1 lies between 16.4 g and 16.9 g with 95% confidence.

The total uncertainties for all the test cases have been calculated, and shown in Tabular form, in Table B.1. The uncertainties are in the range 1.5-4% of the measurements. It is clear that the uncertainties in the experimental measurement are smaller than the mass of condensate reduced by using the channels (Refer Table 3.1). Hence the reduction obtained from the drainage channels is more than the 95% confidence interval of the measurements. Table B.2 shows uncertainties in the measurement of the steady state retained condensate for Design 2 samples. It can be seen that the experimental uncertainties are much more than the actual difference obtained from using the channels on this fin design.

B.2 Contact Angle Measurements

As discussed previously in Chapter-2, the measurement of contact angle was done using the sessile drop measurement test. A micro-syringe was used to put the required volume of distilled water onto the surface to form a droplet. A photograph using a CCD camera was taken, and then the contact angles were manually measured. (Refer Figure 3.10) The random uncertainties were thus only present, and systematic uncertainties, if at all present, were neglected. The

measurements were done on droplets of 5 sizes- from 5 µl to 25 µl. For each droplet volume, 2 droplets were measured with 3 measurements of contact angle on each side of the droplet. Thus, summing to 12 readings for each droplet volume. Finally, the average value of the contact angles measured at the two sides (3 readings each) were taken, and thus 4 values (2 for each drop) for each droplet volume were taken for the uncertainty analysis of the measurement. Hence, 20 readings were used to calculate the uncertainty associated with a measurement.

Equations B.1, B.2 and B.3 were used, with the bias error as zero. Table B.3 shows the mean value of the contact angle measured at three different conditions of the fin surface, with the associated uncertainties. The uncertainties are high in this case, because of a large possibility of human error, variation of surface profile and photographic errors.

B.3 Small Wind Tunnel Tests

The quantitative measurements taken on the table top wind tunnel apparatus comprised of many measurements taken together to maintain the state of the system to ultimately measure the retained condensate. The measured mass is then sensitive to changes in different variables, which must be accounted in the uncertainty analysis.

Sensitivity is the instantaneous rate of change in a result to a change in a parameter. The result here if the measured mass and the parameters may be the air velocity, air humidity, and fin temperature. For a measured result R, which is function of different parameters, we have, if

$$R = f(\bar{X}_1, \bar{X}_2, \ldots\ldots, \bar{X}_I) \qquad (B.4)$$

Then,

$$\theta_i = \frac{\partial R}{\partial \bar{X}_1} \qquad (B.5)$$

where θ_i is the absolute sensitivity coefficient of the parameter on the result. The quantity is evaluated experimentally, by varying the parameter, keeping the other parameters constant, and analyzing the effect on the final result. A linear fit was obtained and the slope of the graph between the result and the parameter was taken to be the sensitivity of that parameter.

Further, the absolute random standard uncertainty of a single test result can be determined from the propagation equation as,

$$S_R = \left[\sum_{i=1}^{I} \left(\theta_i S_{\bar{X}_i}\right)^2\right]^{\frac{1}{2}} \qquad (B.6)$$

where, $S_{\bar{X}_i}$ is the standard random uncertainty associated with a single parameter.

Similarly, the absolute systematic standard uncertainty of a result can be determined from,

$$B_R = \left[\sum_{i=1}^{I} \left(\theta_i B_{\bar{X}_i}\right)^2\right]^{\frac{1}{2}} \qquad (B.6)$$

where, $B_{\bar{X}_i}$ is the standard systematic uncertainty associated with a single parameter.

Finally, the general form of expression for determining the combined standard uncertainty of a result is the root-sum-square of both the systematic and random standard uncertainty of the result. We have,

$$U_R = \left(B_R{}^2 + S_R{}^2\right)^{\frac{1}{2}} \qquad (B.7)$$

For these calculations, the expanded uncertainty in the result at approximately 95 % is taken to be,

$$U_{R,95} = 2U_R \qquad (B.8)$$

Now, for the present experiments, the parameters taken for sensitivity analysis are the inlet air humidity, air velocity and the fin base temperature. There were other parameters which might have an effect on the mass measurements, but those parameters were either dependent on the selected parameters or were not easily controllable. For e.g., the inlet air temperature depends on the inlet air humidity and the room temperature and humidity. The air temperature depends on the mass of moist air injected into the system, which again depends on the humidity of the atmospheric air. Thus, to attain a given relative humidity inside the wind tunnel, mass of air injected had to be changed which made a change on the air temperature, over which there was not any control.

As already described, the inlet moist air relative humidity was measured using a data logger (Omega OM-62) having a systematic uncertainty of ±2% RH[30]. The logger recorded the humidity levels every ten second, hence for a total experimental run time of 90 minutes[31], 540 readings were recorded. A typical plot showing the humidity variation with time was shown in Figure 3.21. These 540 readings were then used to calculate the standard random uncertainty in this measurement. Also, to determine the sensitivity of the relative humidity measurement on the mass measurements, tests were conducted at three different relative humidity levels. The

[30] As provided by the manufacturer
[31] This excludes the time taken to attain a given humidity level

variation of the steady-state retained condensate mass with change in the relative humidity is shown in Figure 3.23. As seen in the figure, there is not much effect of changing relative humidity on the mass retained. However, the steady-state retained mass increases almost linearly with increasing relative humidity. The slope of the linear fit has been taken to the sensitivity. The calculated slope or the sensitivity was found out to be 2.89 g/%RH/100. Thus, the retained mass changes by 2.89/100 g for 1% change in the moist air inlet relative humidity.

The fin base temperature was measured at three different locations on the base aluminum plate, as shown in Figure 2.18. The temperature was measured using thermo-loggers (Omega HH506RA), having an uncertainty of 0.05% of the reading and type-J thermocouple wires. The fin base temperature was recorded every ten minutes for the 90 minutes experiment run time. Thus, there were 9 readings at three locations each, covering the entire run time of the experiment. The temperature at the three locations was averaged for each time interval and thus a total of 9 readings were used to calculate the standard random uncertainty associated with the temperature measurement. Further, to determine the sensitivity of temperature measurement on the measurement of retained condensate mass, the quantitative tests were performed for different values of steady state fin base temperature, keeping the other parameters constant. The temperature was varied by varying the supply dc voltage to the thermoelectric device. The variation of the steady-state retained condensate mass with change in the average fin base temperature[32] is shown in Figure 3.28. As seen in the figure, there is not much effect of changing fin base temperature on the mass retained. As expected, the steady-state mass retained decreases with increase in the fin base temperature. The slope of the linear fit has been taken to the

[32] The averaging is done over nine temporal readings apart from the three spatial readings

sensitivity. The calculated slope or the sensitivity was found out to be 0.487 g/ ^{0}C. Thus, the retained mass changes by only 0.487 g for 1^0C change in the fin base temperature.

The air velocity was measured at 7 different locations spaced equally along the height at the exit of the fin column. The air velocity was measured using a velocimeter (Veloci-Calc 8355), providing accurate measurements up to 2.5% of the reading. Though the air velocity was measured 3-4 times during the experiment at all the 7 locations, but after the start of the experiment the air velocity was different than the initial readings because of bridging of fins/louvers by condensate. Hence, 7 readings recorded just before the start of the experiment were considered for calculation of the uncertainties. The air velocity was varied from 1.5 to 3.5 m/s, and the effect on the retained mass was calculated. The air velocity was varied by varying the supply dc voltage of the fan used. The variation of retained condensate mass at steady state with changing air velocity is shown in Figure 3.26. It can be seen that the variation of the steady state retained mass with air velocity is linear in the range of variation. As the velocity goes high, the retained mass increases. The slope was calculated to be 0.79 g/m/s.

The mass was dynamically recorded using the Sartorius GP-8201, having an accuracy of 0.1 g. Any standard random uncertainty associated with the balance was not considered. Finally, Table B.4 summarizes the systematic errors and the sensitivities associated with the measurements which affect the measurement of the retained condensate mass. Thus, total random standard uncertainty of the present measurements may be expressed as,

$$S_R = \left[\left(\theta_\phi S_{\bar{\phi}}\right)^2 + \left(\theta_T S_{\bar{T}_b}\right)^2 + \left(\theta_v S_{\bar{v}_{air}}\right)^2\right]^{1/2} \qquad (B.9)$$

Where, θ_i are the associated sensitivities, and can be interpreted as,

Sensitivity of inlet relative humidity,

$$\theta_{\phi} = \frac{\partial m}{\partial \phi} \qquad (B.10)$$

Sensitivity of fin base temperature,

$$\theta_{T} = \frac{\partial m}{\partial T_b} \qquad (B.11)$$

And , sensitivity associated with the air velocity,

$$\theta_{v} = \frac{\partial m}{\partial v_{air}} \qquad (B.12)$$

and $S_{\overline{\phi}}, S_{\overline{T}_b}, S_{\overline{v}_{air}}$ are random standard uncertainties. The total standard systematic uncertainty is evaluated using an expression similar to that in Eq. (B.9), with the random uncertainties replaced by systematic uncertainties and an extra term for accounting the systematic uncertainty associated with the electronic balance.

A sample calculation for the uncertainty estimation has been shown here for the fin Design 1 baseline case (i.e. without drainage channels). The targeted values for the experiment were:-

Relative Humidity: 85%, fin base temperature: 15 ^{0}C and air velocity: 3.5 m/s. The values of the standard random and systematic uncertainties and their corresponding effect on the mass measurement are shown in Table B.5 for this sample case. The total standard random uncertainty is then calculated as,

$S_R = [(0.0014)^2 + (0.079)^2 + (0.069)^2]^{1/2}$= 0.105 g

And, the total standard systematic uncertainty is similarly,

B_R=0.109 g

The combined total uncertainty is then,

$U_{R,95} = 2U_R = 2\left(B_R{}^2 + S_R{}^2\right)^{\frac{1}{2}}$=0.303 g

Therefore, the relative uncertainty is, 0.303/9.52= 3.18 %.

Finally, the absolute and relative uncertainties for all the samples tested for fin Design 1 at 85% RH and 3.5 m/s air velocity and fin Design 2 at 2.5 m/s air velocity are shown in Table B.6. From the table, it can be seen that the relative uncertainties for designs 1 and 2 lie in the range 3-4.5%, which is greater than most of the differences created by the drainage channels for Design 1. However, this is greater than the differences caused in Design 2. Similarly, Table B.7 sows the absolute and relative uncertainties associated with Design 3 and Design 4 samples. The uncertainty in Design 3 samples lie in the range 6-9%. It is high, because of small amount of condensate retained by the design. However, it is still less than the difference caused by the drainage channels. For Fin Design 4, the relative uncertainty is in the range 2-3%.

Table B.1 Uncertainty in Design 1 samples (dynamic dip tests)

Channel	*Static Retention, Mean μ (g)*	U_{95} (g)	*% relative uncertainty*
Baseline	16.7	0.244	1.46%
Rectangular:			
1×1 mm			
1 channel	10.8	0.213	1.98%
2 channels	10.7	0.290	2.71%
1×2 mm	14.9	0.264	1.78%
2×1 mm	15.4	0.255	1.66%
2×2 mm	16.9	0.306	1.81%
Triangular:			
45° 1 mm wide			
1 channel	10.2	0.36	3.53%
2 channels	8.8	0.29	3.29%
90° 1 mm wide	12.3	0.56	4.56%
90° 1 mm deep	11.9	0.42	3.53%
Trapezoidal			
1mm wide 120°	12.1	0.455	3.76%

Table B.2 Uncertainty in some of the Design 2 samples (dynamic dip tests)

Channel	*Static Retention, Mean μ (g)*	U_{95} (g)	*% relative uncertainty*
Baseline	10.2	0.3	2.94%
Rectangular:			
1×1 mm	10.2	0.201	1.97%
1×2 mm	10.1	0.253	2.45%
Triangular:			
45° 1 mm wide	10.2	0.212	2.07%

Table B.3 Uncertainties in contact angle measurements

Condition of the Surface	*Mean Contact Angle (^{0})*	U_{95} (^{0})	*% relative uncertainty*
Unwashed	78.95	2.30	2.91 %
After few cycles of experimentation	75.1	3.02	4.02 %
Acetone wash	65.71	4.06	6.17 %

Table B.4 Systematic errors and sensitivities of the measurements

Measurement	*Systematic Error*	*Sensitivity (θ_i)*
Inlet Relative Humidity	$\pm$ 2.0 % RH	2.89 g/%RH/100
Air Velocity	2.5 % rdg $\pm$ 0.05 m/s	0.79g/m/s
Fin Base Temperature	$\pm$ (0.05 % rdg +0.3 ^{0}C)	0.487 g/^{0}C
Mass (electronic balance)	$\pm$ 0.1 g	1 g/g

Table B.5 Uncertainties and their effect for a sample case (fin Design 1 baseline)

Parameter	*Mean Value ($\overline{X}_i$)*	*Standard Random Uncertainty ($S_{\overline{X}_i}$)*	$\theta_i S_{\overline{X}_i}$[33]	*Standard Systematic Uncertainty ($B_{\overline{X}_i}$)*	$\theta_i B_{\overline{X}_i}$[34]
Inlet Relative Humidity (%)	86.2 %	0.049%	0.0014	1 %	0.0289
Air Velocity (m/s)	3.51	0.087	0.069	0.069	0.0544
Fin Base Temperature (^{0}C)	15.71	0.162	0.079	0.154	0.075
Mass (g)	9.5	--	--	0.05	0.05

[33] This quantity has units of mass (grams)
[34] This quantity has units of mass (grams)

Table B.6 Absolute and relative uncertainties associated with Design 1 and Design 2 samples

Channel	*Design 1*			*Design 2*		
	Static retention (g)	Absolute total uncertainty (g)	Relative uncertainty (%)	Static retention(g)	Absolute total uncertainty (g)	Relative uncertainty (%)
Baseline	9.5	0.303	3.18 %	7.56	0.271	3.58 %
Rectangular:						
1×1 mm	7.7	0.294	3.82%	7.27	0.272	3.75%
1×1 mm (non-vertical grooves)	8.7	0.321	3.69%			
1×2 mm	8.5	0.34	4%	7.3	0.31	4.25%
Triangular:						
22.5° 1 mm wide	8.0	0.292	3.65%			
45° 1 mm wide	7.3	0.33	4.5%			
90° 1 mm wide	8.3	0.268	3.23%			
Trapezoidal:						
1mm wide 120°	8.0	0.312	3.9%			

Table B.7 Absolute and relative uncertainties associated with Design 3 and Design 4 samples

Channel	*Design 3*[35]			*Design 4*[36]		
	Static Retention (g)	Absolute total uncertainty (g)	Relative uncertainty (%)	Static Retention(g)	Absolute total uncertainty (g)	Relative uncertainty (%)
Baseline	5.4	0.372	6.88%	12.6	0.329	2.61%
Rectangular:						
1×1 mm	4.4	0.363	8.1%	10.1	0.278	2.75%
1×1 mm (2 channels)	4.0	0.373	9.33%			
Triangular: 45° 1 mm wide	4.6	0.328	7.1%			

[35] Tests were conducted at air speed=3.5-3.6 m/s, and RH=85-87%
[36] Tests were conducted at air speed=2.5-2.6 m/s, and RH=85-87 %

Appendix C- Heat Transfer Calculations and EES Code

In this Appendix, a detailed description of the heat transfer and the pressure drop analysis that was carried out to assess the effect of reduction in condensate retention caused by the drainage channels, on the heat transfer and pressure drop characteristics of full-size heat exchangers. The Appendix describes the working on the EES code and the equations used in the analysis. The EES code which was used is also attached at the end of the appendix. In the first section, the heat and mass transfer analysis is presented, and in the second, the pressure drop analysis.

C.1 Heat/Mass Transfer Analysis

C.1.1 Coolant Side Calculations

The coolant/fluid used in the calculations was ethylene glycol solution (53.6 % by weight). The thermodynamic properties of the fluid were obtained from the correlations developed as a function of temperature. Software FLUIDFILE®, provided by the DOW Chemical Company, was used to obtain various properties at varying temperatures and thus the variations in the properties were curve-fitted with temperature.

Further, the fluid flow inside the tubes was assumed to be hydro dynamically fully developed but thermally developing. Hence, corresponding relation between the Nu and the Pr no. was used, for constant heat flux, shown here [54]:

$$Nu_D = 4.36 + \frac{0.0668 \times \frac{D_h}{l_{tube}} \times Re_D \times Pr}{1 + 0.04\left[\frac{D_h}{l_{tube}} \times Re_D \times Pr\right]^{\frac{2}{3}}} \qquad (C.1)$$

And then the coolant heat transfer coefficient was calculated. The coolant side thermal resistance was then found out using the value of this heat transfer coefficient.

C.1.2 Conduction Resistance

The conduction thermal resistance taken into account in this analysis was due to the thickness of the aluminum tube, extra thickness of metal adhered to the tubes to design the channels, and the thermal resistance of the thermal epoxy used .The resistance due to the tube was evaluated as,

$$R_{tube} = \frac{\delta_{tube} + \delta_{extra}}{A_{tube} \times h_{tube} \times N_{tube}} \qquad (C.2)$$

And in a similar manner, the resistance due to thermal epoxy was calculated.

C.1.3 Air Side Resistance

To calculate the air side thermal resistance, heat transfer coefficient was first calculated from the Colburn j-factor, which was further estimated from the correlation. The calculation was done separately for the channeled and the non-channeled samples.

C.1.3.1 Estimation of j- factor and heat transfer coefficient

The Colburn j-factor was estimated from the correlations for the louver-fin heat exchanger given by Park and Jacobi [31], which were developed recently, consisting of largest number of experimental data points. The factor depends on the louver fin geometrical parameters, and Reynolds number, which further depends on the operating conditions. The correlation as used was,

$$j = C_1 j_{Re} j_{low} j_{louver} \alpha^{C_2} N_{LB}^{C_3} \left(\frac{F_w}{L_p}\right)^{C_4} \left(\frac{F_d}{F_p}\right)^{C_5} \left(\frac{L_w}{F_w}\right)^{C_6} \left(\frac{F_w}{T_p}\right)^{C_7} \left(1 - \frac{\delta_f}{L_p}\right)^{C_8} \left(\frac{L_p}{F_p}\right)^{C_9} \qquad (C.3)$$

where,

$$j_{Re} = Re_{L_p}^{\left[C_{10} + C_{11} cosh\left(F_p/(L_p - 1)\right)\right]} \qquad (C.4),$$

$$j_{low} = 1 - sin\left(\frac{L_p}{F_p}.\alpha\right)\left[cosh\left(C_{12} Re_{L_p} - C_{13}\frac{F_d}{N_{LB} F_p}\right)\right]^{-1} \qquad (C.5)$$

and,

$$j_{louver} = 1 - C_{14} tan(\alpha) \left(\frac{F_d}{N_{LB} F_p}\right) cos\left[2\pi \left(\frac{F_p}{L_p tan(\alpha)} - 1.8\right)\right] \qquad (C.6)$$

C_{1-14} are the regression constants. The values can be found in Table C.1. [31]

The value of heat transfer coefficient was found from the estimated value of the Colburn j- factor using the relation,

$$j = \frac{h_{air}}{C_{p,air} G_c} Pr_{air}^{\frac{2}{3}} \qquad (C.7)$$

C.1.3.2 Concept of wet multipliers

The Colburn j-factor obtained from the correlations discussed above is for the completely dry conditions. To evaluate the factors for the wet conditions, the concept of wet multipliers was used. They are the multiplication factors provided by Park and Jacobi [41], which when multiplied with the Colburn j- and the friction f- factors, give the corresponding factors for the completely wet conditions.

$$j_{wet} = j \times \varphi_j \qquad (C.8)$$

and,

$$f_{wet} = f \times \varphi_f \qquad (C.9)$$

The wet multiplication factors for the Colburn j- and friction factor were given as correlations depending on the fin geometrical parameters, receding contact angle of the fin surface and Reynolds number, which depended on some of the operating conditions like air velocity, viscosity and density. The correlation, as provided in the paper is,

$$\varphi_j = \left[\left(Re_{L_p}^{C_1} + \left(\frac{L_p}{F_p}\right)^{C_2} Re_{L_p}^{C_3}\right)\left(\frac{L_w}{F_w}\right)^{C_4} sin(\alpha + C_5)\right]\left(\frac{F_d}{F_p}\right)^{C_6} (cos\,\theta_R)^{C_7}\left(1 - \varphi_{j,duct}\right) + \varphi_{j,duct} \quad (C.10)$$

where,

$$\varphi_{j,duct} = 1 - exp\left[C_8\left(\frac{F_p}{L_p}\right)^3\right] \quad (C.11)$$

C_{1-8} are again the regression constants obtained for this correlation. Their values are tabulated in Table C.3. Similarly, for the friction factor, a similar relation was used,

$$\varphi_f = \left[D_1 + D_2 exp\left(D_3 Re_{L_p}\right)(\sin\alpha)^{D_4}\left(\frac{L_p}{F_p}\right)^{D_5}\right]\left(\frac{F_w}{T_p}\right)^{D_6}\left(\frac{L_p}{F_p}\right)^{D_7}\left(\frac{L_w}{F_w}\right)^{D_8} \quad (C.12)$$

The values of the regression constants are presented in Table C.4.

Also, as discussed previously (Chapter-4), the non-channeled sample was assumed to be completely wet, and the correlations for complete wet conditions were used. For the channeled case, average values based on the maximum reduction in the retention obtained were taken. The percentage retention in reduction was directly translated to be the effect in *j*- and the *f*-factors.

C.1.3.3 Fin Efficiency

For calculating fin efficiency, the louver fin geometry was modeled as a straight fin with an adiabatic tip. Further, the centerline of the fin surface was taken as the adiabatic tip. Further simplifying, all the fins were assumed to be at the same temperature. The fin efficiency under the wet conditions was calculated using a method suggested by Park and Jacobi [41], as shown

below, based on the analogy between heat and mass transfer and further on the assumption that Le~1 for air-water vapor mixture. For wet conditions, the fin efficiency is calculated as,

$$\eta_w = \frac{tanh(m_w L)}{m_w L} \qquad (C.13),$$

where, fin parameter m_w is related to the dry fin parameter with the relation,

$$m_w{}^2 = \frac{m^2 b_f}{C_{p,air}} \qquad (C.14)$$

where,

$$m = \left(\frac{hP}{k_f A}\right)^{\frac{1}{2}} \qquad (C.15)$$

For fins with fin width much greater than the fin depth, as in the present case, the expression reduces to,

$$m = \left(\frac{2h}{k_f \delta_f}\right)^{\frac{1}{2}} \qquad (C.16)$$

In Eq. (C.14), b_f is the slope of saturated enthalpy line between fin base temperature and fin tip temperature, evaluated as,

$$b_f = \frac{i_{s,b} - i_{s,t}}{T_b - T_t} \qquad (C.17)$$

And the average fluid temperature was taken as the fin base temperature, and the average air temperature as the fin tip temperature.

The overall surface effectiveness was then calculated from the fin efficiency using the standard relation,

$$\eta_{o,wet} = 1 - \frac{A_{fin}}{A_{total}}\left(1 - \eta_{f,wet}\right) \quad (C.18)$$

Finally, the total resistance for the air side was calculated as,

$$R_{air} = \frac{1}{\eta_{o,wet} h_{air} A_{total}} \quad (C.19)$$

C.1.4. Overall Heat Transfer Coefficient

The overall heat transfer coefficient for the wet conditions was evaluated using the thermal resistances of the coolant, conduction resistance and the air side resistance, using a relation used by Xia and Jacobi [55], as,

$$\frac{1}{UA_{total}} = \left[\left(R_{cool} + R_{tube} + R_{epoxy}\right)\frac{Q_{total}}{Q_{sens}} + R_{air}\right] \quad (C.20)$$

C.1.5 Heat/ Mass Transfer Equations

After determination of the overall heat transfer coefficient, equations for the simultaneous heat and mass transfer were solved. The effectiveness-NTU method [56] was used to solve for the sensible heat transfer using the obtained overall heat transfer. Number of transfer units was first determined from the heat transfer coefficient as,

$$\mathrm{NTU} = \frac{\mathrm{UA_{total}}}{\mathrm{C_{min}}} \quad (C.21)$$

The effectiveness was then determined using the relation for single pass, cross flow configuration, given as,

$$\varepsilon = 1 - exp\left\{{C_r}^{-1} NTU^{0.22}\left[exp\left(-C_r NTU^{0.78}\right) - 1\right]\right\} \quad (C.22)$$

with,

$$\mathrm{C_r} = \frac{C_{min}}{C_{max}} \quad (C.23)$$

The sensible component of heat transfer rate was then calculated as,

$$\dot{Q}_{sens} = \varepsilon C_{min}\left(T_{air,in} - T_{cool,in}\right) \quad (C.24)$$

The heat transfer rate on the air-side was calculated as,

$$\dot{Q}_{total,air} = \dot{m}_{air}\left(i_{air,in} - i_{air,out}\right) \quad (C.25)$$

The coolant side heat transfer rate can be written as,

$$\dot{Q}_{total,cool} = \dot{m}_{cool}C_{p,cool}\left(T_{cool,out} - T_{cool,in}\right) \quad (C.26)$$

For simplification of the analysis, the following assumption was made,

$$\dot{Q}_{total,air} = \dot{Q}_{total,cool} = \dot{Q}_{total} \quad (C.27)$$

Also, the total heat transfer rate was written as the sum of its latent and the sensible components as,

$$\dot{Q}_{total} = \dot{Q}_{lat} + \dot{Q}_{sens} \quad (C.28)$$

Further, the latent component was determined from the mass deposition rate of condensate and the enthalpy of vaporization of water as,

$$\dot{Q}_{lat} = \dot{m}_c i_{fg} \quad (C.29)$$

And the mass deposition rate of condensate was determined from mass transfer equations developed on the mass transfer driving potential. The set of equations used is standard and is provided in some texts [57]. The binary mass diffusivity of water in air is calculated as,

$$D_{H2O,air} = 0.00002567\left(\frac{T_s + 273.15}{300}\right)^{\frac{3}{2}} \quad (C.30)$$

Here, temperature is in ^{0}C. The expression is a simplified form of the diffusivity equation, obtained from the Chapman-Enskog kinetic theory, for the air-water system.

The Schmidt number for water in air at the surface of the exchanger is then defined in terms of the kinematic viscosity and the mass diffusivity as,

$$Sc_s = \frac{\nu_{air,s}}{D_{H2O,air}} \qquad (C.30)$$

This quantity is analogous to the Prandtl number in heat transfer. Other quantities as Nusselt no. based on the fin spacing and Prandtl number of moist air at the surface were then evaluated. Using heat and mass transfer analogy, the Sherwood number was evaluated as,

$$Sh = Nu\left(\frac{Sc_s}{Pr_{air,s}}\right)^{\frac{1}{3}} \qquad (C.31)$$

Defining the mass transfer coefficient at zero mass transfer rate, and is determined only by the flow configuration and physical properties,

$$g_m^* = Sh \times D_{H2O,air} \times \frac{\rho_{air,s}}{F_p} \qquad (C.32)$$

The mass transfer driving force at the inlet (air) of the heat exchanger is defined as,

$$\beta_i = \frac{mf_{ws} - mf_{wi}}{1 - mf_{ws}} \qquad (C.33)$$

Where the quantities in the numerator and the denominator are the mass fractions of water vapor at the air-water interface and the inlet. These quantities are determined by the density ratios of the water to that of moist air. Similarly, the mass transfer driving force at the exit is defined as,

$$\beta_o = \frac{mf_{ws} - mf_{wo}}{1 - mf_{ws}} \tag{C.34}$$

Hence, the log mean driving force evaluated from the forces at the inlet and the exit, is given by an expression similar to that used for LMTD,

$$\beta_i = \beta_o exp\left(\frac{\beta_i - \beta_o}{\beta_{lm}}\right) \tag{C.35}$$

The mass transfer coefficient at finite rate is evaluated using the Couette flow model as,

$$g_m = g_m^* \left[\frac{ln(1 + \beta_{lm})}{\beta_{lm}}\right] \tag{C.36}$$

Finally, the mass transfer rate (condensation rate) is calculated as,

$$\dot{m}_c = -A_{total} \times g_m \times \beta_{lm} \tag{C.37}$$

The humidity ratio at the exit and the mass fraction are linked by the equation,

$$\omega_{air,o} = \frac{mf_{wo}}{1 - mf_{wo}} \tag{C.38}$$

And the relation between the exit humidity ratio and the mass flow rate is, based on the concept that the rate of mass of water vapor lost by the air is equal to the mass of condensate rate deposited on the surface. Hence,

$$\dot{m}_c = \dot{m}_{air} \frac{\left(\omega_{air,i} - \omega_{air,o}\right)}{1 + \omega_{air,i}} \tag{C.39}$$

Thus, Equations (C.21)-(C.39) define the complete set of heat and mass transfer equations applied in this analysis.

C.2 Pressure Drop Analysis

Similar to the heat and mass transfer analysis, the pressure drop across the heat exchanger was calculated from the friction f-factors, which were estimated from the correlations.

C.2.1 Estimation of f-factor

Again, the f-factor was estimated from the correlations provided by Park and Jacobi [31]. The factor depends on the louver fin geometrical parameters, and Reynolds number, which further depends on the operating conditions. The correlation as used was,

$$f = D_1 f_{Re} {N_{LB}}^{D_2} \left(\frac{F_p}{L_p}\right)^{D_3} sin(\alpha + D_4) \left(\frac{\delta_f}{L_p}\right)^{D_5} \left(\frac{L_w}{F_w}\right)^{D_6} \left(\frac{F_w}{F_p}\right)^{D_8} \left(1 - \frac{F_w}{T_p}\right)^{D_5} \quad (C.40)$$

and

$$f_{Re} = \left(Re_{L_p} \frac{F_p}{L_p}\right)^{D_9} + D_{10} {Re_{L_p}}^{\left(D_{11} \frac{\delta_f}{F_p}\right)} \quad (C.41)$$

D_{1-11} are the regression constants. Their value is provided in Table C.2.

Again, the concept of wet multipliers was used to calculate the friction factor for the complete wet condition, and the simplifying expression for the evaluation of channeled sample performance.

C.2.2 Pressure Drop from f-factor

From the f-factors, the pressure drop was calculated using the relation given by Kays and London [15], which takes into account the loss coefficients at the entrance and the exit. The relation used was,

$$\Delta P = \left[f A_{air} \frac{\rho_{air,i}}{A_{min}\rho_{air,m}} - (1 - \sigma^2 - K_e)\frac{\rho_{air,i}}{\rho_{air,o}} + 2\left(\frac{\rho_{air,i}}{\rho_{air,o}} - 1\right) + K_c + 1 - \sigma^2 \right] \frac{{G_c}^2}{2\rho_{air,i}} \qquad (C.42)$$

where, σ is the contraction ratio defined by,

$$\sigma = \frac{A_{min}}{A_{fr}} \qquad (C.43)$$

The entrance and exit pressure-loss coefficients, K_c and K_e, were evaluated according to Kays and London [15] with an assumption of highly interrupted fin geometry.

Finally the EES code listing is shown in Table C.5.

Table C.1 Regression constants for the j-correlation [31]

C_1	0.872
C_2	0.219
C_3	-0.0881
C_4	0.149
C_5	-0.259
C_6	0.540
C_7	-0.902
C_8	2.62
C_9	0.301
C_{10}	-0.458
C_{11}	-0.00874
C_{12}	0.049
C_{13}	0.142
C_{14}	-0.0065

Table C.2 Regression constants for f- factor correlation [31]

D_1	3.69
D_2	-0.256
D_3	0.904
D_4	0.200
D_5	0.733
D_6	0.648
D_7	-0.647
D_8	0.799
D_9	-0.845
D_{10}	0.0013
D_{11}	1.26

Table C.3 Regression constants for the wet multiplier for j-factor [41]

C_1	-1.215
C_2	0.5782
C_3	0.0359
C_4	0.4332
C_5	0.2423
C_6	0.04894
C_7	0.3659
C_8	-0.01426

Table C.4 Regression constants for the wet multiplier for f-factor [41]

D_1	0.7564
D_2	0.2602
D_3	-0.003949
D_4	0.3532
D_5	4.168
D_6	-0.07233
D_7	-0.03771
D_8	-0.8744

Table C.5 EES Code listing for calculating the heat transfer and pressure drop

```
"EES Code for evaluating the heat transfer for a louver-fin flat-tube heat exchanger with given inlet conditions and fin/exchanger geometry"

"Defining all the procedures and modules"


"Procedure for evaluating properties of the liquid inside the tube. Liquid is Ethylene Glycol"
PROCEDURE ethglyprop(T: k, Pr, nu,C_p,rho)
rho=1102.1382-0.50217*T-0.0015*T^2                                  {Density, kg/m^3}
k= 0.34115+7.09E-4*T-2.81E-6*T^2                                    {Thermal conductivity, k, W/m-K}
mu=(9.18-0.391*T+0.01215*T^2-3.08E-4*T^3+4.73E-6*T^4-2.93E-8*T^5)*(10^(-3))
                                                                    {Dynamic Viscosity of coolant, kg/m-s}
C_p=3.09353+(0.00414*T)                                             {Specific heat capacity, KJ/kg-K}
Pr=(mu*C_p/k)*(10^3)                                                {Liquid Prandtl number}
nu=mu/rho                                                           {Kinematic Viscosity, m^2/s}
END
“End of procedure for evaluating fluid properties”


"Module for correlation of  j (Colburn j- factor) from Park and Jacobi (2009) [31]"
MODULE
correlation(F_p,L_p,F_d,F_w,L_w,delta_f,alpha,N_L_B,T_p,v,Temp,Press,RH,sigma: j)
mu_air=VISCOSITY(AirH2O, T=Temp,P=Press,R=RH)
                                                                    {Dynamic Viscosity of moist air, kg/m-s}
rho_air=DENSITY(AirH2O, T=Temp,P=Press,R=RH)                        {Density of moist air, kg/m^3}
v_max=v/sigma                                                       {max velocity at min free flow area, m/s}
Re_Lp=rho_air*v_max*L_p/mu_air                                      {Reynolds number based on Louver Spacing}
C_1=0.872                                                           {Values of regression constants from Park and Jacobi (2009)[31]}
C_2=0.219
C_3=-0.0881
C_4=0.149
C_5=-0.259
C_6=0.540
C_7=-0.902
C_8=2.62
C_9=0.301
C_10=-0.458
C_11=-0.00874
C_12=0.0490
C_13=0.142
C_14=-0.0065
j_Re=(Re_Lp)^(C_10+C_11*cosh(F_p/L_p-1))
j_low=1-sin(L_p/F_p*alpha)*1/(cosh(C_12*Re_Lp-C_13*F_d/(N_L_B*F_p)))
```

```
j_louver=1-C_14*tan(alpha)*(F_d/(N_L_B*F_p))*cos(2*pi*(F_p/(L_p*tan(alpha))-1.8))
j=C_1*j_Re*j_low*j_louver*((alpha)^(C_2))*((N_L_B)^(C_3))*((F_w/L_p)^(C_4))*((F_d/F_p
)^(C_5))*((L_w/F_w)^(C_6))*((F_w/T_p)^(C_7))*((1-delta_f/L_p)^(C_8))*((L_p/F_p)^(C_9))
{Final relation for j- factor based on fin geometrical parameters and operating conditions}
END
"End of Module for calculating the j-correlation"


"Procedure for correlation of  f (Fanning f- factor from Park and Jacobi (2009)[31] "
PROCEDURE
fcorrelation(F_p,L_p,F_d,F_w,L_w,delta_f,alpha,N_L_B,T_p,v,Temp,Press,RH,sigma: f)
mu_air=VISCOSITY(AirH2O, T=Temp,P=Press,R=RH)
                                                {Dynamic Viscosity of moist air, kg/m-s}
rho_air=DENSITY(AirH2O, T=Temp,P=Press,R=RH)          {Density of moist air, kg/m^3}
v_max=v/sigma                                  {max velocity at min free flow area, m/s}
Re_Lp=rho_air*v_max*L_p/mu_air                 {Reynolds number based on Louver
Spacing}
D_1=3.69                                  {Values of coefficients from Park and Jacobi (2009)}
D_2=-0.256
D_3=0.904
D_4=0.200
D_5=0.733
D_6=0.648
D_7=-0.647
D_8=0.799
D_9=-0.845
D_10=0.00130
D_11=1.26
f_Re=(Re_Lp*F_p/L_p)^(D_9)+D_10*Re_Lp^(D_11*delta_f/F_p)
f=D_1*f_Re*(N_L_B^(D_2))*((F_p/L_p)^(D_3))*(sin(alpha+D_4))*((delta_f/L_p)^(D_7))*((L
_w/F_w)^(D_6))*((F_w/F_p)^(D_8))*((1-F_w/T_p)^(D_5))
END
"procedure to evaluate f ends here"


"Procedure to evaluate h (heat transfer coefficient) from Colburn j-factor"
PROCEDURE hfromj(j,v,Temp,Press,RH,sigma:h,C_pair,rho_air)
      {returns heat transfer coefficient, specific heat capacity, and density of moist air at average
                                                                              properties}
mu_air=VISCOSITY(AirH2O, T=Temp,P=Press,R=RH)
rho_air=DENSITY(AirH2O, T=Temp,P=Press,R=RH)
C_pair=CP(AirH2O, T=Temp, P=Press, R=RH)
k_air=conductivity(AirH2O, T=Temp, P=Press, R=RH)
Pr_air=(mu_air*C_pair/k_air)*10^(3)
v_max=v/sigma                                  {max velocity at min free flow area, m/s}
G_c=rho_air*v_max                               {mass flow rate of moist air , kg/m^2-s}
```

```
h=(j*G_c*C_pair/(Pr_air)^(2/3))*10^(3)                    {heat transfer coefficient, W/m^2-K}
END
"procedure to evaluate h ends here"
"Procedure for calculating the wet surface multiplier for j factor (Park and Jacobi (2009)) [41]"
" Wetmultiplier is used to obtain the factors under complete wet conditions of operation"
PROCEDURE wetmultiplier (F_p,L_p,F_d,F_w,L_w,delta_f,alpha,theta,v,Temp,Press,
RH,sigma:phi_j,Re_Lp)
mu_air=VISCOSITY(AirH2O, T=Temp,P=Press,R=RH)
rho_air=DENSITY(AirH2O, T=Temp,P=Press,R=RH)
C_pair=CP(AirH2O, T=Temp, P=Press, R=RH)
k_air=conductivity(AirH2O, T=Temp, P=Press, R=RH)
Pr_air=(mu_air*C_pair/k_air)*10^(3)
v_max=v/sigma
Re_Lp=rho_air*v_max*L_p/mu_air
C_1=-1.215
C_2=0.5782
C_3=0.03590
C_4=0.4332
C_5=0.2423
C_6=0.04894
C_7=0.3659
C_8=-0.01426
phi_j_duct=1-exp((C_8)*(F_p/L_p)^3)
phi_j=((Re_Lp)^(C_1)+((L_p/F_p)^(C_2))*(Re_Lp)^(C_3))*((L_w/F_w)^(C_4))*(sin(alpha+C
_5))*((F_d/F_p)^(C_6))*((cos(theta))^(C_7))*(1-phi_j_duct)+phi_j_duct
                                                    {wet multiplier for colburn j-factor}
END
"Procedure for calculating the wet surface multiplier for j- factor ends here"


"Procedure for calculating the wet surface multiplier for f factor"
PROCEDURE fwetmultiplier (F_p,L_p,F_d,F_w,L_w,delta_f,alpha,T_p,v,Temp,Press,
RH,sigma:phi_f)
mu_air=VISCOSITY(AirH2O, T=Temp,P=Press,R=RH)
rho_air=DENSITY(AirH2O, T=Temp,P=Press,R=RH)
C_pair=CP(AirH2O, T=Temp, P=Press, R=RH)
k_air=conductivity(AirH2O, T=Temp, P=Press, R=RH)
Pr_air=(mu_air*C_pair/k_air)*10^(3)
v_max=v/sigma
Re_Lp=rho_air*v_max*L_p/mu_air
D_1=0.7564
D_2=0.2602
D_3=-0.003949
D_4=0.3532
D_5=4.168
D_6=-0.07233
```

```
D_7=-0.03771
D_8=-0.8744
phi_f=(D_1+D_2*exp(D_3*Re_Lp)*((sin(alpha))^(D_4))*((L_p/F_p)^(D_5)))*((F_w/T_p)^(D_6))*((L_p/F_p)^(D_7))*((L_w/F_w)^(D_8))
END
"Procedure for calculating the wet surface multiplier for f factor ends"


"Procedure for evaluating pressure drop from friction factor"
PROCEDURE pfromf(A_min,A_air,Temp,Press,rho_ai,v,RH,sigma, rho_ao,f:delta_p)
rho_air=DENSITY(AirH2O, T=Temp,P=Press,R=RH)
v_max=v/sigma
G_c=rho_air*v_max
K_c=0.5                          {Values of loss coefficients taken from Kays and London [15]}
K_e=-0.35
delta_p=(f*A_air*rho_ai/(A_min*rho_air)-(1-sigma^2-K_e)*(rho_ai/rho_ao)+2*(rho_ai/rho_ao-1)+(K_c+1-sigma^2))*G_c^2/(2*rho_ai)
END
"Procedure for evaluating pressure drop ends"


"Procedure to calculate the overall efficiency"
MODULE eff(h,k_f,delta_f,F_w,A_fin,A_total,b_f,Cp:eta_0)
m=(2*h/(k_f*delta_f))^(1/2)                {Expression for dry conditions with adiabatic tip}
m_w=((m^2)*b_f/Cp)^(1/2)                                {modifying for wet conditions}
L_f=(F_w)/2
eta_f=(tanh(m_w*L_f))/(m_w*L_f)                                                {fin efficiency}
eta_0=1-((A_fin)/(A_total))*(1-eta_f)                                {surface effectiveness}
END
"Procedure to calculate the overall efficiency ends"


"Procedure to determine the value of epsilon for the effectiveness-NTU method"
PROCEDURE eps(UA,mdot_cool,mdot_a, Cp_air, Cp_cool:epsilon,C_min)
C_cool=mdot_cool*Cp_cool
C_air=mdot_a*Cp_air
IF (C_air>C_cool) THEN                        { If Loop to determine the C_min and C_max}
C_min=C_cool
C_max=C_air
ELSE
C_min=C_air
C_max=C_cool
ENDIF
NTU=UA/C_min                                                        {No. of transfer Units}
Cr=C_min/C_max
epsilon=1-exp((1/Cr)*((NTU)^(0.22))*(exp(-Cr*((NTU)^(0.78)))-1))
```

```
                                                {Relation for single pass, cross flow configuration}
END
" Procedure to determine the effectiveness ends"

"Module to calculate the heat transfer and outlet quantities"
MODULE finalcalc
(T_s,p,T_ai,T_ci,w_ai,R_i,h,P_f,A_To,mdot_a,mdot_cool,UA,Cp_cool,C_min,epsilon,mf_wi,h_
ai:Q,Q_sens,Q_lat,SHR,T_ao,T_co,w_ao,rho_ao)
"Thermophysical properties"
cp_s=1000*Cp(AirH2O,T=T_s, P=p, R=1)              {moist-air specific heat at surface, J/kg-K}
D_AB=(25.67e-6)*((T_s+273.15)/300)^(3/2)
                                        {Binary mass diffusivity of water in air at surface, m^2/s}
h_fg=(Enthalpy(Water, T=T_s, x=1)-Enthalpy(Water, T=T_s, x=0))
                                                    {latent heat at surface, kJ/kg}
k_as=Conductivity(AirH2O,T=T_s, P=p, R=1)
                                    {thermal conductivity of moist air at surface, W/m-K}
mu_as=Viscosity(AirH2O,T=T_s,P=p, R=1)        {viscosity of moist air at surface, kg/m-s}
nu_as=mu_as/rho_ss                      {kinematic viscosity of moist air at surface, m^2/s}
rho_ws=Density(Water, T=T_s, x=1)             {density of water vapor at surface, kg/m^3}
rho_das=Density(AirH2O,T=T_s, P=p_das, w=0)       {density of dry air at surface, kg/m^3}
rho_ss=rho_ws+rho_das                       {density of moist air at surface, kg/m^3}
p_ws=Pressure(Water, T=T_s, x=0.          {saturation water vapor pressure at surface, kPa}
p_das=p-p_ws                              {partial pressure of dry air at surface, kPa}
Pr_s=(cp_s*mu_as)/k_as                      {Prandtl number of moist air at surface}
Sc_s=nu_as/(D_AB)                       {Schmidt number of water in air  at surface}
w_ss=HumRat(AirH2O,T=T_s, P=p, R=1) {humidity ratio at saturation at surface, kg_w/kg_da}
"Calculate appropriate mass fractions and driving potentials"
mf_ws=rho_ws/rho_ss                 {mass fraction of water vapor at liquid-vapor interface}
beta_i=(mf_wi-mf_ws)/(mf_ws-1)              {mass transfer driving force,  at inlet , -}
Nusselt_P=h*P_f/k_as                          {Nusselt number based on fin
spacing}
Sherwood_P=Nusselt_P*((Sc_s/Pr_s)^(1/3))      {Sherwood number by heat and mass analogy}
g_mstar=Sherwood_P*D_AB*rho_ss/P_f
                                {mass transfer coefficient at zero mass transfer rate, kg/m^2-s}
w_ao=mf_wo/(1-mf_wo)          {outlet humidity ratio, as related to mass fraction, kg_w/kg_da}
beta_o=(mf_wo-mf_ws)/(mf_ws-1)              {mass transfer driving force, at outlet, -}
beta_i=beta_o*exp((beta_i-beta_o)/beta_lm)                  {log mean driving force, -}
{Heat and mass transfer correlations}
g_m=g_mstar*ln(1+beta_lm)/beta_lm
                        {mass transfer coefficient at finite rate, Couette-flow model, kg/m^2-s}
{Energy transfer rate and conservation}
Q_sens=C_min*epsilon*(T_ai-T_ci)              {Sensible component of heat transfer, KW}
{Mass rate and conservation}
m_c=-g_m*beta_lm*A_To                     {mass transfer rate (condensation), kg/s}
mdot_da=mdot_a/(1+w_ai)                             {mass flow rate of dry air, kg/s}
m_c=mdot_da*(w_ai-w_ao)                               {gives w_wo, kg_w/kg_da}
```

```
Q_lat=m_c*h_fg                                          {latent heat transfer, kW}
Q=mdot_cool*Cp_cool*(T_co-T_ci)                         {coolant side heat transfer}
h_ao=Enthalpy(AirH2O,T=T_ao, P=p, w=w_ao)               {enthalpy of moist air at outlet, kJ/kg}
Q=mdot_a*(h_ai-h_ao)                {total (sensible+latent) heat transfer rate from air flow, kW}
Q=Q_sens+Q_lat                      {total (sensible+latent) heat transfer rate from air flow, kW}
SHR=Q_sens/Q                                            {sensible heat ratio}
rho_ao=Density(AirH2O,T=T_ao, P=p, w=w_ao)              {final density at the exit, kg/m^3}
END

"All the Procedures and Modules end here"



"Main Program starts here"

"Calculating the coolant side thermal resistance"
mdot_cool=0.09                                          {mass flow rate of fluid, kg/sec}
vol_c=mdot_cool/rho_c                                   {volume flow rate of fluid, m^3/kg}
T_ci=3.0                                                {inlet fluid temperature, C}
T_s=(T_ci+T_co)/2 ;                 {Average fluid temperature without drainage channels, C}
T_s_ch=(T_ci+T_co_ch)/2               {Average fluid temperature with drainage channels, C}
CALL ethglyprop(T_s:k_cool,Pr_c,nu_c,Cp_c,rho_c)
          {Calculating the properties of fluid at average temperature, without drainage channels}
CALL ethglyprop(T_s_ch:k_cool_ch,Pr_c_ch,nu_c_ch,Cp_c_ch,rho_c_ch)
            {Calculating the properties of fluid at average temperature, with drainage channels}
l_tube=28E-3 [m]                                        {dimensions of tubes}
w_tube=3E-3[m]
height_tube=90.0E-3 [m]
A_cross_section=l_tube*w_tube
v_cool=vol_c/A_cross_section                            {velocity of coolant, m/s}
P_tube=2*(l_tube+w_tube)
D_h=4*A_cross_section/P_tube                            {hydraulic diameter, m}
Re_D=v_cool*D_h/nu_c                                    {Reynolds number}
Re_D_ch=v_cool*D_h/nu_c_ch
" for constant heat flux relation for the Nusselt no. when the flow is thermally developing and
hydrodynamically developed"
Nusselt_D=4.36+((0.0668*(D_h/height_tube)*Re_D*Pr_c)/(1+0.04*((D_h/height_tube)*Re_D*
Pr_c)^(2/3)))
Nusselt_D_ch=4.36+((0.0668*(D_h/height_tube)*Re_D_ch*Pr_c_ch)/(1+0.04*((D_h/height_tu
be)*Re_D_ch*Pr_c_ch)^(2/3)))
h_tube=Nusselt_D*k_cool/D_h                     {heat transfer coefficient, W/m^2-K}
h_tube_ch=Nusselt_D_ch*k_cool_ch/D_h
A_tube_inside=P_tube*height_tube
Res_cool=1/(h_tube*A_tube_inside*N_tube)
                          {Thermal resistance of coolant, without drainage channels, C/W}
Res_cool_ch=1/(h_tube_ch*A_tube_inside*N_tube)
```

```
                                                {Thermal resistance of coolant, with drainage channels, C/W}



"calculations for tube resistance"
delta_tube=0.2E-3
delta_tube_extra=1E-3
                {extra thickness caused by the extra material adhered to create drainage channels, m}
k_tube=250 [W/m K]                                  {Thermal conductivity of aluminum, W/m-K}
Res_tube=(delta_tube+delta_tube_extra)/(k_tube*A_tube*N_tube)


"resistance due to epoxy used"
delta_epoxy=0.2e-3                                          {thickness of the epoxy used, m}
k_epoxy=5.5 [W/mK]                                  {thermal conductivity of the epoxy, W/m-K}
A_epoxy=height_tube*l_tube
Res_epoxy=delta_epoxy/(k_epoxy*A_epoxy*N_tube*2)
                                                        {Thermal resistance due to epoxy, C/W}


"Air-Side Thermal resistance Calculations"
"Starting from the inlet properties"
{Inlet air conditions, pressure, relative humidity, temperature, velocity}
p=101.325;                                                                  {pressure, kPa}
R_i=0.8                                                          {inlet relative humidity, %/100}
T_ai=35                                                             {inlet air temperature, C}
V_fr=1.5                                                                    {Velocity, m/s}
w_ai=HUMRAT(AirH2O, T=T_ai, P=p, R=R_i)                  {inlet humidity ratio, kg_w/kg_da}
h_ai=Enthalpy(AirH2O,T=T_ai, P=p, w=w_ai)                {enthalpy of moist air at inlet, kJ/kg}
rho_ai=Density(AirH2O,T=T_ai, P=p, w=w_ai)                {inlet moist-air density, kg/m^3}
rho_wi=Density(Water,T=T_ai, P=p_wi)                      {inlet water vapor density, kg/m^3}
rho_dai=rho_ai-rho_wi                                      {density of dry air, inlet, kg/m^3}
p_wi=R_i*PRESSURE(Water, T=T_ai, x=0.5)                    {inlet water vapor pressure, kPa}
p_dai=p-p_wi                                          {inlet partial pressure of dry air, kPa}
mf_wi=rho_wi/rho_ai                                              {inlet water mass fraction}

"dimensions of heat exchanger and experimental section"
Height_tunnel=0.33          {dimensions of the wind tunnel, defining the experimental section, m}
Width_tunnel=0.228

Width=N_tube*T_p                                                {width of heat exchanger, m}
mdot_a=rho_ai*V_fr*Height_tunnel*Width_tunnel
A_fr=height_tube*Width                                  {frontal area of heat exchanger, m^2}
A_min=A_fr-N_fins*delta_f*N_finstock*F_w-N_tube*w_tube*height_tube
                                                        {Minimum area for free flow, m^2}
sigma=A_min/A_fr                                        {Ratio of min and the frontal area}
```

```
"properties of the fin stock/heat exchanger"
L_p=1.4e-3                                                    {Louver spacing,
m}
F_d=16e-3                                                     {fin depth, m}
F_w=8.6e-3                                                    {fin width, m}
L_w=6.2e-3                                                    {louver width, m}
F_p=1.2e-3
alpha=27*pi/180                                               {louver angle, radians}
delta_f=0.1e-3                                                {fin thickness, m}
theta_r=50*pi/180                                             {receding contact angle, radians}
N_L_B=2                                                       {no. of louver banks}
T_p=F_w+w_tube+2*delta_tube+2*delta_tube_extra+2*delta_epoxy   {tube spacing,
m}
N_fins=height_tube/F_p                                        {no. of fins}
N_tube=9                                                      {no. of tubes}
N_finstock=N_tube-1                                           {no. of fin sections}

"Calculation of air side heat transfer area-details in Appendix-A"
A_fin_single_side=F_d*F_w
A_fin=N_finstock*N_fins*A_fin_single_side*2
A_tube_single_side=height_tube*F_d*(1-(delta_f/F_p))
A_tube=A_tube_single_side*2*N_tube
A_To=A_fin+A_tube+A_small                                     {total outside area, m^2}
A_small=A_small_fin+A_small_tube
A_small_fin=N_fins*delta_f*F_w*2*N_finstock
Tube_minor_dia=T_p-F_w
A_small_tube=N_tube*Tube_minor_dia*height_tube*2

"overall heat transfer coefficient without drainage channels"
R_a=(R_i+R_o)/2                                               {average relative humidity}
T_a=(T_ai+T_ao)/2                                             {average temperature}
CALL jcorrelation(F_p,L_p,F_d,F_w,L_w,delta_f,alpha,N_L_B,T_p,V_fr,T_ai,p,R_i,sigma:j)
CALL wetmultiplier (F_p,L_p,F_d,F_w,L_w,delta_f,alpha,theta_r,V_fr,T_ai,p,
R_i,sigma:phi_j,Re_Lp)
j_nonch=j*phi_j                          {j-factor for complete wet conditions, without channels}
CALL hfromj(j_nonch,V_fr,T_a,p,R_a,sigma:h,Cp_a,rho_a)
CALL eff(h,k_tube,delta_f,F_w,A_fin,A_To,b_f,Cp_a:eta)
hf_base=ENTHALPY(AirH2O,T=T_s, P=p,R=1)
hf_tip=ENTHALPY(AirH2O,T=T_a, P=p,R=1)
b_f=(hf_base-hf_tip)/(T_s-T_a)                        {slope of enthalpy line, KJ/kg-K}
Res_air=(1/(h*A_To*eta))                  {air-side heat transfer coefficient, W/m^2K}
UA=((((Res_cool+Res_tube+Res_epoxy)*(Q/Q_sens))+Res_air)*1000)^(-1)

"overall heat transfer coefficient with drainage channels"
```

```
R_a_ch=(R_i+R_o_ch)/2
T_a_ch=(T_ai+T_ao_ch)/2
CALL
jcorrelation(F_p,L_p,F_d,F_w,L_w,delta_f,alpha,N_L_B,T_p,V_fr,T_ai,p,R_i,sigma:j_ch_1)
CALL wetmultiplier (F_p,L_p,F_d,F_w,L_w,delta_f,alpha,theta_r,V_fr,T_ai,p,
R_i,sigma:phi_j_ch,Re_Lp_ch)
j_ch=phi_j_ch*j_ch_1*0.7+j_ch_1*0.3   {assuming drainage channels reduce retention by 30%}
CALL hfromj(j_ch,V_fr,T_a_ch,p,R_a_ch,sigma:h_ch,Cp_a_ch,rho_a_ch)
CALL eff(h_ch,k_tube,delta_f,F_w,A_fin,A_To,b_f_ch,Cp_a_ch:eta_ch)
hf_base_ch=ENTHALPY(AirH2O,T=T_s_ch, P=p,R=1)
hf_tip_ch=ENTHALPY(AirH2O,T=T_a_ch, P=p,R=1)
b_f_ch=(hf_base_ch-hf_tip_ch)/(T_s_ch-T_a_ch)
Res_air_ch=(1/(h_ch*A_To*eta_ch))
UA_ch=((((Res_cool_ch+Res_tube+Res_epoxy)*(Q_ch/Q_sens_ch))+Res_air_ch)*1000)^(-1)

"calculating the effectiveness for channeled and non-channeled case"
CALL eps(UA,mdot_cool,mdot_a, Cp_a, Cp_c:epsilon,C_min)
CALL eps(UA_ch,mdot_cool,mdot_a, Cp_a_ch, Cp_c_ch:epsilon_ch,C_min_ch)

"calculating final values for both cases"
CALL finalcalc
(T_s,p,T_ai,T_ci,w_ai,R_i,h,F_p,A_To,mdot_a,mdot_cool,UA,Cp_c,C_min,epsilon,mf_wi,h_ai:
Q,Q_sens,Q_lat,SHR,T_ao,T_co,w_ao,rho_ao)
CALL finalcalc
(T_s_ch,p,T_ai,T_ci,w_ai,R_i,h_ch,F_p,A_To,mdot_a,mdot_cool,UA_ch,Cp_c_ch,C_min_ch,ep
silon_ch,mf_wi,h_ai:Q_ch,Q_sens_ch,Q_lat_ch,SHR_ch,T_ao_ch,T_co_ch,w_ao_ch,rho_ao_ch
)

R_o=RELHUM(AirH2O,T=T_ao,P=p,w=w_ao)
R_o_ch=RELHUM(AirH2O,T=T_ao,P=p,w=w_ao_ch)

"Pressure drop without drainage channels"
CALL fcorrelation(F_p,L_p,F_d,F_w,L_w,delta_f,alpha,N_L_B,T_p,V_fr,T_ai,p,R_i,sigma:f)
CALL fwetmultiplier (F_p,L_p,F_d,F_w,L_w,delta_f,alpha,T_p,V_fr,T_ai,p, R_i,sigma:phi_f)
f_nonch=f*phi_f
CALL pfromf(A_min,A_To,T_a,p,rho_ai,V_fr,R_a,sigma, rho_ao,f_nonch:delta_p)

"Pressure drop with drainage channels"
CALL fcorrelation(F_p,L_p,F_d,F_w,L_w,delta_f,alpha,N_L_B,T_p,V_fr,T_ai,p,R_i,sigma
:f_ch_1)
CALL fwetmultiplier (F_p,L_p,F_d,F_w,L_w,delta_f,alpha,T_p,V_fr,T_ai,p,
R_i,sigma:phi_f_ch)
f_ch=phi_f_ch*f_ch_1*0.7+f_ch_1*0.3
CALL pfromf(A_min,A_To,T_a_ch,p,rho_ai,V_fr,R_a_ch,sigma, rho_ao,f_ch:delta_p_ch)

"latent heat ratio"
```

```
LHR=1-SHR
LHR_ch=1-SHR_ch

"difference caused by drainage channels in LHR"
LHR_diff=(LHR_ch-LHR)/LHR*100

"in pressure drop"
Press_diff=(delta_p-delta_p_ch)/delta_p_ch*100

"in heat transfer and its components"
Q_sens_diff=(Q_sens_ch-Q_sens)/Q_sens*100
Q_lat_diff=(Q_lat_ch-Q_lat)/Q_lat*100
Q_diff=(Q_ch-Q)/Q*100
```